Quantum Sensors for Electromagnetic Induction Imaging: from Atomic Vapours to Bose-Einstein Condensates

Benjamin Paul Maddox

A dissertation submitted in partial fulfillment

of the requirements for the degree of

Doctor of Philosophy

of

University College London.

Department of Physics and Astronomy

University College London

October 28, 2022

I, Benjamin Paul Maddox, confirm that the work presented in this thesis is my own. Where information has been derived from other sources, I confirm that this has been indicated in the work.

Abstract

In this thesis, two sensors for electromagnetic induction imaging (EMI) are presented based on radio-frequency atomic magnetometry (RF-AM) in alkali atoms.

The first sensor addresses portability and real-world use of EMI with AMs, by housing the major components of the RF-AM within a lightweight, minaturised system that can be mechanically translated. The atomic source was provided by a thermal vapour of ^{87}Rb and was pumped/probed on the D_1 line. The performance of the sensor is detailed and an RF sensitivity of $dB_{AC} = 19\,\mathrm{pT}/\sqrt{\mathrm{Hz}}$ was achieved. Stability of the device was investigated and potential improvements to the design are discussed. EMI with the sensor is then tested by application to two real-world industrial problems. Through-skin pilot-hole detection in Al strut-skin arrangements and corrosion detection under thermal/electrical insulation. The mechanically translatable RF-AM was able to detect and localise pilot-holes of diameter 16 mm concealed by an Al skin of thickness 0.41 mm with sub-mm precision. For corrosion detection, localisation and depth detection of recesses in an Al plate was achieved when concealed with a 1.5 mm thick piece of rubber acting as an electrical/thermal insulator. The sensor demonstrates key advantages over existing solutions to these challenges in a package that is within the reach of real-world deployment.

The second sensor addresses the spatial resolution limitations of thermal vapours, by instead utilising ultra-cold atoms trapped in a tight optical potential, as the atomic source for the RF-AM. Initially an existing ^{87}Rb BEC setup is optimised and characterised. A BEC of 65k atoms is produced via optical evaporation with a final volume

of 3.2×10^{-8} cm^{-3}. The BEC RF sensitivity is measured to be $dB_{AC} = 268\,\mathrm{pT}/\sqrt{\mathrm{Hz}}$ with a volumetric sensitivity of $dB_{AC}\sqrt{V} = 50.2\,\mathrm{fT}\sqrt{\mathrm{cm}^3/\mathrm{Hz}}$. The BEC RF-AM is found not to be limited by the atomic projection noise and a strategy for further improvements is discussed.

Additionally, work towards developing another cold atoms platform for magnetometry in ^{133}Cs is presented. Construction of a new vacuum chamber and optical setup is outlined and laser cooling to 3 µK is demonstrated with 3D degenerate Raman sideband cooling (dRSC). An optical setup for a high power dipole trap at 1064 nm was built and tested, with a promising outlook for future dipole trapping and optical evaporation to a BEC.

Impact Statement

Electromagnetic induction imaging (EMI) opens up the potential for a diagnostic technique that is based on measuring the propagation of radio-frequency (RF) magnetic fields in a material. This non-contact, inherently safe and versatile procedure can find applications in industry, defence and medical imaging. The development of this emerging technology is limited by the performance of magnetometers that are able to sense RF magnetic fields. Currently induction coils are the conventional sensor of choice but degrade in performance at low frequencies where higher penetration can be achieved by the RF magnetic fields. Atomic magnetometers (AMs) can be configured to sense RF magnetic fields and replace the induction coils used in EMI. They are capable of outcompeting the sensitivity of induction coils at low frequencies [1] and have already be demonstrated to achieve EMI in unshielded magnetic environments [2, 3, 4]. However, these realisations are often bulky and impractical with optical and magnetic control systems that require very stable mechanical and magnetic conditions to function. This necessity effectively limits EMI with AMs to laboratory settings with the object having to be moved about the sensor in order to form an image. EMI is also currently limited to mm spatial resolution due to sensor volume constraints.

This thesis presents work towards portability of EMI with AMs, introducing a AM that can be housed inside a small lightweight sensor head capable of being exposed to unshielded urban magnetic environments and robust in mechanical translation of an area for imaging. Several present-day industrial tasks were successfully

demonstrated with this system, showing key benefits over existing solutions. This proof-of-concept was published [5, 6] and shows that EMI is capable of escaping the laboratory and converging to commercial industrial use outside of academia. The thesis later explores AMs generated in ultra-cold atomic samples which offers the prospect of bringing high spatial resolution imaging to EMI with sensor volumes that are orders of magnitude smaller than vapour cell based AMs. A Bose-Einstein condensate was utilised for the atomic sample and allowed the measurement of RF magnetic fields at the 10 µm scale. The work was published in [7] and creates the possibility of further research into enhancing the AM performance by manipulating the properties of quantum gases.

Acknowledgements

Firstly, I thank Professor Ferruccio Renzoni at UCL and Professor Kai Bongs at University of Birmingham for giving me the opportunity to undertake this PhD. Ferruccio was my primary supervisor at UCL and I thank him for encouraging me to take on several projects throughout this time, which I have learned so much from. His knowledge and enthusiasm for atomic physics has helped me tackle many challenges and I will carry these lessons with me. Thank you also to Professor Phil Jones for being my secondary supervisor at UCL, for always lending his time to discuss experiments and all the insightful suggestions over the years.

I am heavily indebted to Dr Cameron Deans for the impact he had on me as a researcher. His diligent creativity still echoes here in the lab and I try to emulate it, wherever I can. There is no one better at LabVIEW, or at the very least, no one who loves it as much. Thanks also to Dr Luca Marmugi for all the things he taught me about lasers.

I have been uniquely fortunate to have had great partnership in my friend Yuval Cohen, who I am proud to now be able to call Dr Yuval Cohen. He was with me from the very beginning back in our final year project of undergraduate in Birmingham and we came full circle to work together again at the end of my PhD. We always put doubt before certainty, even when it was difficult, and so much of my development has come as a result of that. I'll miss the *state of things* conversations.

To Dr Poomaradee Tanapoom (aka Pik), thanks for getting me started at UCL on the Cs experiment, for all the energy you brought to the lab and the persistent en-

couragement you gave me even after you had finished your PhD. All the best for the future mate. To Krishna Jadeja, thanks for the early contributions to the Cs experiment and congratulations on completing your PhD thesis. Thanks to everyone else in the lab: Han, Sindi, Antonio, Nin and Torin for making this a great place to work and for all the joyful lunchtime conversations.

So many problems would not have been overcome without the help of the UCL Physics department staff. I thank Mark Sterling for the uncountable number of parts he machined for me over the years and for all the fantastic conversations about car engines. *Big up Brixton*. Rafid Jawad, for the mountain of electronics he built for the lab. Sorry for all the ground loops we made. Derek Thomas and Bernard Bristoll for all the times they went above and beyond their job description to help out our lab.

To Leonard and Will, from that first PPS event in physics undergrad, all the way to me writing this, there's no way I could have enjoyed physics as much without you and I wouldn't trade those memories for anything. Thanks for having my back all those years. To my friends from UoB weightlifting club: Chris, Henry, Joe and Aidan, it was a privilege to lift all that metal together, and all the Monster we drank in the process. And to all the guys on the lifting big chat: the laughter got me through this. *RIP Munrow*. Aaron, cheers for all the snooker matches, *ton up* my friend. To my school friends: Simon, Nas, Alex, Oli, Max and George, its been an honour to meet up every year to renew the chess rivalry and fight it out for the Power-Rankings. See you all at POWERS-XI. To James, I cant believe we made it out of Gisbert-Kapp alive. Take care mate. To my family, thank you for being a rock to stand on in good times and bad. Particularly my parents, who have perpetually inspired me to chase my ambitions. Finally, I think of all the moments I would have found insurmountable without my girlfriend Emily, whose relentless sense of humour has never failed to melt away pessimism, and to spur on creativity.

The experiment, is never truly finished.

Contents

List of Figures

List of Tables

Chapter 1

Introduction

The use of magnetic fields as an investigative measurement tool is ubiquitous in industrial, military and medical practices around the world. With ambitions to push these techniques beyond current limits, comes the need for sensors that can surpass that of the existing traditional magnetometers.

1.1 Electromagnetic induction imaging (EMI)

Electromagnetic induction imaging (EMI) presents a contactless, non-invasive and inherently safe imaging technique that is based on measuring the response of a material to oscillating magnetic fields. Object detection [8], object tracking [9], fault detection [10] and biomedical imaging [11, 12] have been experimentally explored. Due to the skin effect, the penetration depth of the oscillating magnetic field will vary with frequency, allowing for a tomographic measurement and imaging of conductive objects enclosed by metallic shielding [13]. The effectiveness of the technique is generally limited by the properties of the sensor measuring the secondary field:

- **Sensitivity** is the standard benchmark used to compare magnetic sensors and gives the unit of uncertainty on a given magnetic measurement normalised by the averaging time. The typical units are given in $\mathrm{T}/\sqrt{\mathrm{Hz}}$. In the context of EMI, the better the sensitivity, the greater the contrast in the imaging.

Measurements of sensitivity are usually done in magnetic shielding to subtract the effect of a noisy magnetic environment. However it is important to realise that for many applications it is not possible to shield the measurement environment and therefore sensors need to be able to operate in unshielded environments. Hence many realisations of sensors will quote the unshielded sensitivity, which is often lower.

- **Portability** presents a bottleneck for the deployment of EMI systems. Many sensors are too fragile or too bulky to be moved and thus, to achieve EMI, the target under investigation must instead be moved about the sensor. This can be undesirable, or even impossible in the case of aircraft investigation [6] or medical imaging. Size, weight and power consumption are the major points of consideration in portability with each of these needing to be minimised. The lack of portability of some sensors leads to the impossibility of deployment in rough conditions for geological or astronautical missions [14].

- **Spatial resolution** of the sensor can become the main limiting factor on the spatial resolution of the EMI image. Sensors typically face a trade-off in sensitivity to increase their spatial resolution and manufacture below the $\sim 1\,\mathrm{mm}^3$ level presents a limit to many sensor technologies. To account for this trade-off the magnetic sensitivity figure-of-merit can be normalised to the sensor volume, in what is refered to as the *volumetric sensitivity* given in units of $\mathrm{T}\sqrt{\mathrm{cm}^3/\mathrm{Hz}}$.

- **Operational Frequency** sets a limit on the penetration depth of EMI as is dictated by the skin effect of the material.

- **Cost and Mass Producibility** impact the adoption of the sensor technology and speed of innovation.

1.2 Sensors for EMI

1.2.1 Induction Coils

Induction coils represent the incumbent sensor of EMI, having been used for the early development of this technology [15, 16]. They are low cost and simple to implement, with robust manufacturing allowing for high portability. While induction coils can reach sub-pT$/\sqrt{\text{Hz}}$ sensitivity in the $>$50 MHz regime, their sensitivity becomes fundamentally limited by Johnson noise at low frequencies [1]. Manufacturing coils to scales less than 1 mm diameter is a general problem for increasing spatial resolution.

1.2.2 Giant Magnetoresistance (GMR)

Magnetoresistance can be observed as the change in resistance of a material given by a change in the mangitude of the external magnetic field across it. The observation of *giant* magnetoresistance[1] can be seen in microfabricated multilayered structures arranged into a magnetic-nonmagnetic-magnetic pattern [17]. GMR sensors have high magnetic field range and can be microfabricated to be very small with spatial resolution approaching 20 µm [18]. Their sensitivity at these scales however is at the $\sim$100 pT$/\sqrt{\text{Hz}}$ level [19]. GMR sensors are also intrinsically limited at low frequencies (below 1 kHz) by the flicker noise ($1/f$ noise), which lowers their sensitivity and restricts their capability for through-skin EMI.

1.2.3 SQUIDs (Superconducting Quantum Interference Devices)

SQUID magnetometers exploit the dynamics of Josephson junctions in superconductors. A SQUID typically consists of a ring of superconductor, segmented by one or more Josephson junctions whereby an electrically resistive material creates a discontinuity in the superconducting ring. If the current passed through the SQUID is below a critical current I_c, Cooper pairs can tunnel through the barrier and the SQUID acts as a superconductor with no voltage drop over the circuit [20]. Above I_c, the SQUID becomes limited by the resitive material and behaves ohmically. This

[1] Maximum possible change in resistance of $>$10%

creates a discontinuity in the I-V curve of a SQUID, around I_c, as the SQUID crosses from the *superconductive state* to the *normal state*. It is at this discontinuity that the SQUID is extremely sensitive to external magnetic fields that effectively change I_c and thus dramatically change the voltage drop across the SQUID. In the case of the RF SQUID, one Josephson junction is inductively coupled to an RLC circuit which picks up the measured RF field [21]. For decades the SQUID represented the state-of-the-art sub-fT$/\sqrt{\text{Hz}}$ magnetic sensitivity but bulky and expensive cryogenic cooling systems are required for their operation, which limits their ability to be mass-produced or deployed in the field.

1.2.4 NV centres (Nitrogen Vacancy)

Nitrogen vacancy centres in diamonds can be utilised for optical magnetometry. A nitrogen defect creates a discontinuity in the bonding of the carbon lattice, leaving a vacancy, which leaves 5 unpaired electrons [22]. The NV centre can capture an extra electron to form the NV^- centre whose state can be manipulated by optical fields [23]. The system is optically pumped and upon de-excitation the NV centre will fluoresce. This fluorescence can then be detected via a microscope and used to infer the local magnetic field. NV centres can be used to measure DC or AC magnetic fields. The small scale and rigid binding of the NV centre in the lattice leads to very high spatial resolution with some measurements resolving the $\sim$10 nm scale [24], though at these length scales, the magnetic sensitivity of NV centres is typically $\sim$100 nT$/\sqrt{\text{Hz}}$ [25]. Another advantage of NV centres is their robustness, being able to operate in large temperature ranges from cryogenic temperatures up to 700 K and large pressure ranges from high-vacuum to 70 GPa [26].

1.2.5 Atomic Magnetometers (AMs)

Atomic magnetometers measure the spin state of a collection of optically pumped alkali atoms, as their energy levels shift due to the local magnetic field. Typically, a glass cell containing a thermal alkali vapour is probed with a linearly polarised laser beam, which interrogates the atoms. Changes in the total spin state lead to a rotation of the polarisation of the probe beam, which can then be read off with a polarimeter.

There are many forms of atomic magnetometer, used to measure DC or AC fields in particular conditions. The most sensitive atomic magnetometers, SERF magnetometers (Spin-Exchange Relaxation Free), have demonstrated the state-of-the-art magnetic sensitivity level of 160 $\mathrm{aT}/\sqrt{\mathrm{Hz}}$ [27]. For sensing AC fields the radio frequency atomic magnetometer (RF-AM), first developed in Princeton [28], can reach similarly extreme levels of magnetic sensitivity with the record currently standing at 240 $\mathrm{aT}/\sqrt{\mathrm{Hz}}$ [29]. Unshielded RF-AMs have managed to reach the 10-100 $\mathrm{fT}/\sqrt{\mathrm{Hz}}$ level [30, 31, 32] with a gradiometer configuration achieving $<1\,\mathrm{fT}/\sqrt{\mathrm{Hz}}$ [33]. The spatial resolution is generally limited by the confinement of the atoms, which is either achieved by reducing the cell dimensions or by adding a buffer gas to reduce the mean-free-path of the atomic motion. Microfabricated cells can be made to the mm scale allowing for increased portability [34, 35, 36]. High buffer gas pressure cells can restrict the motion of the atoms to the diffusion length which can be made to be of the order of 1 mm [37, 38].

1.2.6 Cold Atom Magnetometers

Pushing the extreme sensitivity of atomic magnetometers into sensing volumes below the mm scale becomes difficult due to the depolarising effects of atom-wall collisions which increase in probability as the cell decreases in size, or atom-buffer collisions which increase as the buffer gas pressure increases. Optically trapping a cold atomic sample under ultra-high vacuum (UHV) can circumvent this by constraining the atoms to an optical dipole potential, capable of isolating atoms to the 1 μm scale [39]. Several atomic magnetometers have been realised in optical traps to measure DC [38] and RF fields [40]. Their sensitivities are generally in the $\mathrm{pT}/\sqrt{\mathrm{Hz}}$ range, mainly due to the large reduction in atom number in the sensor volume. At present these systems are large and bulky, requiring many complex optical systems and vacuum chambers, but work is progressing to build optical traps on atom chips [41] and create compact vacuum systems that do not require active pumping [42].

1.3 Thesis Motivation

So far, most EMI systems have been realised with induction coils as the main sensor. Due to the skin effect (see section 2.1), oscillating magnetic fields will penetrate deeper into a target material with lower and lower frequency, enabling EMI imaging through conductive barriers. However, induction coils are fundamentally limited at low frequencies by the Johnson noise. Radio-frequency atomic magnetometers (RF-AMs) are fundamentally limited by the atomic projection noise which is insensitive to frequency and therefore RF-AMs outperform induction coils below 50 MHz, specifically enjoying over two orders of magnitude improvement in sensitivity in the 1-100 kHz regime [1]. AMs also offer the chance to obviate the use of bulky and expensive cryogenic cooling required for SQUIDs, which restricts portability and mass production. The ability to detect low frequency magnetic fields with higher precision than coils makes AMs a promising candidate for improving through-skin imaging.

The use of a cold atom RF-AM offers the potential to increase the spatial resolution of EMI with AMs to the micron scale, while offering higher sensitivity than other high spatial resolution magnetometers like NV centres and GMR. Cooling the atomic sample to quantum degeneracy in a Bose-Einstein condensate (BEC) also offers the chance to explore collective measurement and achieve sensitivities that surpass the atomic projection noise limit [44].

In this thesis, I present work on two different sensors for EMI: an unshielded miniaturised RF-AM based on a thermal vapour cell, and an ultra-cold atoms system for an RF-AM in a BEC.

Chapter 2

Concepts

2.1 Electromagnetic Induction Imaging

The general principle of Electromagnetic Induction Imaging (EMI) relies on the measurement of a secondary magnetic field induced by eddy currents in a material. A depiction of this effect can be seen in figure 2.1a. To induce eddy currents in a material, an oscillating magnetic field B_1 known as the primary field, is applied. The eddy currents then form closed loops in the material and generate the secondary field B_2 that opposes the primary field (Lenz's law). The complex vector sum of the two magnetic fields (figure 2.1b) creates the total field B_{TOT} which is then detected by an AC magnetometer. An oscillating radio-frequency magnetic field B_{RF} propagating through a target material along the z axis will decay in amplitude according to [12, 45]

$$B_{RF}(z) = B_{RF}(0)e^{-z/\delta(\omega_{RF})}, \tag{2.1}$$

where $\delta(\omega_{RF})$ is the penetration depth of the wave at a frequency ω_{RF} due to the skin effect given by [2, 46]

$$\delta(\omega_{RF}) = \sqrt{\frac{2}{\omega_{RF}\sigma_T\mu_T}}\left[\sqrt{1+\left(\frac{\omega_{RF}\varepsilon_T}{\sigma_T}\right)^2}+\frac{\omega_{RF}\varepsilon_T}{\sigma_T}\right]^{1/2}, \tag{2.2}$$

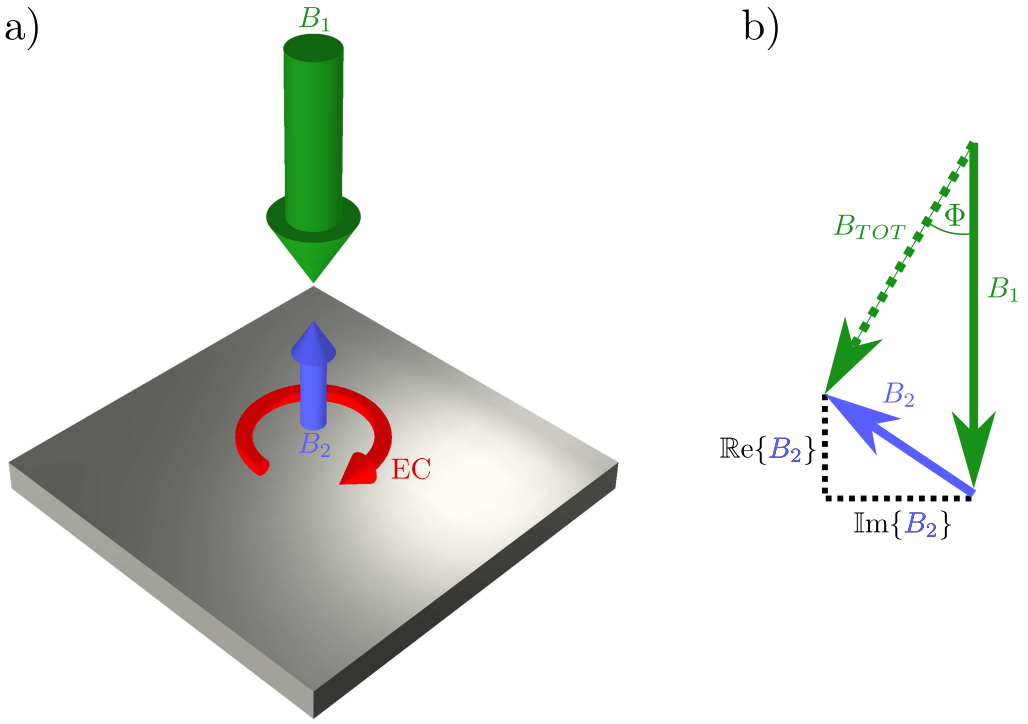

Figure 2.1: Illustrative depiction of the process of EMI of a target material a) with a complex vector diagram b) showing the addition of the primary B_1 and secondary B_2 magnetic fields. Green, blue and red arrows show the primary field B_1, the secondary field B_2 and the eddy currents (EC) respectively. The imaginary component of B_2 is neglected in a) to simplify the directionality of the primary and secondary fields.

where σ_T, ε_T and μ_T are the conductivity, electrical permittivity and magnetic permeability of the target material respectively. The application of a primary RF field B_1 at frequency ω_{RF} generates eddy currents in the target material which create the secondary field B_2 and the overall EMI response is given by [2, 47]

$$\begin{aligned}\frac{B_2}{B_1} &= \Lambda_1 \omega_{RF} \mu_0 \left[\omega_{RF} \varepsilon_0 (\varepsilon_r - 1) - i\sigma_T\right] + \Lambda_2(\mu_r - 1) \\ &= \underbrace{\underbrace{\Lambda_1 \omega_{RF} \mu_0 \omega_{RF} \varepsilon_0 (\varepsilon_r - 1)}_{\text{Displacement current density}} - \underbrace{i\Lambda_1 \omega_{RF} \mu_0 \sigma_T}_{\text{Eddy current density}}}_{\text{Eddy currents}} + \underbrace{\Lambda_2(\mu_r - 1)}_{\text{Magnetisation}}\end{aligned} \tag{2.3}$$

where μ_0 and μ_r (ε_0 and ε_r) are the magnetic permeability (electric permittivity) of free-space and relative to the target material respectively. $\Lambda_{1,2}$ are constants that depend on the EMI geometry. Equation 2.3 can be decomposed into two main

contributions, the effect due to eddy currents in the target and the effect due to the magnetisation of the target. The contribution due to eddy currents can be further subdivided into the real part which describes the displacement current density in the material and the imaginary part which represents the eddy current density. While the real components of equation 2.3 contribute to the amplitude decay of B_{TOT} the imaginary part creates a phase lag that is proportional to the conductivity of the sample. Therefore using phase-sensitive detection of B_{TOT} to extract amplitude and phase of the signal can be used to infer all three of the target properties σ_T, ε_T and μ_T. If the eddy currents are well localised in the target (RF coil diameter smaller than target), EMI images can be built up by rastering the target position relative to the position of B_1 and the AC magnetometer.

2.2 Atomic Magnetometry

2.2.1 Zeeman Effect

Within atoms, electronic structure is arranged into the fine structure which is determined by the orbital arrangements of each electron shell. Perturbation of the fine structure due to IJ-coupling, where the total electronic angular momentum $\mathbf{J}$ couples with the nuclear spin $\mathbf{I}$, causes energy splitting to create the hyperfine structure. Hyperfine levels are assigned the quantum number $\mathbf{F}$ which describes the total angular momentum of the atom, where $\mathbf{F} = \mathbf{I} + \mathbf{J}$ [48]. The projection of $\mathbf{F}$ along a quantisation axis gives rise to $2F + 1$ magnetic sublevels of the hyperfine level F denoted by the quantum number m_F. The scalar projection of a static magnetic field $\mathbf{B}$ will then cause energy splitting $\Delta E_{[m_F \leftrightarrow m_F+1]}$ of the magnetic sublevels according to

$$\Delta E_{[m_F \leftrightarrow m_F+1]} = g_F \mu_B B = \hbar \Omega_L \tag{2.4}$$

which gives rise to a frequency associated with this energy splitting called the *Larmor frequency* Ω_L. Here g_F is the Landé factor associated with the hyperfine level, μ_B is the Bohr magneton and $\hbar$ is the reduced Planck constant.

2.2.2 The Atomic Magnetometer

For both DC and AC measurements, the atomic magnetometer takes advantage of the Zeeman effect in order to produce a measurable quantity proportional to the detected magnetic field. An atomic magnetometer measurement is made up of three processes:

- **Atomic polarisation** of the magnetic sublevel populations in the ground state via optical pumping to produce a net total spin vector **S**.
- **Evolution** of the total spin vector in a static magnetic field that introduces Zeeman splitting into the magnetic sublevels of the ground state.
- **Polarimetry** on a probe beam that traverses the atomic ensemble to read off the total spin vector and infer the magnetic field.

To imagine these processes I work from the scenario put forward in [49] where we start with an ensemble of motionless non-interacting two-level atoms, with ground state $F = \frac{1}{2}$ and excited state $F' = \frac{1}{2}$. The ground state can be subdivided into 2 m_F sublevels which we denote as $\left|m_F = \pm\frac{1}{2}\right\rangle = |\pm\rangle$. Initially, with $B_z = 0$, a resonant σ^+ polarised pump beam propagates along the x-axis and optically pumps the atoms from $|-\rangle_x \rightarrow |+\rangle_x$ [50] (see figure 2.2a) until the entire atomic population occupies $|+\rangle_x$. Now $B_z > 0$ which introduces Zeeman splitting in the magnetic sublevels.

In the z-axis, the wavefunction of the ground state Ψ becomes

$$|\Psi\rangle = \frac{1}{\sqrt{2}}\left[e^{-i\Omega_L t/2}\,|+\rangle_z + e^{i\Omega_L t/2}\,|-\rangle_z\right] \tag{2.5}$$

whereby the energy of the Zeeman splitting becomes the effective Hamiltonian. Using the quantum-mechanical rotation matrices we can rotate the states into the x-axis

$$|+\rangle_x = \frac{|-\rangle_z + |+\rangle_z}{\sqrt{2}}; \qquad |-\rangle_x = \frac{|-\rangle_z - |+\rangle_z}{\sqrt{2}}. \tag{2.6}$$

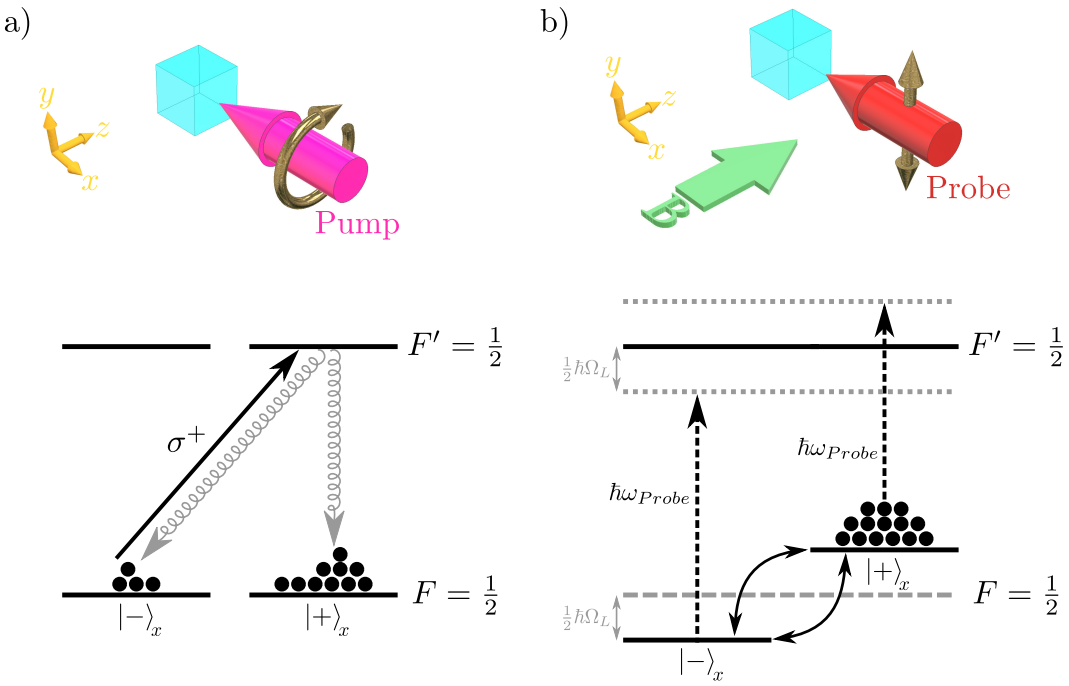

Figure 2.2: Illustrative depiction of the process of a two-level atom being optically pumped a) along the x-axis with $B_z = 0$ and subsequently probed along the x-axis b) during evolution when $B_z > 0$.

The probability $P(\pm,x)$ of finding an atom in each sublevel in the x-axis then becomes

$$P(+,x) = |\langle\Psi|+\rangle_x|^2 = \frac{1}{2}[1-\cos(\Omega_L t)] \tag{2.7}$$

$$P(-,x) = |\langle\Psi|-\rangle_x|^2 = \frac{1}{2}[1+\cos(\Omega_L t)] \tag{2.8}$$

which demonstrates the coherent population oscillation from one state to the other at the Larmor frequency. A linearly polarised probe propagating in the x-axis (see figure 2.2b) can be decomposed into two superimposed contributions of σ^+ and σ^- light. These two contributions then couple to their respective magnetic sublevel and experience a relative detuning from the transition due to the Zeeman effect. This detuning then gives rise to a phase shift proportional to the number of atoms in the state that is probed. As the magnetic sublevel populations oscillate so too does the phase shift between the two circular contributions of the probe, such that the linear

polarisation of the probe beam oscillates at the Larmor frequency. The polarisation rotation ϕ can then be written as [51, 52]

$$\phi = (n_+ - n_-)kL = -\frac{\pi}{2} nLr_e f c \frac{\langle \hat{S}_x \rangle}{S} \mathbb{I}\mathrm{m}\{\bigvee(\omega_{pr} - \omega_0)\} \tag{2.9}$$

where ω_{pr} is the probe frequency, k is the wavevector of the probe light, $n_\pm$ are the indices of refraction for the given sublevel, n is the total atomic number density, L is the path length of the probe-atom intersection, r_e is the classical electron radius, f is the oscillator strength and c is the speed of light. Here $\langle \hat{S}_x \rangle / S$ is the expectation value of the x-axis component of the total spin vector $\mathbf{S}$ of the sample, which represents the polarisation of the sample along the probe axis. $\mathbb{I}\mathrm{m}\{\bigvee(\omega_{pr} - \omega_0)\}$ is the imaginary part of the Voigt profile centred on the optical transition at ω_0

$$\bigvee(\omega_{pr} - \omega_0) = \frac{2\sqrt{\ln 2/\pi}}{\Gamma_G} w\left(\frac{2\sqrt{\ln 2}\,[(\omega_{pr} - \omega_0) + i\Gamma_L/2]}{\Gamma_G}\right), \tag{2.10}$$

where Γ_G and Γ_L are the linewidths of the Gaussian and Lorentzian broadening respectively. $w(x)$ is the complex error function defined by

$$w(\mathrm{x}) = [1 - \mathrm{erf}(-ix)] \exp\left(-x^2\right). \tag{2.11}$$

The Voigt profile gives the true lineshape of an atomic transition after accounting for Gaussian and Lorentzian broadening processes[1]. In reality, the coherence of the magnetic sublevels in the ground state can relax to a steady state via dephasing mechanisms associated with the atoms environment. Hence, for continuous measurement, it becomes necessary to drive the coherence and it is popular to do this with either synchronous pumping [53] or a radio-frequency magnetic field that is resonant with the Zeeman splitting [28].

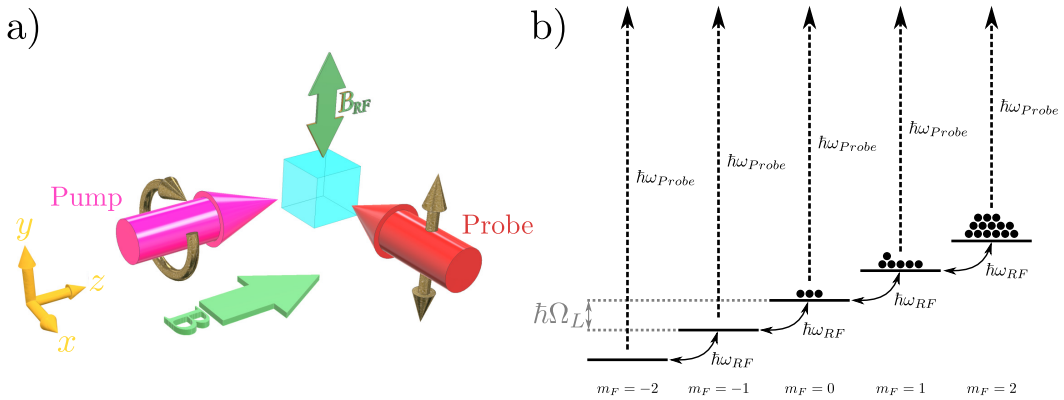

Figure 2.3: Diagram of the geometry of an RF atomic magnetometer a) and illustrative depiction b) of the process of an RF field driving the optically pumped magnetic sublevels in the $F = 2$ ground state of ^{87}Rb. Dashed arrows illustrate the probe transition to the excited state (not shown). Black dots illustrate the relative population in each magnetic sublevel.

2.2.3 The RF Atomic Magnetometer

In the RF magnetometer, a collection of atoms optically pumped along a static field B_{Bias} becomes subject to a perpendicularly aligned radio-frequency (RF) magnetic field B_{RF} at a frequency of ω_{RF}. Figure 2.3a shows the geometry of the RF magnetometer with respect to the atomic source. A circularly polarised pump beam propagates parallel to B_{Bias} in the y axis and the sample is probed by a linearly polarised probe beam in the x axis. When $\omega_{RF} = \Omega_L = \gamma B_{Bias}$ the ground state magnetic sublevel populations are coupled by the RF field allowing transfer between them which then imprints an oscillating polarisation rotation onto the probe beam at ω_{RF}. Figure 2.3b shows an illustrative depiction of this process in the ground state in the $F = 2$ state of ^{87}Rb. The ensemble of atoms get pumped towards the stretched $|F = 2, m_F = 2\rangle$ state creating the population anisotropy in the ground state, for B_{RF} to couple together for population transfer. The RF magnetometer response can be modelled with the Bloch equations as is done in several previous works [2, 51, 54] and I draw from these in the following derivation. The collective spin vector for the atomic ensemble can be written as $\mathbf{S} = S_x\hat{\mathbf{x}} + S_y\hat{\mathbf{y}} + S_z\hat{\mathbf{z}}$ which

[1] Typically for atomic vapors, the Gaussian broadening is due to the Doppler broadening and cannot be neglected as the sample is generally at or above room temperature. The Lorentzian broadening is usually the larger of the natural linewidth and the collisional broadening.

then evolves in a magnetic field $\mathbf{B}$ according to

$$\frac{d\mathbf{S}}{dt} = \gamma \mathbf{S} \times \mathbf{B} - \frac{S_x\hat{\mathbf{x}} + S_y\hat{\mathbf{y}}}{T_2} - \frac{(S_z - S_0)\hat{\mathbf{z}}}{T_1}, \tag{2.12}$$

where γ is the gyromagnetic ratio. The three terms on the right hand side of equation 2.12 represent: the kinetic evolution of the spins in the field, the transverse spin relaxation with decay time T_2 and the longitudinal spin relaxation towards the equilibrium state S_0 with decay time T_1. In the RF magnetometer, the magnetic fields applied becomes the sum of the static bias field and the perpendicularly applied RF field such that the magnetic field is

$$\mathbf{B} = \mathbf{B}_{Bias} + \mathbf{B}_{RF} = B_{Bias}\hat{\mathbf{z}} + 2B_1 \cos(\omega_{RF} t)\hat{\mathbf{y}}, \tag{2.13}$$

where $2B_1 = B_{RF}$. We now move to the rotating frame about $\hat{\mathbf{z}}$ at a frequency ω_{RF} and make the rotating wave approximation, tilde notation above the symbols now indicate the quantity in the rotating frame. The effective magnetic field in the rotating frame B_{eff} then becomes

$$\mathbf{B}_{eff} = \left(B_{Bias} + \frac{\omega_{RF}}{\gamma}\right)\hat{\tilde{\mathbf{z}}} + B_1\hat{\tilde{\mathbf{y}}} = \frac{1}{\gamma}\left(\Delta\omega\hat{\tilde{\mathbf{z}}} + \Omega_1\hat{\tilde{\mathbf{y}}}\right), \tag{2.14}$$

where $\Omega_1 = \gamma B_1$ is the Larmor frequency of the field B_1 and $\Delta\omega = \omega_{RF} - \Omega_L$ is the detuning of the magnetometer from the Larmor frequency of B_{Bias}. The counter-rotating component of the RF field is neglected under the rotating wave approximation. Now the evolution of the total spin vector in the rotating frame $\tilde{\mathbf{S}}$ can be expressed as

$$\frac{d\tilde{\mathbf{S}}}{dt} = \tilde{\mathbf{S}} \times \mathbf{B}_{\mathbf{eff}} - \frac{\tilde{S}_x\hat{\tilde{\mathbf{x}}} + \tilde{S}_y\hat{\tilde{\mathbf{y}}}}{T_2} - \frac{(\tilde{S}_z - S_0)\hat{\tilde{\mathbf{z}}}}{T_1}. \tag{2.15}$$

The rate equations for each component of $\tilde{\mathbf{S}}$ can then be summarised by

$$\begin{pmatrix} \frac{d\tilde{S}_x}{dt} \\ \frac{d\tilde{S}_y}{dt} \\ \frac{d\tilde{S}_z}{dt} \end{pmatrix} = \begin{pmatrix} -\frac{1}{T_2} & \Delta\omega & -\Omega_1 \\ -\Delta\omega & -\frac{1}{T_2} & 0 \\ \Omega_1 & 0 & -\frac{1}{T_1} \end{pmatrix} \begin{pmatrix} \tilde{S}_x \\ \tilde{S}_y \\ \tilde{S}_z \end{pmatrix} + \begin{pmatrix} 0 \\ 0 \\ \frac{S_0}{T_1} \end{pmatrix}. \tag{2.16}$$

Under the condition of steady state where $\frac{d\tilde{S}_x}{dt} = \frac{d\tilde{S}_x}{dt} = \frac{d\tilde{S}_x}{dt} = 0$ the differential equations for each component have the solution

$$\tilde{S}_x = \frac{\gamma B_1 T_2}{1+\gamma^2 B_1^2 T_1 T_2 + \Delta\omega^2 T_2^2} S_0 \tag{2.17}$$

$$\tilde{S}_y = \frac{-\gamma \Delta\omega B_1 T_2^2}{1+\gamma^2 B_1^2 T_1 T_2 + \Delta\omega^2 T_2^2} S_0 \tag{2.18}$$

$$\tilde{S}_z = \frac{1+\Delta\omega^2 T_2^2}{1+\gamma^2 B_1^2 T_1 T_2 + \Delta\omega^2 T_2^2} S_0. \tag{2.19}$$

Now by making the substitution

$$\Gamma = \frac{2}{T_2}\sqrt{1+\gamma^2 B_{RF}^2 T_1 T_2/4} \tag{2.20}$$

and the approximation of low RF power $1 \gg \gamma^2 B_{RF}^2 T_1 T_2/4$, we arrive at the lineshapes for the transverse spin components

$$\tilde{S}_x(\omega_{RF}) = \frac{S_0 B_{RF}\gamma}{4}\left[\frac{\Gamma}{(\omega_{RF}-\Omega_L)^2+\Gamma^2/4}\right] \tag{2.21}$$

$$\tilde{S}_y(\omega_{RF}) = \frac{S_0 B_{RF}\gamma}{2}\left[\frac{(\Omega_L-\omega_{RF})}{(\omega_{RF}-\Omega_L)^2+\Gamma^2/4}\right] \tag{2.22}$$

which gives a Lorentzian (dispersive) lineshape centered on Ω_L for the $\tilde{S}_x$ ($\tilde{S}_y$) component where the amplitude is linearly proportional to B_{RF}. Γ now represents the *linewidth* of the magnetometer response otherwise known as the full-width at half-maximum (FWHM). In the lab frame $S_x = \tilde{S}_x \cos(\omega_{RF} t) + \tilde{S}_y \sin(\omega_{RF} t)$ and therefore by probing in the x-axis the imprinted polarisation rotation signal will be made up of the $\tilde{S}_x$ component oscillating in-phase with the RF and the $\tilde{S}_y$ component oscillating out-of-phase with the RF. Utilising a lock-in amplifier (LIA) or fast-fourier transform (FFT) it is possible to extract both lineshapes from the polarimetry signal.

2.2.4 Balanced Polarimetry

The main readout of atomic magnetometers is the measurement of the polarisation rotation of the probe beam after interaction with the atomic sample. The standard configuration of the polarimeter is shown in figure 2.4. The incident beam is split

into two paths via a polarising beam splitter (PBS) and each beam is directed onto an arm of the balanced photodiode. The two intensities I_1 and I_2 can then be used

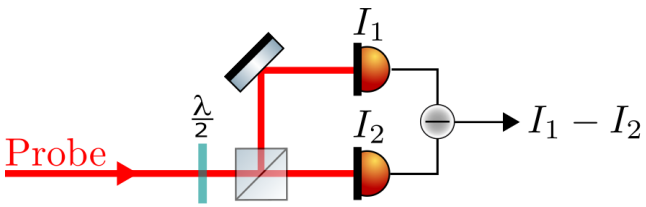

Figure 2.4: Illustration of the standard polarimeter setup to measure the probe polarisation. Here I_1 and I_2 represent the intensities seen by the two photodiodes.

to calculate the angle of polarisation ϕ

$$\phi = \frac{1}{2}\arcsin\left(\frac{I_1 - I_2}{I_1 + I_2}\right), \tag{2.23}$$

which in the limit of small angles gives

$$\phi \simeq \frac{1}{2}\left(\frac{I_1 - I_2}{I_1 + I_2}\right), \tag{2.24}$$

which shows a linear dependence on the difference between the measured beam intensities. The output of the balanced photodiode therefore gives a signal that is linearly proportional to the angle of the probe polarisation.

2.2.5 Limits of Atomic Magnetometry

2.2.5.1 Atomic Projection Noise

The spin vector can be decomposed into its projections along each axis $\vec{S} = \{S_x, S_y, S_z\}$. Since S_z is large when the sample is polarised in this direction, it can be treated as a classical variable [55, 56]

$$S_z = FN_a, \tag{2.25}$$

where F refers to the quantum number of the hyperfine level of the the atoms and N_a is the number of atoms. However the projections in the plane transverse to z are

small and hence are treated as quantum variables with a mean equal to zero

$$\langle S_x \rangle = 0; \qquad \langle S_y \rangle = 0. \tag{2.26}$$

Fluctuations of the transverse spin projections arise as a result of the Heisenberg uncertainty principle such that the uncertainty on the transverse spin components ΔS_x and ΔS_y becomes

$$\Delta S_x = \Delta S_y = \sqrt{|S_z|/2} \tag{2.27}$$

and the uncertainty on the spin vector is

$$\frac{S_\perp}{S_z} = \frac{1}{\sqrt{2S_z}} = \frac{1}{\sqrt{2FN_a}}. \tag{2.28}$$

This uncertainty sets the standard quantum limit of atomic measurement which improves with $1/\sqrt{N_a}$. The smallest detectable magnetic field in an atomic magnetometer at this limit δB_{SQL} then becomes [49, 57]

$$\begin{aligned} \delta B_{SQL} &= \frac{\hbar}{g_F \mu_B} \frac{1}{\sqrt{N_a T_2 \tau}} \\ &= \frac{\hbar}{g_F \mu_B} \frac{1}{\sqrt{nV T_2 \tau}} \end{aligned} \tag{2.29}$$

where τ is the measurement duration and V is the volume of the atomic sample. We can see that δB_{SQL} improves with increasing T_2 and this quantity generally describes the quality of the magnetic resonance. More explicitly, T_2 defines any process that causes relaxation of the magnetic sublevel oscillations (dephasing) and can be described by [51]

$$\frac{1}{T_2} = \frac{1}{T_1} + \frac{1}{q_{SE}} R_{SE} + R_{inh}, \tag{2.30}$$

where R_{SE} and R_{inh} represent the rate of relaxation due to spin-exchange collisions and due to bias field inhomogeneity respectively. Spin-exchange collisions occur when atoms exchange angular momentum with each other in an atom-atom collision and this can effectively dephase the coherent oscillations between magnetic sublevel

by providing another mechanism to change their $|F,m_F\rangle$ state other than the RF field. q_{SE} is the spin-exchange factor[2] which in the limit of $\Omega_L \gg R_{SE}$ gives the solution [58]

$$\frac{1}{q_{SE}} = \frac{2I(2I-1)}{3(2I+1)^2}, \tag{2.31}$$

where I is the nuclear spin of the atom, which gives $1/q_{SE} = 1/12$ for ^{87}Rb. The spin-exchange relaxation rate is given by [59]

$$R_{SE} = \sigma_{SE} n \bar{v} = \sigma_{SE} n \sqrt{\frac{3k_B T}{m}}, \tag{2.32}$$

where $\bar{v}$ is the average velocity of the atomic sample, σ_{SE} is the spin-exchange cross-section which is typically on the order of 1×10^{-14} cm^2 for the alkali metals. The relaxation rate due to the inhomogenous bias field is geometry dependent and it is difficult to derive a general analytical expression. However, a simplified stochastic treatment is given in [60] where for an ideal vapour cell of length L and bias gradient $\partial B/\partial z$ the following expression is derived

$$R_{inh} = \left(\frac{g_F \mu_B}{\hbar}\right)^2 \frac{L^3}{\bar{v}} \left(\frac{\partial B}{\partial z}\right)^2. \tag{2.33}$$

Due to the cubic dependence of L gradient broadening is generally more relevant for vapourcell magnetometers, where the sensor volume is typically on the order of cm.

2.2.5.2 Photon Shot Noise

Since the polarisation measurement is intrinsically a measurement of the intensities of light, the photon shot noise of the photon flux becomes a potentially limiting factor in the SNR of the polarimeter. If there are N_0 photons from the probe in the measurement duration then the amplitude of the photon shot noise A_{PSN} in the balanced case [61]

$$A_{PSN} = \langle \delta N \rangle^2 = \sqrt{N_0} \tag{2.34}$$

[2] This factor accounts for the nuclear spin of the atom in question

since the signal A_{sig} is proportional to the number of photons

$$A_{sig} = \Delta I \propto N_0 \Delta\phi \tag{2.35}$$

the polarimeter SNR then becomes

$$\phi_{SNR} = \frac{A_{sig}}{A_{PSN}} \propto \frac{N_0}{\sqrt{N_0}} = \sqrt{N_0} \tag{2.36}$$

which demonstrates that the SNR of the polarimeter increases with probe beam intensity.

2.2.6 Defining Sensitivity

The sensitivity of a device defines the degree of precision that can be assigned to the measurement. More specifically, the sensitivity is defined by the larger of the resolution step or the noise floor and is normalised to the measurement bandwidth. In magnetometry, it is useful to define two figures of merit as the *DC sensitivity*, the ability to resolve magnitude changes in a static magnetic field and the *AC sensitivity*, the ability to distinguish changes in magnitude of an oscillating magnetic field at a certain frequency. While both metrics give an idea of the performance of an RF magnetometer, for the purposes of EMI, the AC sensitivity is the important metric, giving an indication of how well the secondary field can be measured.

For both AC and DC sensitivities, it is necessary to measure the signal to noise ratio (SNR) with a lock-in amplifier or with a spectrum analyser based on the Fast Fourier Transform (FFT). It is important to recognise that the SNR is dependent on the measurement duration τ and thus sensitivities are typically normalised to this [62, 63].

2.2.6.1 AC Sensitivity

For the AC sensitivity measurement we start with a calibrated oscillating field $B_{RF}^{[REF]}$ that is within the optimal measuring range of the RF-AM. The bias field is tuned to resonance with ω_{REF}. The polarimeter signal is then recorded and passed

through an FFT algorithm to obtain the amplitude spectral density (ASD) in $\mathrm{V}/\sqrt{\mathrm{Hz}}$ at $\omega_{REF}/2\pi$. $B_{RF}^{[REF]}$ is then turned off to find the level of the noise and the SNR is recorded. The AC sensitivity dB_{AC} then becomes

$$dB_{AC} = \frac{B_{RF}^{[REF]}}{SNR}\sqrt{\tau} \tag{2.37}$$

It is conventional to express the AC sensitivity as the root-mean-square uncertainty and hence $B_{RF}^{[REF]}$ should be the rms value of the oscillation amplitude [51].

2.2.6.2 DC Sensitivity

Since B_{Bias} sets Ω_L at the Larmor frequency, DC magnetic fields are measurable in the frequency domain. The linewidth of the magnetometer Γ represents the uncertainty of the magnetometer resonance in frequency space and thus as this narrows the sensitivity of the magnetometer increases [64] according to

$$dB_{DC} = \frac{\hbar}{g_F \mu_B}\frac{\Gamma}{SNR}\sqrt{\tau}, \tag{2.38}$$

where SNR is the signal-to-noise ratio in the ASD.

2.2.6.3 Volumetric Sensitivity

The volumetric sensitivity provides an adjustment for the sensitivity based on the volume of the probe [40, 65, 66]. In the case of atomic magnetometers, this volume is defined by the intersection of probe beam and the polarised atomic medium. Considering the atomic shot noise of atomic magnetometers at the standard quantum limit in equation 2.29, we see that the sensitivity improves with $\sqrt{V}$ and so normalising by this factor allows comparison of sensors with differing probe volumes. The volumetric figures-of-merit become $dB_{AC}\sqrt{V}$ and $dB_{DC}\sqrt{V}$, typically quoted in units of $\mathrm{T}\sqrt{\mathrm{cm}^3/\mathrm{Hz}}$ [40, 67].

2.3 Laser Cooling

2.3.1 Doppler Cooling

Consider a sample of two-level atoms illuminated by a pair of counter-propagating laser beams in the x axis with frequency ω and equal intensity I. The two-level system has a resonance at a frequency of ω_0 and linewidth Γ where $\omega_0 \gg \Gamma$. Stationary atoms will experience a scattering force F on the atoms by a single beam according to its intensity and the detuning $\Delta = \omega - \omega_0$

$$\mathbf{F}(I,\Delta) = k\hbar\frac{\Gamma}{2}\frac{I/I_{SAT}}{1+I/I_{SAT}+\frac{\Delta^2}{\Gamma^2}}\hat{\mathbf{x}}, \tag{2.39}$$

where I_{SAT} is the saturation intensity of the transition. Now it is important to consider the velocity of a moving atom $\mathbf{v} = v_x\hat{\mathbf{x}}$, which will see the light Doppler shift such that the detuning becomes $\Delta = \omega - \omega_0 + k\mathbf{v}$. The total scattering force F_{TOT} felt by an atom in the x axis is then the sum of the contributions of the laser beams

$$\mathbf{F}_{TOT} = [\mathbf{F}(I,\Delta+kv_x) - \mathbf{F}(I,\Delta-kv_x)]\,\hat{\mathbf{x}}, \tag{2.40}$$

which now produces three velocity regimes of interest $\{v_x \simeq -\Delta/k, v_x = 0, v_x \simeq +\Delta/k\}$. In the case of $v_x = 0$ the scattering force contributions of the laser beams are equal and therefore cancel to $\mathbf{F}_{TOT} = 0$. In the case of $v_x \simeq \pm\Delta/k$ the atom will scatter photons mostly from the laser it is moving towards, incurring momentum kicks that oppose its motion and reduce its velocity. The process can be visualised in figure 2.5 which is split into the three different velocity regimes. This 1D scenario can then be scaled to 3D by applying additional identical pairs of counter-propagating beams in the y and z axes providing cooling for all three orthogonal directions.

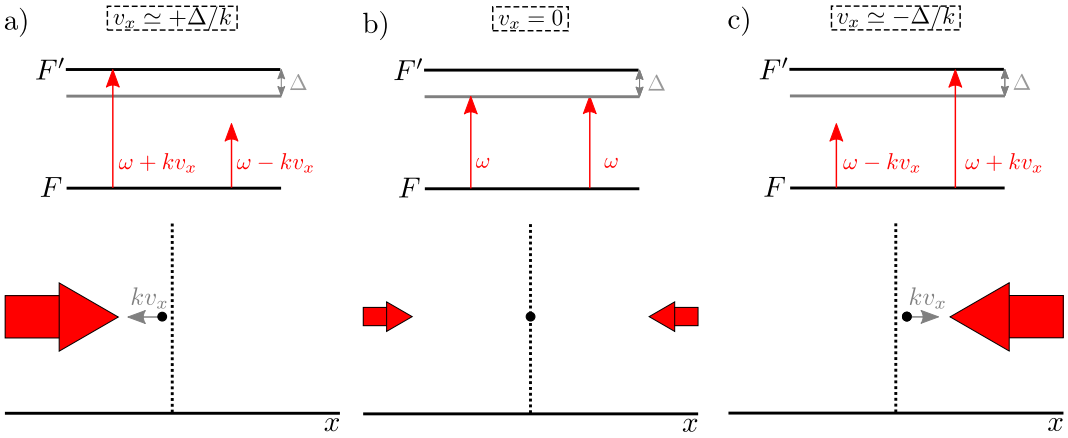

Figure 2.5: Illustration of the scattering processes occurring in each of three velocity regimes of interest. For each velocity regime, the atom is drawn (black dot) along with the laser beams (red arrows) in the spatial coordinates and above is a level diagram to represent the frequencies of the lasers as observed in the rest frame of the atom.

2.3.2 Magneto-Optical Trapping (MOT)

The magneto-optical trap combines the optical molasses with a quadrupole magnetic field which overlaps a spatially-dependent Zeeman shift onto the atoms. This then translates to a spatially-dependent and velocity-dependent scattering force which can cool and trap atoms. We consider again, the 1D molasses as discussed in section 2.3.1, but now there is a linear magnetic field gradient in the x axis $\frac{\partial B}{\partial x} > 0$ and $B = 0$ at $x = 0$. The hyperfine levels are now chosen to be $F = 0$ and $F' = 1$ such that the magnetic field will induce Zeeman splitting in the excited state m_F levels. Now the detuning that the atoms see, requires the addition of the Zeeman shift on the magnetic sublevels of the excited state. The laser beams are circularly polarised to be $\sigma^{\pm}$ polarised which selects the allowed cooling transition $|F = 0, m_F = 0\rangle \rightarrow |F' = 1, m_F = \pm 1\rangle$ accordingly. Choosing the transition which red detunes with increasing magnetic field will cause the atoms to become closer to resonance with the laser as the atoms moves further from the magnetic minimum. An anti-Helmholtz field can provide a magnetic field minimum with approximately linear gradient radially at the centre. By scaling up to the 3D optical arrangement and applying an anti-Helmholtz field centred on the point of the beam intersection, atoms can be cooled and trapped in three dimensions.

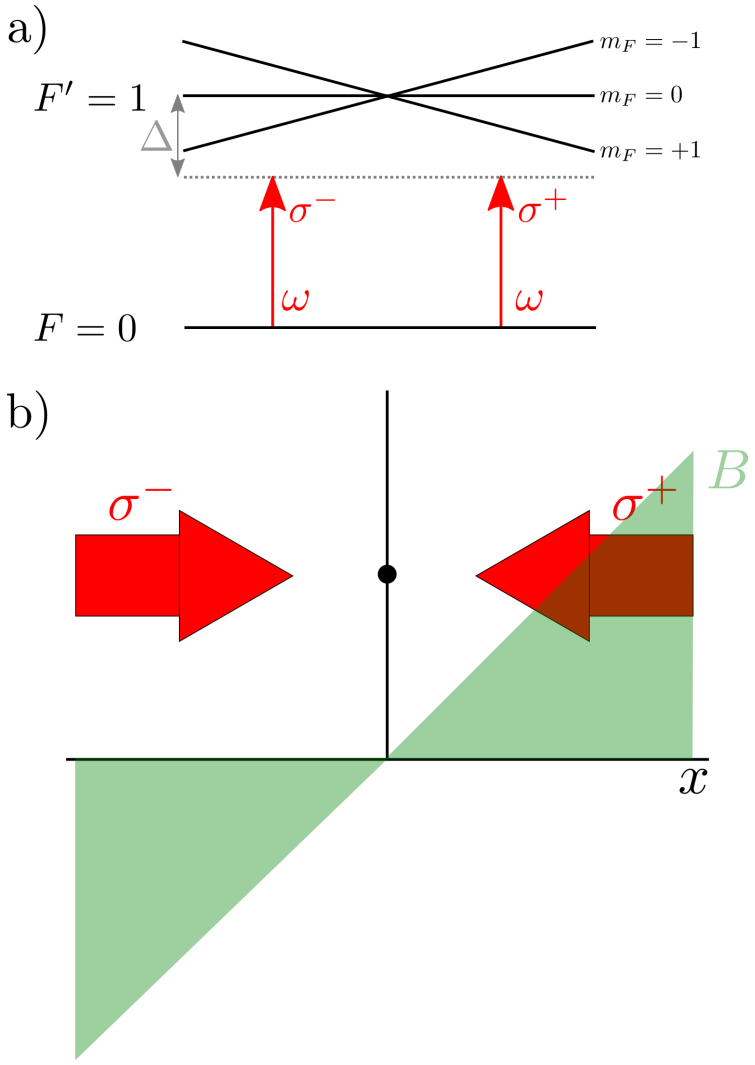

Figure 2.6: Level diagram a) of the transitions induced by the lasers and illustrative depiction of the geometry b) for the two-level MOT. In b) we see the lasers (red arrows) aimed at the centred atoms (black dot). The magnetic field strength B is plotted along the x-axis in green and this maps onto the level diagram above in a) to show the Zeeman splitting of the excited state as a function of position.

2.3.3 Polarisation Gradient Cooling

The optical arrangement of the magneto-optical trap gives rise to a secondary cooling mechanism known as polarisation gradient cooling (PGC) that acts simultaneously in the MOT. The counter-propagating beams are oppositely circularly polarised (σ^+-σ^-) and thus their interference leads to a spatially rotating linear polarisation along the axis of the beam pair. The spatially rotating linear polarisation creates population imbalance in the magnetic sublevels in the beam pair axis and gives

preferential absorption probability to the beam polarisation the atom is moving towards. This cooling scheme allows for sub-doppler cooling and is conventionally enacted sequentially after the MOT is prepared. This cooling method is also given the name *molasses cooling*.

2.3.4 Degenerate Raman Sideband Cooling (dRSC)

For further cooling of the Cs atoms to increase the phase space density (PSD) beyond that of optical molasses, degenerate Raman sideband cooling will be employed. Many experiments have used dRSC in the past to achieve a Bose-Einstein condensate of Cs atoms, yielding a high PSD with minimal atomic losses [68, 69].

Atoms begin in a far-detuned 3D optical lattice creating harmonic oscillator potentials in a spatially periodic distribution. The atoms occupy the vibrational states of the harmonic potentials with a quantum number ν such that each atom can be described to be in a state $|F, m_F, \nu\rangle$ which is illustrated in figure 2.7. Here the three lowest energy m_F sublevels of the $F = 3$ ground state are shown, with a harmonic potential well to illustrate the ν vibration levels of each m_F sublevel. A magnetic field $\mathbf{B}_{dRSC}$ is applied to induce Zeeman splitting of the $F = 3$ ground state. The magnitude of $\mathbf{B}_{dRSC}$ matches the difference in vibration level splitting such that the vibrational levels of two neighbouring magnetic sublevels $|F, m_F, \nu\rangle$ and $|F, m_F + 1, \nu - 1\rangle$ become degenerate. In the Lamb-Dicke regime, where the vibrational splitting is well resolved with respect to the atomic kinetic energy, two-photon Raman transitions induced by the lattice beams (maroon arrows) can then couple the two vibrational levels such that atoms can change vibrational state. A pump beam (blue arrows) which is resonant with $|F = 3\rangle \rightarrow |F' = 2\rangle$, optically pumps the atoms towards the stretched state $|F = 3, m_F = -3\rangle$. If the atoms decay from the $|F' = 2\rangle$ into $|F = 3, m_F = -3\rangle$ and occupy a state $|F, m_F, \nu > 1\rangle$ then Raman transitions allow the atoms to move across to other magnetic sublevels for them to again be excited by the pump beam. The state $|F = 3, m_F = -3, \nu = 1\rangle$ is the only state that is dark to both the pump beam and to the Raman transitions. After many optical pumping cycles, the atoms will build up in $|F = 3, m_F = -3, \nu = 1\rangle$

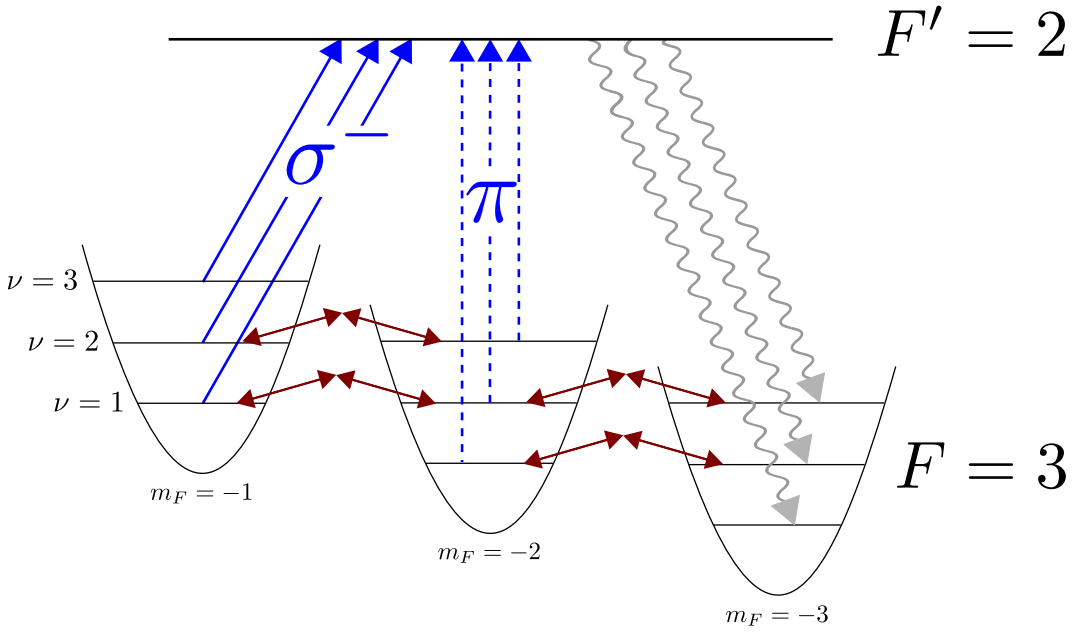

Figure 2.7: Level diagram illustrating the dRSC process in Cs. The three lowest m_F states of the $F = 3$ ground state are shown as potential wells with vibrational states induced by the optical lattice. Two-photon Raman transitions between the vibrational states are coupled via the lattice beams (maroon). The Raman pump beam (blue) provides σ^- and π light to pump into the $m_F = -3$ magnetic sublevel via spontaneous emission (grey) from the $F' = 2$ excited state.

which is the lowest energy vibrational state. The atoms therefore undergo a reduction in internal energy and thus a reduction in temperature. The π polarised portion of the pump beam prevents the formation of a dark state in $|F = 3, m_F = -2\rangle$.

A 3D optical lattice can be created from 4 linearly polarised beams propagating in the $+x$,$\pm y$ and $+z$ directions all intersecting with the atomic cloud. The total polarisation vector field $\boldsymbol{\varepsilon}$ of the four beam optical lattice can be reduced to

$$\boldsymbol{\varepsilon}(x,y,z) = \mathbf{n_x} e^{ikx} + \mathbf{n_z} e^{ikz} + \mathbf{n_y} e^{iky} + \mathbf{n_{-y}} e^{-iky}, \tag{2.41}$$

where n_i is the Jones vector of the polarisation for each lattice beam defined by

$$\mathbf{n_x} = \begin{pmatrix} 0 \\ 0 \\ 1 \end{pmatrix} \quad \mathbf{n_z} = \begin{pmatrix} 1 \\ 0 \\ 0 \end{pmatrix} \quad \mathbf{n_y} = \begin{pmatrix} \cos(\alpha_+) \\ 0 \\ \sin(\alpha_+) \end{pmatrix} \quad \mathbf{n_{-y}} = \begin{pmatrix} \cos(\alpha_-) \\ 0 \\ \sin(\alpha_-) \end{pmatrix}, \tag{2.42}$$

where α_+ and α_- are the angles of the linear polarisation of the y and $-y$ beams in the x-z plane relative to the x axis. The field defining the optical potential of the lattice can be described by [68, 70]

$$\hat{U}_{LAT} = -\frac{2}{3}U_0|\boldsymbol{\varepsilon}(x,y,z)|^2 - \frac{i}{12}U_0[\boldsymbol{\varepsilon}^*(x,y,z)\times\boldsymbol{\varepsilon}(x,y,z)]\cdot\hat{\mathbf{F}}, \tag{2.43}$$

where $\hat{\mathbf{F}}$ represents the angular momentum operator and U_0 represents the dipole potential induced by a single lattice beam. The real part of equation 2.43 is a scalar representing the optical potential that is isotropic across all the Zeeman sublevels of the ground state. The imaginary part is a vector that represents an effective magnetic field that shifts the potential according to the sublevel.

2.4 Evaporative Cooling

The MOT and molasses rely on atom-photon absorption processes which are ultimately limited by the discrete momentum change the atom undergoes when absorbing or emitting a photon. This leads to minimum temperature that is achievable via these processes, known as the *recoil temperature limit* T_{recoil} which is described by [71]

$$T_{recoil} = \frac{k^2\hbar^2}{mk_B} \tag{2.44}$$

which gives $T_{recoil} = 198\,\text{nK}$ (362 nK) for ^{133}Cs (^{87}Rb). To reach sub-recoil temperatures, it is customary to utilise cooling processes that do not require absorption of photons. During evaporative cooling, the more energetic atoms are removed from the trap and the ensemble will rethermalise [72]. To create a trapping potential without atom-photon absorption processes, it is conventional to use the magnetic trap (MT) and/or very far-detuned dipole trap (DT), which take advantage of the Zeeman effect and light shift respectively, to change the internal energy of the atoms without the absorption of a photon. The process of evaporation can then be implemented by removing the atoms with a selectively-perturbing interaction known as *forced evaporation* or by reducing the trap-depth to allow the hottest atoms to

escape the trap, known as *passive evaporation*.

2.4.1 Magnetic Trapping

The energy of an atom U in a magnetic field B can be described by the Zeeman splitting in equation 2.4. The force on an atom in a spatial magnetic gradient therefore becomes

$$F = -\nabla \cdot U = -\left\{ \hat{\mathbf{x}}\frac{\partial}{\partial x} + \hat{\mathbf{y}}\frac{\partial}{\partial y} + \hat{\mathbf{z}}\frac{\partial}{\partial z} \right\} g_F \mu_B m_F B, \tag{2.45}$$

At the centre of an anti-Helmholtz coil pair the magnetic vector field has the form

$$\mathbf{B}_{AH} = \frac{b'_z}{2}(x\hat{\mathbf{x}} + y\hat{\mathbf{y}} - 2z\hat{\mathbf{z}}), \tag{2.46}$$

where b'_z is the axial magnetic field gradient of the anti-Helmholtz pair. The force on the atoms in the MT therefore becomes

$$F_{MT} = -g_F \mu_B m_F \nabla \cdot |\mathbf{B}_{AH}| = -g_F \mu_B m_F \frac{b'_z}{2}\sqrt{x^2 + y^2 + 4z^2}, \tag{2.47}$$

which provides an antisymmetric linearly changing positional dependent force along any vector from the centre of the trap. The sign of F_{MT} ultimately depends on the $|F, m_F\rangle$ state of the atom and thus the magnetic trap becomes a state-dependent trapping potential, which becomes useful in forced evaporation and in state preparation. To reach potential depths deep enough to trap atoms at the 10 µK level the magnetic trap requires very high magnetic gradients ($\sim$100 G/cm). The state-dependent nature of the trapping potential also leads to several trap escape processes. Spin-exchange collisions between atoms facilitate transition from a trappable m_F state to an untrappable or anti-trappable state which leads to losses [73]. At the centre of the trap where $B \simeq 0$ the m_F states become nearly degenerate to a point where the Zeeman splitting is so narrow that perturbations from ambient noise can provide coupling from trapped to un(anti-)trappable states. This effect is known as the *Majorana losses* and can be circumvented by offsetting the trap centre from magnetic zero, either with an DC magnetic field or a plug beam [74].

The m_F transitions in the MT can be taken advantage of, to induce forced evaporation. From equations 2.46 and 2.47 we see that $|\mathbf{B}_{AH}|$ increases radially from the trap centre and therefore the energy shifts due to the Zeeman effect will also increase radially. It is then possible to selectively excite the atoms radially with the application of an RF magnetic field B_{knife} tuned to the frequency that corresponds to the Zeeman splitting at that radius. B_{knife} provides coupling of the atoms from a trappable to an un(anti-)trappable state and the atom is removed from the trap. Since the most energetic atoms will occupy the peripherals of the trapping potential, ω_{knife} can be progressively swept to lower frequencies to cut the distribution at progressively lower temperatures.

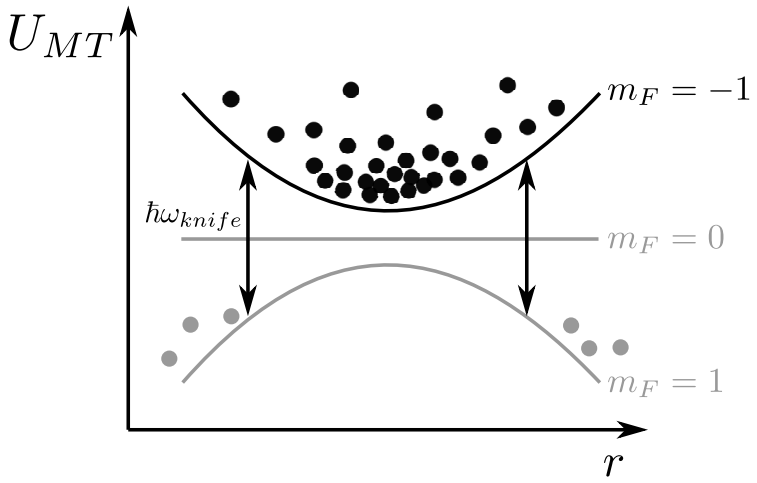

Figure 2.8: Illustrative depiction of the process of forced evaporation from the MT in the $F = 1$ ground state of ^{87}Rb. B_{knife} transfers the hotter atoms trapped in the $m_F = -1$ state, to the un(anti-)trapped state of $m_F = 0$ ($m_F = +1$) where they leave the MT.

Figure 2.8 shows a depiction of this process for an atom magnetically trapped in the $F = 1$ ground state. The $m_F = -1$ sublevel becomes the trapped state and B_{knife} couples the atoms to the un(anti-)trapped state of $m_F = 0$ ($m_F = +1$) where they leave the trap.

2.4.2 Dipole Trapping

2.4.2.1 Light Shift

The coupling strength of an atom to a photon driving a transition $i \rightarrow j$ at a resonant frequency ω_0 can be characterised by the Rabi frequency Ω

$$\Omega_{i,j} = \frac{\hat{E} \cdot \hat{d}_{i,j}}{\hbar}. \tag{2.48}$$

where $\hat{d}_{i,j}$ is the transition dipole moment for a transition $i \rightarrow j$. The light shift gives the relative frequency shift of the levels $\Delta\omega$ in the transition due to the applied electric field of the light

$$\Delta\omega = \frac{\Omega_{i,j}^2}{4\omega_0}. \tag{2.49}$$

2.4.2.2 Dipole Force

The dipole force F_{dip} arises as a consequence of a spatially changing light shift [48]

$$\mathbf{F}_{dip} = -\nabla \cdot U_{dip} = -\left\{ \hat{\mathbf{x}}\frac{\partial}{\partial x} + \hat{\mathbf{y}}\frac{\partial}{\partial y} + \hat{\mathbf{z}}\frac{\partial}{\partial z} \right\} \frac{\hbar\Omega_{i,j}^2}{4\omega_0}. \tag{2.50}$$

The intensity profile of a focussed gaussian laser beam propagating in an axis z has the form

$$I(z,r) = \frac{P}{\pi w(z)^2} \exp\left\{ -\frac{2r^2}{w(z)^2} \right\}, \tag{2.51}$$

where P is the total beam power and r is the radial position from the centre of the beam. The radius of the focussed Gaussian w beam will converge to its minimum value w_0 along the beam axis z according to

$$w(z) = w_0 \sqrt{1 + \left(\frac{z-f}{z_R} \right)^2}, \tag{2.52}$$

where z_R is the Rayleigh length of the focus and f is the focal length of the lens[3] used to focus the beam. From equations 2.51 and 2.52 we see that the focussed gaussian beam has an intensity maximum at the focus. For a linearly polarised

[3] This will usually be a planoconvex lens.

beam that is sufficiently detuned $\Delta \gg \Gamma$ the optical potential is

$$U_{dip} = -\frac{3c^2}{2\omega_0^3}\frac{\Gamma}{\Delta}I(z,r). \tag{2.53}$$

We can see that the sign of the detuning determines the sign of the potential created. If the beam is red-detuned, the intensity maximum of a focussed laser becomes a potential minimum which allows for confinement in the beam both axially and radially. In general, the intensity gradient is much sharper radially than it is axially, and so trapping along the beam axis is much weaker. Therefore most experimental geometries will utilise the *crossed dipole trap* (XDT) whereby two orthogonally directed beams intersect at their foci. This prevents axial atom loss by providing a steep intensity gradient in all 3 dimensions.

For very far detuned beams ($\Delta > |\omega_{D1} - \omega_{D2}|$) the fine structure needs to be taken into account as the beam will have comparable coupling to both the D_1 and D_2 line

$$U_{dip} = -\frac{1}{2}\pi c^2 \left(\frac{2\Gamma_{D2}}{\omega_{D2}^3}\left[\frac{1}{\omega_{D2}-\omega} + \frac{1}{\omega_{D2}+\omega}\right] + \frac{\Gamma_{D1}}{\omega_{D1}^3}\left[\frac{1}{\omega_{D1}-\omega} + \frac{1}{\omega_{D1}+\omega}\right]\right) I(z,r), \tag{2.54}$$

where ω_{D1} (ω_{D2}) and Γ_{D1} (Γ_{D2}) are the resonant frequency and the spontaneous decay rate of the D_1 (D_2) line.

Passive evaporation in the dipole trap can be performed via the *trap weakening method* [75, 76] whereby the dipole beam powers are ramped down to reduce the trap depth. As the trap depth reduces, the most energetic atoms escape and the atomic ensemble (after many atom-atom collisions) will rethermalise to a lower average temperature.

2.5 Bose-Einstein Condensation

For a classical gas, atoms are generally modelled ballistically and the wave nature of the individual atoms is neglected. When the temperature becomes so low that the

characteristic de Broglie wavelength λ_{DB} of the whole ensemble [77]

$$\lambda_{DB} = \sqrt{\frac{2\pi\hbar^2}{mk_BT}} \tag{2.55}$$

is on the order of the inter-atomic separation, the wavefunctions of the individual atoms begin to overlap and interfere. For bosons such as ^{87}Rb and ^{133}Cs, atoms can begin to macroscopically occupy the lowest quantum state and thus cross a phase-transition from a classical gas into a Bose-Einstein condensate (BEC). At this point, the entire atomic ensemble can be described by a single wavefunction. The phase-space density D

$$D = n\lambda_{DB}^3, \tag{2.56}$$

gives a metric for describing the degree of overlap between the atomic wavefunctions. The phase-space density value of criticality for the BEC transition D_c varies for different confining potential geometries and for a non-interacting Bose gas in a harmonic oscillator $D_c = \zeta(3/2) \simeq 2.61$ where ζ is the Riemann zeta function. In the following I will utilise the derivations in [78, 79] to outline the thermodynamics of the transition from classical gas to BEC.

2.5.1 Ideal Bose Gas in Harmonic Potential

Consider an ideal Bose gas of N bosons confined in a harmonic oscillator potential $U(\mathbf{r})$ of the form [78, 80]

$$U(\mathbf{r}) = \frac{1}{2}m\left[\omega_x^2x^2 + \omega_y^2y^2 + \omega_z^2z^2\right], \tag{2.57}$$

where $\omega_{x,y,z}$ represent the trap frequencies in each axis. The atoms fill into discrete energy levels denoted by the quantum numbers $n_{x,y,z}$ where the distribution of the total population N can be described in the grand canonical ensemble with chemical potential μ

$$N = \sum_k b_k = \sum_{n_x,n_y,n_z}^{\infty} \frac{1}{e^{\beta(\varepsilon_{n_{x,y,z}} - \mu)} - 1}, \tag{2.58}$$

where $\beta = 1/k_B T$ and $\varepsilon_{n_{x,y,z}}$ defines the energy of the level $n_{x,y,z}$. It is useful to separate the ground state population N_0 from the ensemble such that the summation then becomes

$$N = N_0 + \sum_{n_x,n_y,n_z \neq 0}^{\infty} \frac{1}{e^{\beta\hbar(\omega_x n_x + \omega_y n_y + \omega_z n_z)} - 1}. \tag{2.59}$$

Provided $k_B T \gg \hbar\bar{\omega} = \hbar(\omega_x + \omega_y + \omega_z)/3$ the energy level spacing can be taken to be continuous and thus the summation in equation 2.59 can be solved as an integral

$$N - N_0 = \int_0^{\infty} \frac{1}{e^{\beta\hbar(\omega_x n_x + \omega_y n_y + \omega_z n_z)} - 1} dn_x dn_y dn_z, \tag{2.60}$$

With a change of variables ($\beta\hbar\omega_{x,y,z} n_{x,y,z} = n'_{x,y,z}$) the solution to the integral becomes

$$N - N_0 = \zeta(3) \left(\frac{k_B T}{\hbar\omega_{HO}} \right)^3, \tag{2.61}$$

where $\zeta(3) \approx 1.202$ and $\omega_{HO} = \sqrt[3]{\omega_x \omega_y \omega_z}$ is the geometric average trap frequency of the harmonic oscillator. At the condition of criticality, $T = T_c$ and N_0 vanishes, the number of atoms N_c becomes

$$N_c = \zeta(3) \left(\frac{k_B T_c}{\hbar\omega_{HO}} \right)^3 \tag{2.62}$$

and therefore the condensed fraction N_0/N can be written as

$$\frac{N_0}{N} = 1 - \left(\frac{T}{T_c} \right)^3 \tag{2.63}$$

2.5.2 Interacting Bose-Einstein Condensate

Below the critical temperature, the atoms condense into the BEC phase and are so cold that their interatomic interactions create an additional potential term. The atoms in the ground state can then be collectively described by one many-body wavefunction $\psi(\mathbf{r})$ in the Gross-Pitaevskii equation [79]

$$i\hbar\frac{d\psi}{dt} = -\left[\frac{\hbar^2}{2m}\nabla^2 + U(\mathbf{r}) + \tilde{U}|\psi|^2\right]\psi \tag{2.64}$$

where $\tilde{U} = 4\pi\hbar^2 a/m$ describes the two-body interactions at an s-wave scattering length a and $|\psi|^2$ is the atomic density. The density profile of the condensate can then be explored for different interaction strengths. In the *ideal-gas limit* the interactions are weak such that $(n\tilde{U} \ll \hbar\omega_{x,y,z})$ and therefore the kinetic energy term of the GPE dominates and interactions are ignored. The wavefunction of the condensate then matches that of the ground state of the harmonic oscillator and gives a gaussian density profile in the form

$$n_c(\mathbf{r}) = \frac{N}{\pi^{3/2}}\prod_{i=x,y,z}\frac{1}{\sigma_i}e^{-i^2/\sigma_i^2} \tag{2.65}$$

where σ_i gives the width of the condensate in axis i. In the trap the width is confined to the harmonic oscillator as $\sigma_{i,OH}$ and when released, expands ballistically after some time-of-flight t_{TOF} to a width $\sigma_{i,EX}$ according to

$$\sigma_{i,EX}^2 = \sigma_{i,OH}^2 + v_{i,OH}^2\, t_{TOF}^2 \tag{2.66}$$

where $v_{i,OH}$ is the velocity of the condensate in axis i when trapped in the harmonic oscillator. In the *Thomas-Fermi limit* the interactions are strong $(n\tilde{U} \gg \hbar\omega_{x,y,z})$ such that the interaction term of the GPE dominates and the kinetic term can be ignored. The condensate now takes a density profile in the form

$$n_c(\mathbf{r}) = \max\left(\frac{\mu - U(\mathbf{r})}{\tilde{U}}, 0\right) = \frac{15}{8\pi}\frac{N}{\prod\sigma_i}\max\left(1 - \sum_{i=x,y,z}\frac{i^2}{\sigma_i^2}, 0\right) \tag{2.67}$$

which gives rise to a parabolic shape in the density profile of the condensate. This parabolic shape is used to identify the BEC after evaporative cooling and can be used to reveal the condensed fraction in the sample [81, 82].

Chapter 3

EMI with a Mechanically-Translatable RF-AM

Using RF-AMs for practical applications requires sensors that are robust in the real world. Currently most RF-AMs are laboratory-based, stationary and bulky, which limits their competitiveness with existing solutions. In this chapter, I outline the design and implementation of a mechanically translatable RF-AM operating with a miniaturised sensor head and external stationary control electronics. Early work on the design and construction of the sensor head was done by Dr Cameron Deans and the raw data used for several figures (marked in their respective captions) in the first section of this chapter are derived from his test data. The setup presents a significant step to implementing EMI with RF-AMs in a real world environment where size and movement constraints are usually intolerable. The work in this chapter led to the following publications:

- C. Deans, Y. Cohen, H. Yao, B. Maddox, A. Vigilante, and F. Renzoni, "Electromagnetic induction imaging with a scanning radio frequency atomic magnetometer," *Applied Physics Letters*, vol. 119, no. 1, p. 014001, 2021
- B. Maddox, Y. Cohen, and F. Renzoni, "Through-skin pilot-hole detection and localization with a mechanically translatable atomic magnetometer," *Applied Physics Letters*, vol. 120, no. 1, p. 014002, 2022

3.1 Sensor Head Setup

3.1.1 Main Setup

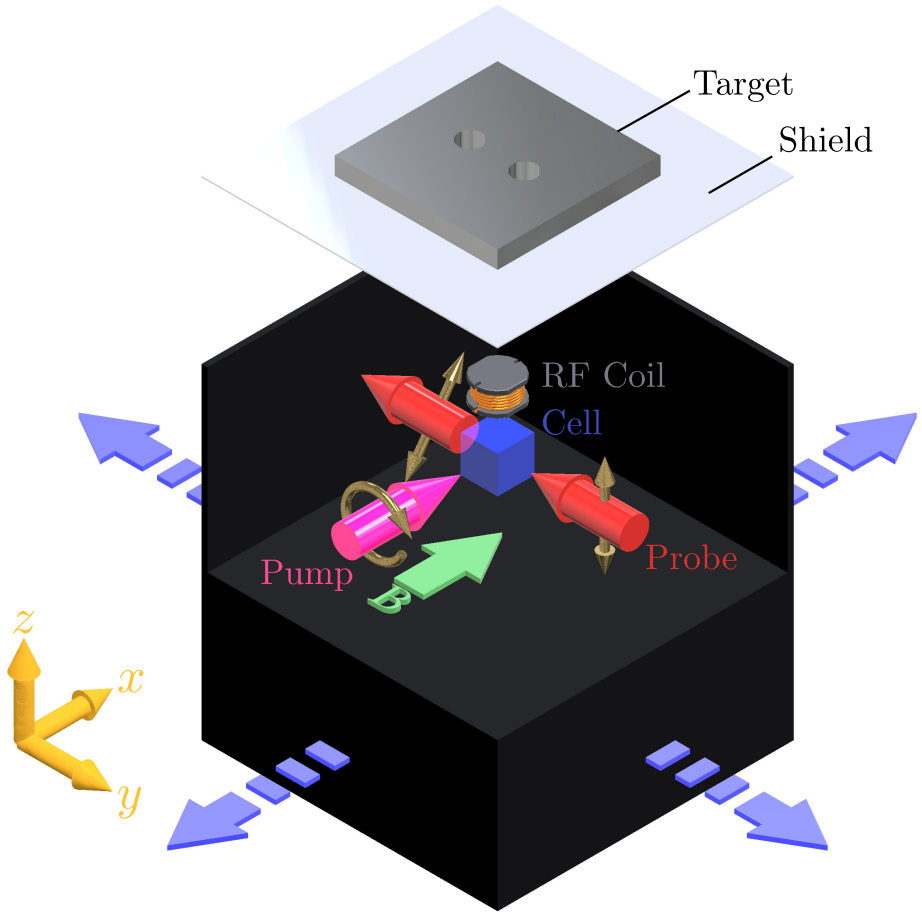

Figure 3.1: Simplified diagram of the mechanically-translatable RF-AM setup with respect to the target during the imaging procedure. The target shown is the aluminium pilot-hole target piece used in section 3.3. Red, magenta and green arrows show the probe, pump and bias field geometries respectively with golden arrows showing polarisation of the laser beams. Blue arrows indicated the 2D mechanical translation of the sensor-head. Figure appears in [6].

Figure 3.1 shows a simplified schematic of the sensor head for the mechanically translatable RF-AM. The sensor head, of dimensions $110 \times 110 \times 145\,\text{mm}^3$ (L×W×H)[1], is made of 3D printed nylon and houses all of the optical and mag-

[1]Length, width and height correspond to the dimensions in the x, y and z axes of figure 3.1 respectively.

netic apparatus in a package that weighs 1.49 kg. All the control electronics[2] are stationary and externally connected to the sensor head via cables. Inside the sensor head, a circularly polarised pump beam, resonant with the $|F=1\rangle \rightarrow |F'\rangle$ transition in the D_1 line of ^{87}Rb, propagates through the vapour cell along a bias field B_{Bias} generated in the x-axis. This then spin-polarises the sample with a ground state splitting of $\Omega_L = \gamma_{Rb} B_{Bias}$. An RF coil above the vapour cell then generates the oscillating magnetic field B_{RF} and drives the transitions in the magnetic sub-levels. This is then read off by the linearly polarised probe beam, red-detuned from the $|F=1\rangle \rightarrow |F'\rangle$ transition in the D_1 line of ^{87}Rb, which propagates through the cell in the $-y$-direction. The probe is then directed onto a miniaturised polarimeter which is housed in the sensor head. Three square Helmholtz coils with dimensions $100 \times 100\,\text{mm}^2$ are orthogonally aligned and centred on the cell providing active compensation of the internal DC magnetic fields. A three-axis fluxgate sensor is placed close to the cell to feedback to PID controllers which lock field in the x-axis to B_{Bias} and the transverse fields in y and z to zero. The whole sensor head is mounted on a large 2D translational stage which can translate it in the x-y plane, allowing the sensor to be raster scanned about a target object placed on a plastic screen above. Figure 3.2 shows a typical resonance recorded at $\Omega_L = 102\,\text{kHz}$, the lineshapes match the expected result of an in-phase Lorentzian and out-of-phase dispersive shape as seen in equations 2.21 and 2.22 respectively. What can also be extracted is the typical linewidth of the RF-AM which yields $\Gamma = 2\pi \times 1.8\,\text{kHz}$.

[2]Including: laser temperature/current controllers, PID controllers for the compensation coils, lock-in amplifier and computer control.

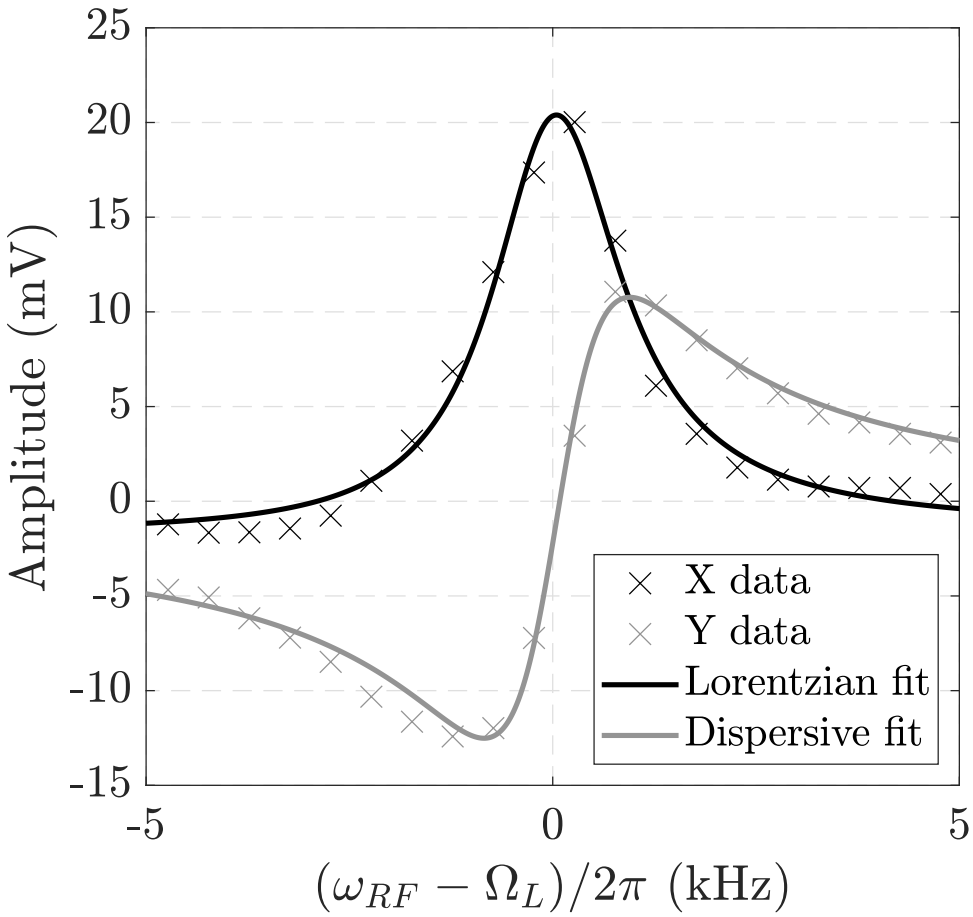

Figure 3.2: Typical magnetic resonance for the mechanically translatable RF-AM at $\Omega_L = 102\,\text{kHz}$. Black (grey) crosses show the data extracted from the X (Y) channel of the lock-in amplifier as Ω_{RF} is swept. The solid black (grey) line shows the fitted Lorentzian and dispersive lineshapes.

3.1.2 Vapour Cell

The vapour cell is a cubic ($25\,\text{mm} \times 25\,\text{mm} \times 25\,\text{mm}$) glass cell filled with isotopically enriched ^{87}Rb metal and 20 Torr of N_2 as a buffer gas. The buffer gas reduces the mean free path of the atoms which reduces atom-wall collisions that act to depolarise the atoms. The buffer gas introduces collisional broadening of the ^{87}Rb D_1 line at a rate of 16.3 MHz/Torr [83]. This adds $\Gamma_L/2\pi = 326\,\text{MHz}$ of collisional broadening to the atomic resonances in the vapour cell, along with the comparable doppler broadening of $\Gamma_G/2\pi = 501\,\text{MHz}$ at room temperature (300 K). The cell can be seen as a blue cube in figure 3.1 and is centred in the sensor head under the RF coil. A small AC heater circuit is wrapped around the cell to provide heating

above room temperature,[3] if required.

3.1.3 Lasers

Laser light is generated within the sensor head by two vertical-cavity surface-emitting lasers (VCSELs) from VIXAR (i0-0795s-0000-bc06). Both lasers were collimated at a diameter of 10 mm. These lasers emit at $\lambda = 795 \pm 0.5$ nm, have a large linewidth (≤ 100 MHz) and low wavelength-temperature coefficient (0.055 nm/K) which makes them stable enough to park on the atomic transitions without needing readjustment for several days. The redundancy of active frequency locking allows the laser system to be simplified and compacted. To find the atomic transitions, the magnetometer signal itself can be used for spectroscopy. Figure 3.3 shows the level diagram of the ^{87}Rb D_1 line, showing the pump and probe detunings.

[3] For initial testing measurements were performed at 40 °C but for imaging, the cell was left at room temperature 21 °C

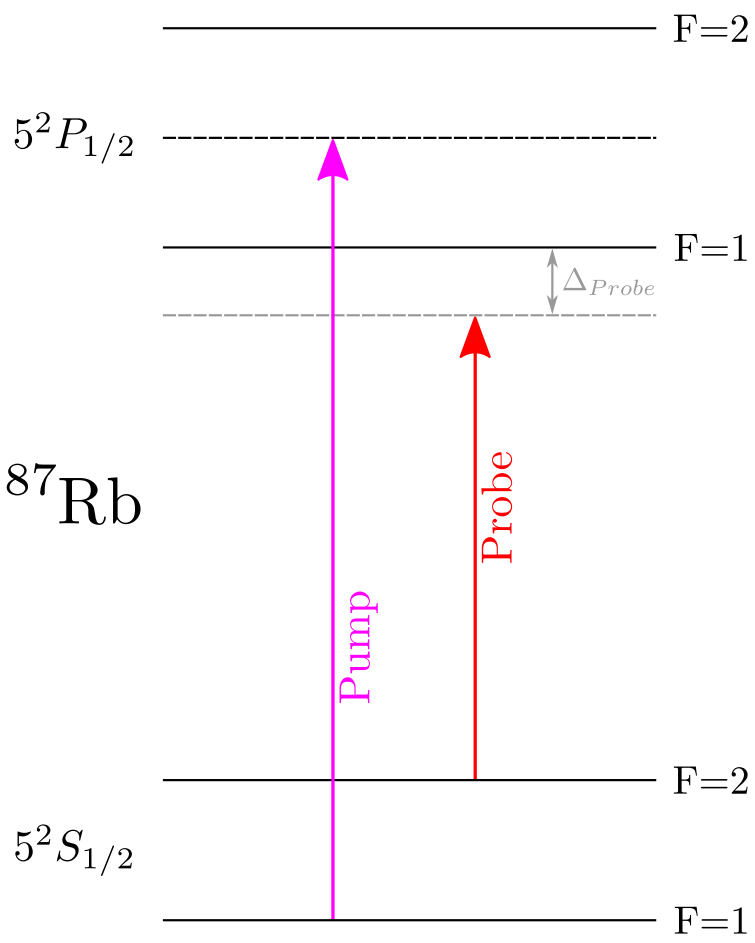

Figure 3.3: Level diagram of the ^{87}Rb D_1 line [84] showing the tuning of the near-resonant beams with respect to the hyperfine transitions.

3.1.4 Pump Beam

Since the amplitude of the magnetometer signal is proportional to the polarisation of the vapour, it is possible to infer the ground state spectrum from the magnetometer response. With the probe beam parked on the $|F = 2\rangle \rightarrow |F'\rangle$ transition, the pump laser current was manipulated to sweep the frequency of the pump laser. Magnetic resonances were then built up by sweeping ω_{RF} at each pump detuning and the maximum amplitude was outputted. Figure 3.4 shows the results of this with two clear peaks in the spectrum separated by $\simeq$7.5 GHz. While this splitting is not exactly the ground state hyperfine splitting of 6.85 GHz [84] it is enough to identify the transitions[4]. The difference in amplitudes of the peaks arises due to the probe

[4]Inaccuracy in the splitting likely comes as result of departure from the nominal wavelength-current coefficient of 0.4 nm/mA, due to inconsistencies in the manufacturing process.

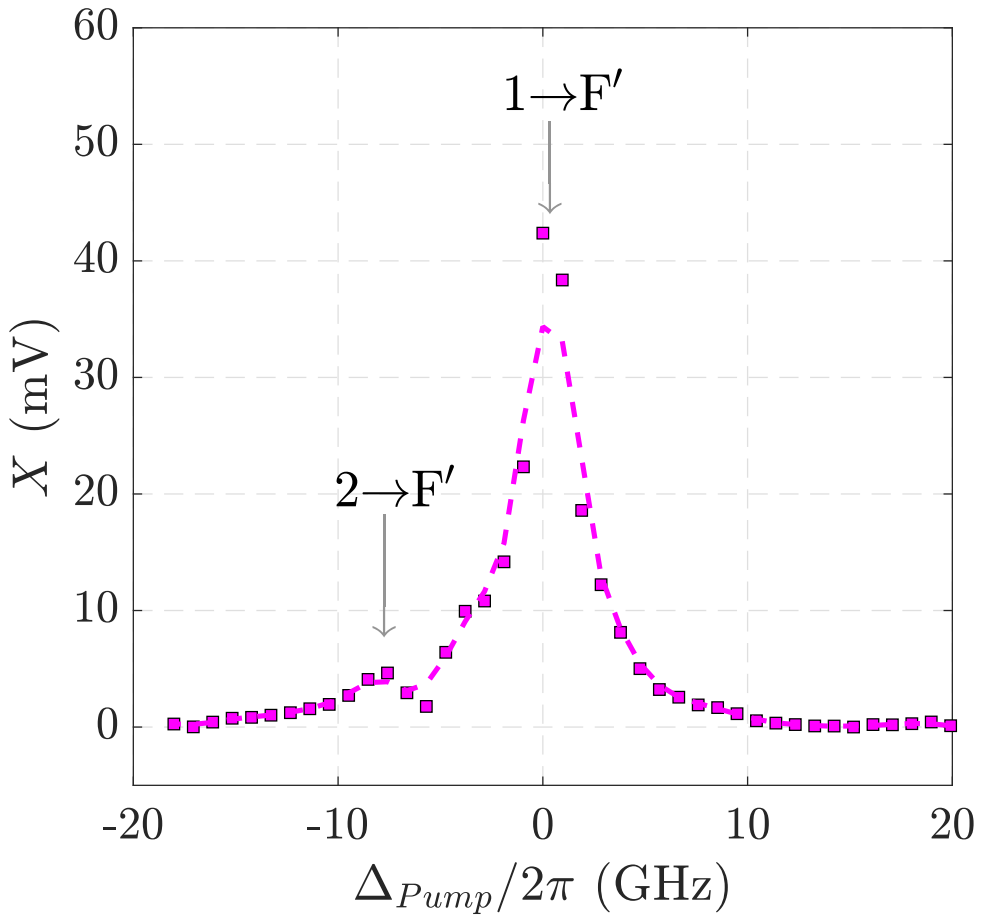

Figure 3.4: X amplitude of the magnetometer resonance as a function of pump detuning Δ_{Pump}. Δ_{Pump} is centred on the $|F=1\rangle \rightarrow |F'\rangle$ transition identified by eye. The dashed magenta line shows a smoothed average while grey arrows point to the features in the spectrum with annotations $F \rightarrow F'$ as shorthand for $|F\rangle \rightarrow |F'\rangle$. The probe frequency was parked on the $|F=2\rangle \rightarrow |F'\rangle$ transition. The frequency space is calibrated from the wavelength-current coefficient found in the VCSEL datasheet. Raw data was taken by Cameron Deans.

being sufficiently more detuned from atoms in the $F=1$ ground state than the atoms in $F=2$.

3.1.5 Probe Beam

With the pump parked on the $|F=1\rangle \rightarrow |F'\rangle$ transition, the probe could then be tuned. Again, in the same process as for the pump, the probe detuning Δ_{Probe} was swept across the transitions and the maximum amplitude recorded. The results can be seen in figure 3.5a along with the expected $\mathbb{I}\mathrm{m}\{\bigvee\}$ in figure 3.5b. $\mathbb{I}\mathrm{m}\{\bigvee\}$ is

calculated with equation 2.10[5] and is proportional to the optical rotation. As the frequency splitting of the excited state is 816.7 MHz and therefore comparable to the pressure broadening and Doppler broadening, the contributions from each of the transitions $|F=2\rangle \rightarrow |F'=1,2\rangle$ will blur together to form one large dispersive curve[6]. The result of detuning the probe therefore shows a response that is con-

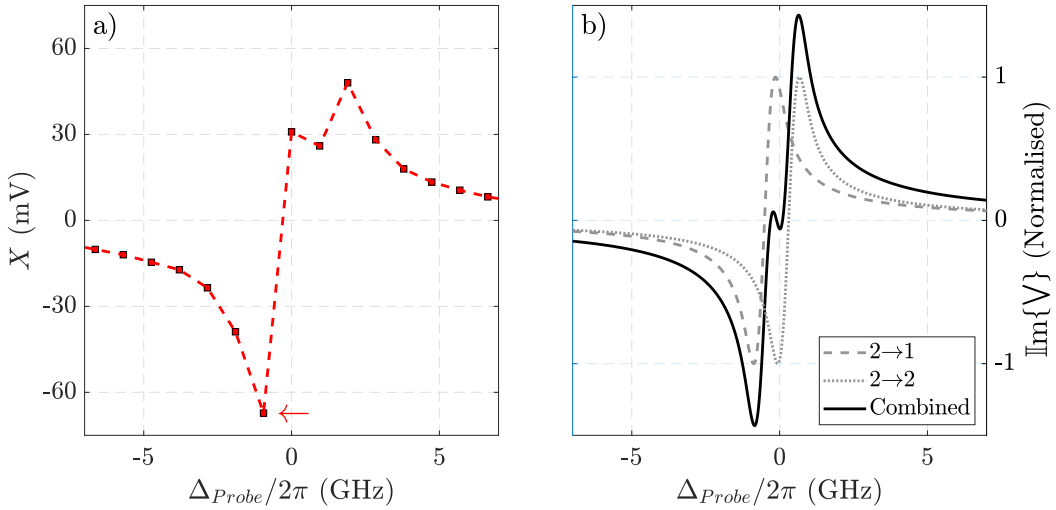

Figure 3.5: X amplitude a) of the magnetometer resonance as a function of probe detuning Δ_{Probe}, compared with the normalised imaginary part of the calculated Voigt profile $\mathbb{I}\text{m}\{\mathcal{V}\}$ b). In a) the frequency space is calibrated from the wavelength-current coefficient found in the VCSEL datasheet and the pump frequency was parked on the $|F=1\rangle \rightarrow |F'\rangle$ transition. In b) the grey dashed and dotted lines show the individual contributions of the two hyperfine transitions while the black solid line shows the combined Voigt profile. $F \rightarrow F'$ is shorthand for $|F\rangle \rightarrow |F'\rangle$. Raw data in a) was taken by Cameron Deans.

sistent with the expectation. For tuning simplicity, the probe beam is parked at a frequency which maximises the magnetometer amplitude which from figure 3.5a appears as the negative peak of the dispersive[7] which we can therefore infer to be $\Delta_{Probe}/2\pi \simeq -1\,\text{GHz}$ from the $|F=2\rangle \rightarrow |F'=1\rangle$ transition.

3.1.6 Bias field Compensation

Bias field stabilisation becomes critical for unshielded magnetometers, as low frequency fluctuations in the background magnetic field lead to perturbations of Ω_L

[5] Calculated with equation 2.10 using the values of Γ_G and Γ_L discussed in section 3.1.2.

[6] The hyperfine transition strengths of both transitions are identical [84] and therefore give an equal contribution to the combined Voigt profile.

[7] Red arrow in figure 3.5a

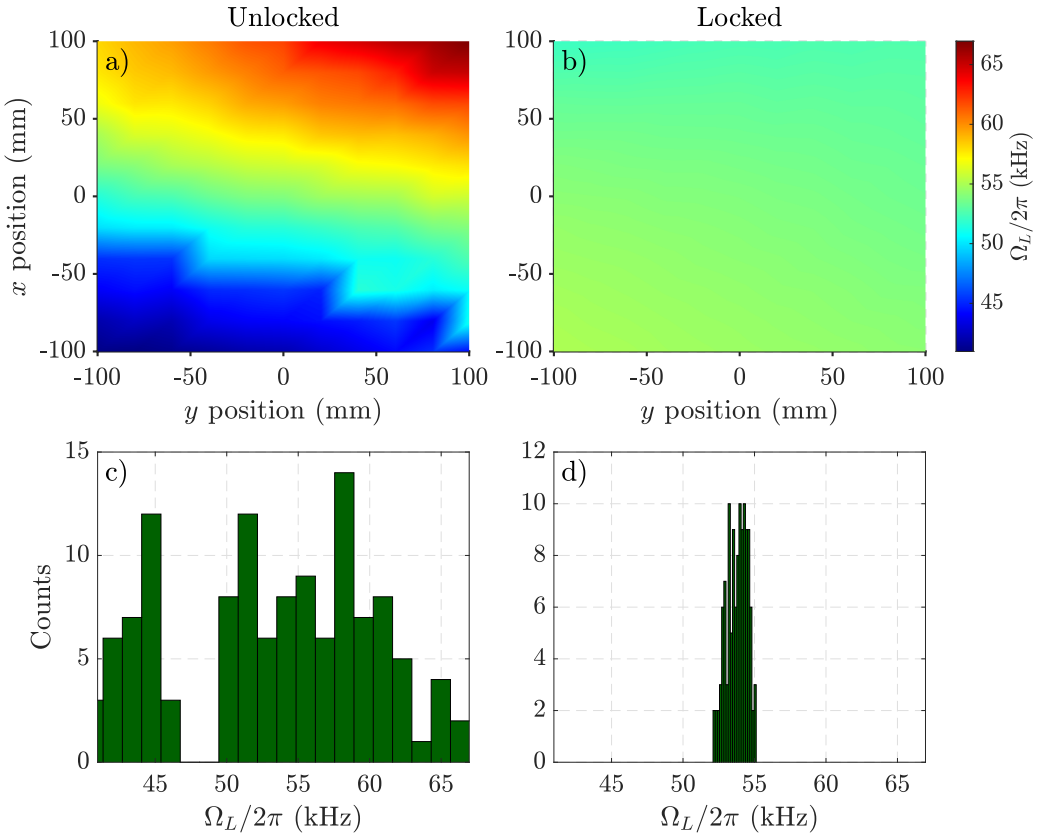

Figure 3.6: Resonant frequency Ω_L of the mechanically translatable RF-AM mapped spatially with the transverse and bias magnetic fields unlocked a) and locked b) along with corresponding histogram plots c) and d).

which can lead to linewidth broadening [2]. For the mechanically translatable RF-AM this becomes ever more challenging due to the spatial inhomogeneity of background magnetic fields in typical laboratory settings. Figure 3.6 shows how Ω_L changes over the measurement area for the case where the compensation coils are locked with the PID or left unlocked. For the unlocked case, the bias coil was fixed at the field that gave $\Omega_L = 54\,\text{kHz}$ at the origin with the transverse magnetic coils deactivated. The sensor head was then translated around the measurement area and magnetic resonances were built up at each point, with Ω_L extracted from the fitting procedure. The same is then done in the locked case, but now with the PID feeding back the fluxgate sensor voltage to the PID to lock the bias and the transverse fields with the compensation coils. As it can be seen from the figure, the magnetic compensation system is essential to the spatial stability of Ω_L, with the range of frequen-

cies decreasing by an order of magnitude from $\delta\Omega_L/2\pi \simeq 30\,\text{kHz}$ for the unlocked case, to $\delta\Omega_L/2\pi \simeq 3\,\text{kHz}$ for the locked case. The residual $\delta\Omega_L/2\pi \simeq 3\,\text{kHz}$ for the

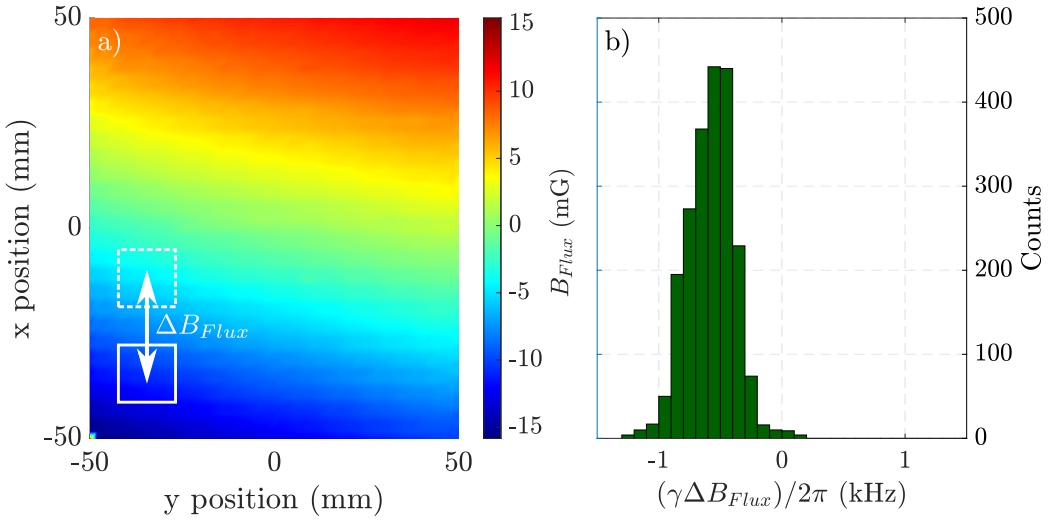

Figure 3.7: Unlocked measurement of background magnetic field in the bias direction with the fluxgate B_{Flux} mapped spatially with the mechanically translatable RF-AM a) normalised to the origin. The white dashed (solid) box represents the rough geometry of vapour cell (fluxgate) to demonstrate how ΔB_{Flux} is calculated for the histogram that appears in b).

locked case still presents a limit to the device spatial stability and can be explained by the non-zero displacement between the fluxgate sensor and the vapour cell. For compactness, only one fluxgate sensor is used to approximate the magnetic field felt by the cell. This is displaced by $-20\,\text{mm}$ from the cell, in the bias direction[8]. Figure 3.7a shows the change in measurement of the fluxgate sensor B_{Flux} against displacement from the origin as a spatial map, with the PID unlocked and transverse coils deactivated. From here, we can see the natural background magnetic gradient in the bias direction, that appears in the laboratory. By applying the geometry of the fluxgate-vapour cell spacing (white dashed and solid boxes) we can calculate the discrepancy ΔB_{Flux} between the field that the fluxgate feels, versus the vapour cell. Since the PID loop reacts to B_{Flux} and not the field felt at the cell, the vapour cell will see a field that is $B_{Flux} + \Delta B_{Flux}$ and thus if the gradient is spatially varying then this will cause a change in Ω_L over the measurement area, regardless of active compensation. ΔB_{Flux} can then be extracted from the data, converted to frequency

[8] Along x axis in figure 3.1.

space and plotted in a histogram in figure 3.7b. We can see that the width of this histogram is about 1 kHz which is comparable to that extracted from the magnetometer resonances in figure 3.6d. While active compensation in this arrangement does well, a 3 kHz spatial deviation in Ω_L becomes comparable to the linewidth of the magnetometer and would decrease stability of imaging with a fixed ω_{RF}. Hence to combat this, magnetic resonances are always taken and the lineshape is fitted to extract the amplitude and account for any change in Ω_L.

3.1.7 AC Sensitivity

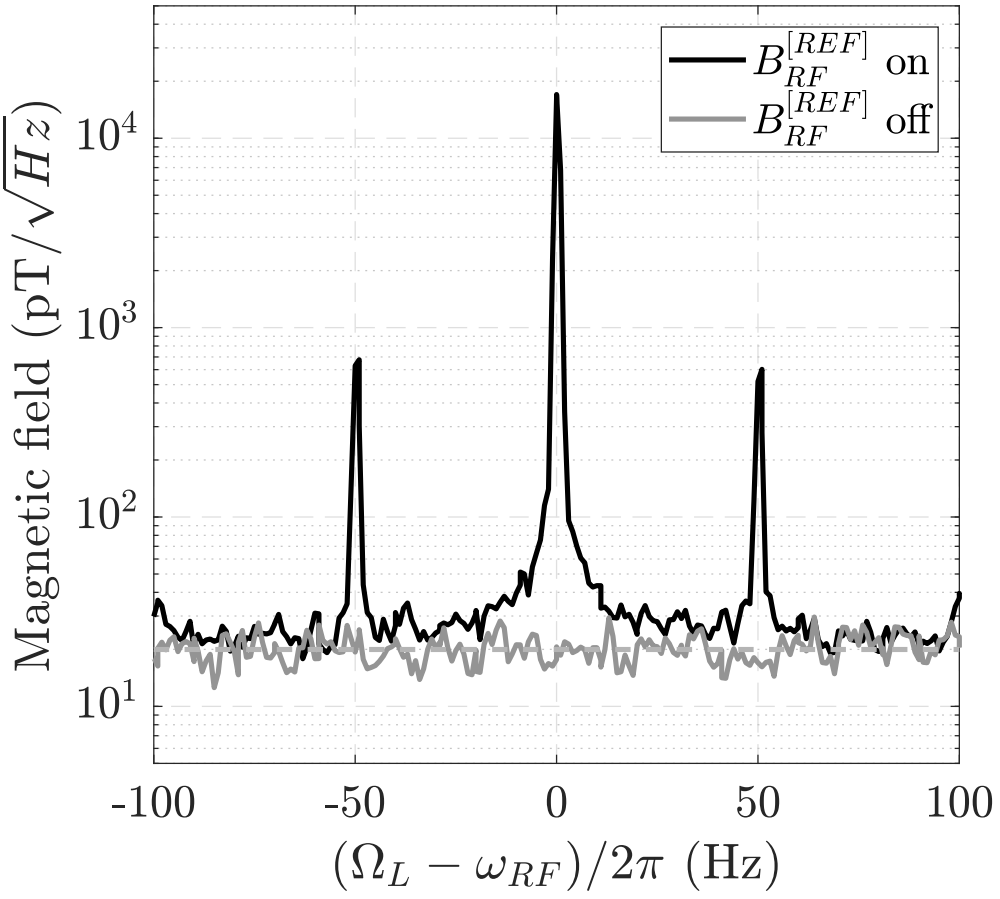

Figure 3.8: Calibrated magnetic field spectral density of the mechanically translatable RF-AM at $\Omega_L/2\pi = 56$ kHz. Spectra were taken with and without the reference field of $B_{RF}^{[REF]} = 17\,\mathrm{nT_{rms}}$. For this measurement the vapour cell was heated to 40 °C. Grey dashed line represents the average of the noise level. Raw data was taken by Cameron Deans. Figure adapted from [5].

Using a calibrated reference field of $B_{RF}^{[REF]} = 17\,\mathrm{nT_{rms}}$ it was then possible to

measure the AC sensitivity. The spectrum in figure 3.8 was obtained from the power spectral density of the polarimeter signal, with the RF-AM on resonance at $\Omega_L/2\pi = 56\,\text{kHz}$ with $B_{RF}^{[REF]}$ on and off to measure the SNR of 915. The graph can then be calibrated to magnetic field spectral density by assigning the main peak height to be equal to $B_{RF}^{[REF]}$. Then using equation 2.37 the AC sensitivity can be calculated to be $dB_{AC} = 19\,\text{pT}/\sqrt{\text{Hz}}$. Sidebands about the main peak in the spectrum reveals the coupling of 50 Hz noise to the magnetometer resonance, which produces harmonics.

3.2 EMI Imaging

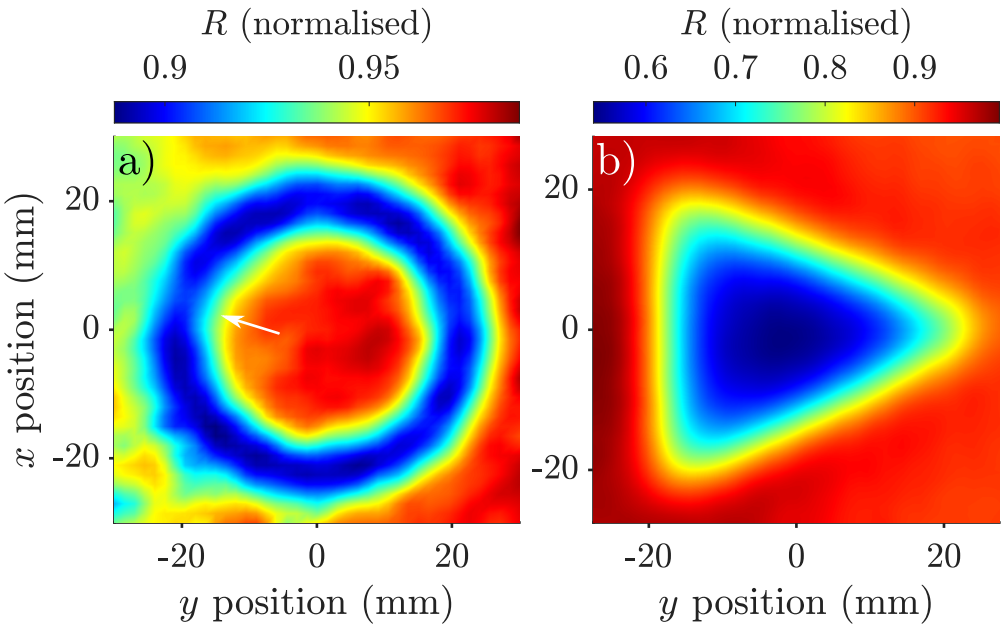

Figure 3.9: R images at $\Omega_L/2\pi = 55\,\text{kHz}$ of a cut Cu ring a) and an Al triangle b). The images are normalised to the maximum value of R recorded. The spatial step of the 2D translational stage was 2 mm in a) and 1.2 mm for b). The images are filtered with a Gaussian filter with standard deviation of 1. The white arrow in a) shows the location of the cut.

For imaging, magnetic resonances are built up at each pixel by sweeping ω_{RF} from $\Omega_L - \Delta_{RF} \rightarrow \Omega_L + \Delta_{RF}$ where typically $\Delta_{RF} = 5\,\text{kHz}$. A dual-phase lock-in amplifier records outputs X and Y. Then the magnitude $R = \sqrt{X^2+Y^2}$ and the phase $\phi = \arctan(Y/X)$ are calculated and the resonant values are extracted for each pixel to then become R and Φ images. R forms the measurement of B_{TOT} while Φ gives

the angle between B_{TOT} and B_1 (see figure 2.1). Figure 3.9 shows the R images of two target objects to demonstrate the ability of the mechanically translatable RF-AM to perform EMI imaging of small conductive objects. Figure 3.9a shows the R image of a Cu ring[9] of 40 mm diameter which had a 0.5 mm slice cut from the ring while 3.9b shows the R image of an Al isosceles triangle of dimensions 48 mm × 49 mm (W×H). In this configuration, where the excitation field (RF coil) has a smaller area in the imaging plane (x-y plane) than the sensor volume (probe-pump intersection), the spatial resolution is set by the RF coil diameter (6 mm) [85][10]. This limitation can be seen in Figure 3.9a as the 0.5 mm slice in the copper gasket, while detected, cannot be fully resolved. The results show the capability of the mechanically translatable RF-AM to produce EMI imaging of stationary conductive targets.

3.3 Through-Skin Pilot-Hole Detection

Now we identify a real-world application of EMI with AMs. In many industrial processes, it is often required that a panel (or skin) is secured to a thick metallic support (or strut). Specifically in the aviation industry, aircraft wing manufacture requires the outer skin to be drilled onto the support strut. The support struts are prefabricated to have pilot-holes ready for the engineer to drill through from the other side of the skin. However, these large scale situations present the challenge of the engineer not being able to see the pilot-hole and thus errors arise from trying to approximate the pilot-hole locations. Due to manufacturing tolerances, an erroneously drilled hole can, in the worst case, make the whole wing become defective and require re-manufacture[11]. Transient thermography, a method of applying rapid yet benign pulses of heat to the sample to measure thermal conductivity has been tested as a possible solution [88]. While the strut can be identified with this technique, the apparatus needs to be in tight thermal contact with the skin and becomes

[9] Copper CF40 gasket for ultra-high vacuum flanges.

[10] This is in the situation of negligible lift-off where the sample is very close to the RF coil. With significant lift-off, the divergence of the primary field will lead to a loss in spatial resolution due to decreased localisation of the primary field in the sample [86].

[11] From Halosensor.com, a company producing technology based on the permanent magnet solution in [87].

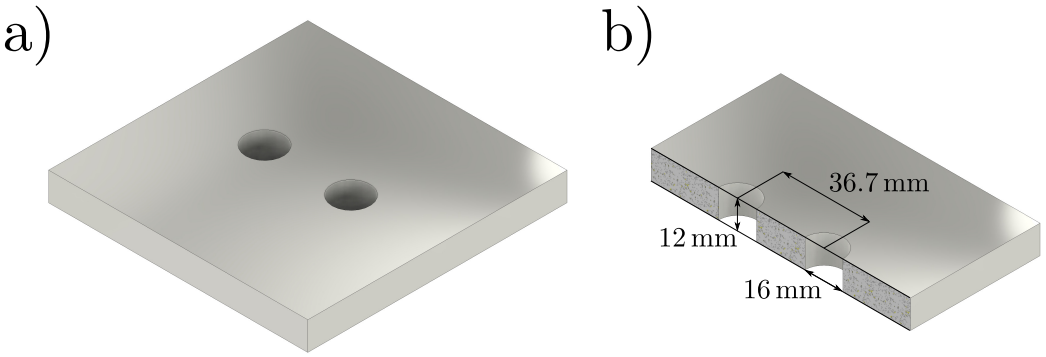

Figure 3.10: CAD drawing a) with cross-sectional view b) of the double-hole Al target to show the dimensions of the pilot-holes.

almost completely ineffective when an air-gap of $>10\,\mu$m is introduced. This creates issues when translating the measurement device across the skin surface and/or if embossed/indented features are present on the skin. It also prevents measurements of skin-strut systems that have any insulation layers. Another method, commonly deployed at present, is to detect the field of a very strong permanent magnet[12] that is placed within the pilot-hole [87]. This requires access to the other side of the skin and normally requires someone to climb inside the wing to place/remove the magnet. EMI with AMs has the potential to circumvent these issues by providing a contactless, non-destructive imaging system that does not rely on access to the other side of the skin. Additionally, the mechanically translatable RF-AM presented in this chapter allows for a through-skin pilot-hole detection proof-of-principle, in near real-world conditions where the object is immovable and the magnetometer is unshielded from ambient magnetic fields. Figure 3.10 shows CAD models of the test target for the pilot-hole imaging: two 16 mm diameter holes are drilled into a $108 \times 110 \times 12\,\text{mm}^3$ $(W \times L \times H)$ Al block[13]. Initially this double-hole target was imaged with only the target holder (0.1 mm of plastic) between the target and the sensor head. Figures 3.11a and 3.11b show the R and Φ images of the double-hole target at $\Omega_L/2\pi = 6.5\,\text{kHz}$ respectively. The range of the image is cropped to exclude the boundaries of the target and isolates just the pilot-holes, to reveal

[12] Very strong permanent magnets also create a hazard to operators.

[13] Al is chosen to mimic the situation in aviation, whereby aluminium alloys are the material of choice for wing parts [89].

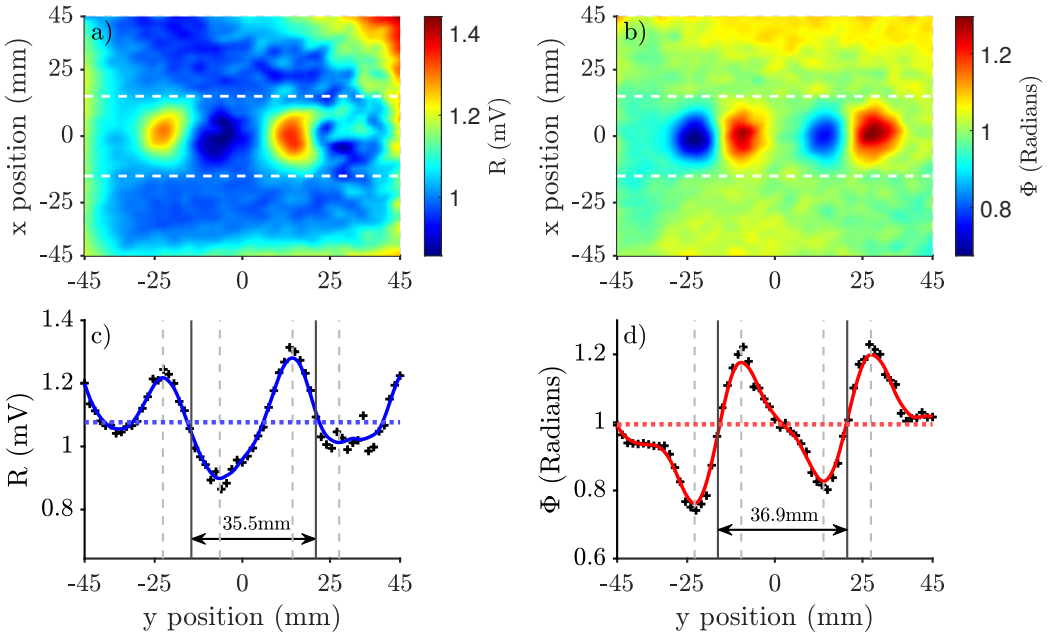

Figure 3.11: R image a) and ϕ image b) of the double-hole Al target along with corresponding horizontal interpolations c) and d) taken at $\Omega_L/2\pi = 6.5\,\text{kHz}$. The white dashed lines in a) and b) show the bounds of the interpolation. The vertical grey dashed lines in c) and d) show the positions of the peaks and troughs detected by the peak detection algorithm with the vertical black line showing the calculated hole centre from the midpoint. The double arrow then shows the measured pilot-hole separation. Horizontal blue and red dotted lines show the average R and Φ across the rest of the image to give a baseline. Figure adapted from [6].

two features in the centre of the image. The images are interpolated within the range of the white dashed lines and the resultant plots are shown in figures 3.11c and 3.11d. The interpolations allow us to identify the characteristic pattern of the pilot-holes and to calculate their separation. A dispersive-like shape can be seen in both the R and Φ interpolations as the target is scanned in the y axis. This can be explained as B_{RF} reflecting off the edge of the pilot-hole at an angle due to the boundary which changes the angle of B_{TOT} and creates a measurable change in the measured field. Since the pumping direction, the x-axis, is a dead-zone for the magnetometer, the pattern is not radially symmetric about the pilot-hole. However if the magnetometer is orientated such that the pumping direction is perpendicular to the hole, the pattern becomes radially symmetric [90]. To find the centre of

the pilot-hole, a peak detection algorithm in MATLAB[14] was used to find the position of the peak and trough of each dispersive shape. Then by taking the midpoint of the peak and trough, the centre of the pilot-hole could be established and from here the separation could be extracted and compared to the true value of 36.7 mm. To image the pilot-holes through a skin, we now consider the skin-depth δ. For

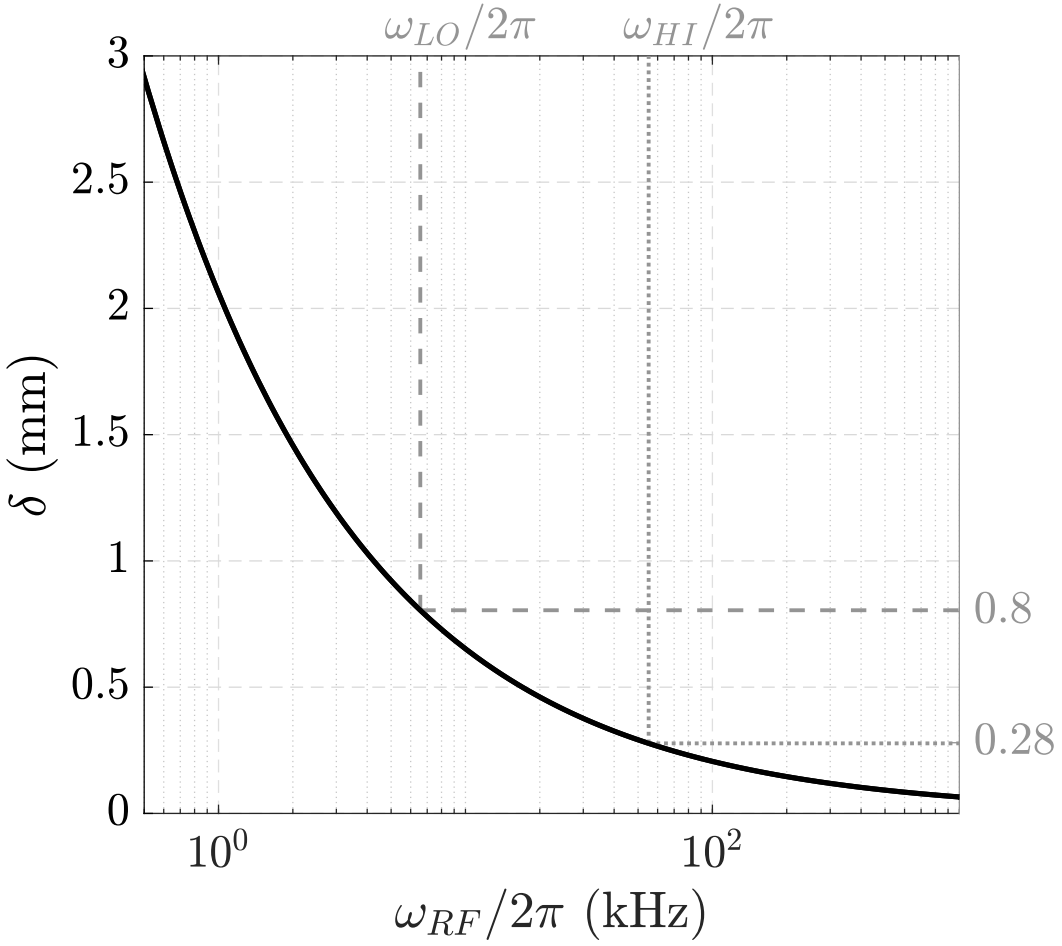

Figure 3.12: Calculated skin-depth δ of Al as a function of ω_{RF} using equation 2.2. The grey lines show the skin-depth at the frequencies used in the dual-frequency technique.

through-skin imaging, it is helpful to use a dual-frequency approach [91], whereby an image at a lower-frequency RF field ω_{LO} which penetrates the skin shows the structure of the skin and below the skin, and an image using a higher-frequency RF ω_{HI} gives the structure of just the skin. The two images can then be subtracted to

[14] MATLAB *findpeaks* algorithm

leave an image that reveals the stucture below the skin only. Figure 3.12 shows the calculated skin-depth for Al as a function of ω_{RF}. For the RF-AM, the minimum resonant frequency that gave a stable resonance was $\Omega_L^{[min]}/2\pi = \omega_{LO} = 6.5\,\text{kHz}$ which gives a skin-depth of $\delta_{LO} = 0.8\,\text{mm}$. $\omega_{HI} = 55\,\text{kHz}$ was then chosen, giving a skin-depth of $\delta_{HI} = 0.28\,\text{mm}$. To shield the pilot-holes, an Al skin of dimensions

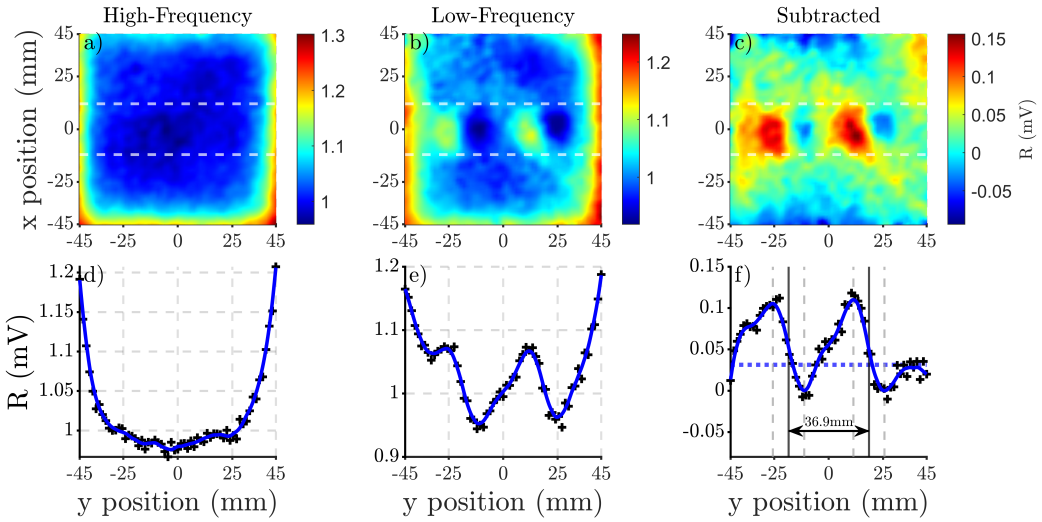

Figure 3.13: *R* images at ω_{HI} a) ω_{LO} b) and the dual-frequency subtracted image c) of the double-holeAl target through the 0.41 mm skin, along with their respective horizontal interpolations in d), e) and f). White dashed lines show the bounds of the horizontal interpolation. The images are filtered with a Gaussian filter with standard deviation of 1. The separation distance in f) is found with the same technique as for figure 3.11d. Figure appears in [6].

$108 \times 110 \times 0.41\,\text{mm}^3$ $(W \times L \times H)$ is placed between the target and the sensor head, as shown in figure 3.1. The thickness of the skin is comparable to the difference in skin depths of the dual-frequency approach $\delta_{LO} - \delta_{HI} = 0.48\,\text{mm}$. Figure 3.13 shows the results of the dual-frequency subtraction technique on the double-hole Al target, shielded by the Al skin. In the case of ω_{HI} we see the boundaries of the skin appearing as decreased absorption of the RF towards the edges of the image. This can also be seen in the ω_{LO} image, along with the hole structure observed in the unshielded case in figure 3.11. After subtraction, the effect of the skin is removed, leaving only the pilot-hole pattern, which allows for the localisation of the pilot-hole centres. The peak detection algorithm outputted the pilot-hole sepa-

ration to be $36.9 \pm 0.4\,\text{mm}$[15] which agrees with the real separation value to within 1 standard deviation.

3.4 Imaging Corrosion Under Insulation

We now turn to another real-world application of EMI, the case of examining corrosion in piping. Corrosion under insulation is a problem in chemical and petroleum industries in which insulated piping can succumb to damage via corrosion and fail [92]. Lack of access to the pipe due to the insulation limits the capability of inspection. EMI with RF-AMs can provide a solution without the need for the insulation to be removed and again as pipelines are generally immovable objects, the mechanical translatable RF-AM presents a step towards real-world use. To simulate corrosion, multiple recesses are milled into a block of Al [3] with dimensions $110 \times 70 \times 12\,\text{mm}^3$ $(W \times L \times H)$. This can be seen in figure 3.14 as four slots with incrementally deeper recesses up to full depth (to compare to a hole). Figure 3.15

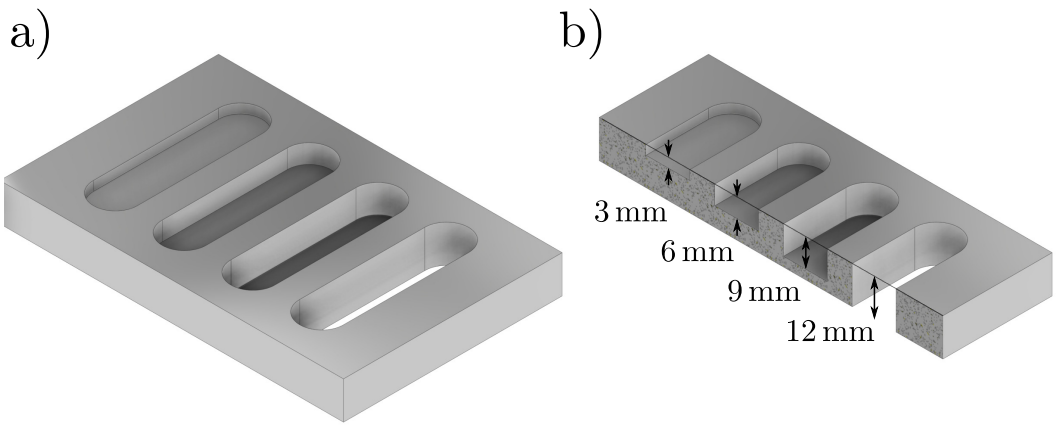

Figure 3.14: CAD drawing (a) with cross-sectional view (b) of the multi-recess Al target to show the dimensions of the corrosion slots.

shows the EMI imaging of the recess plate with a 1.5 mm layer of rubber between sensor head and target. Here the recesses face the sensor head. From the R image, we see decreased absorption of the RF field as the recess level deepens which we can attribute to the reduced amount of material. In the Φ image at each recess we

[15] Uncertainty was taken as the standard deviation of 10 measurements of the separation from 10 different dual-frequency images.

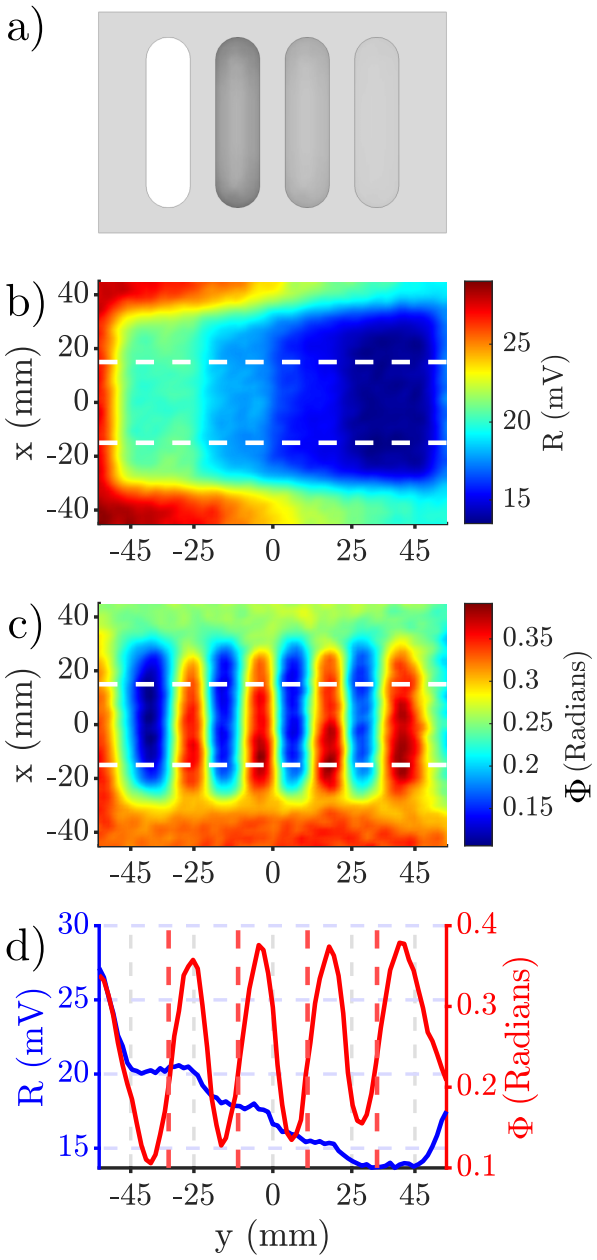

Figure 3.15: EMI imaging of multi-recess plate under 1.5 mm of rubber insulation at $\Omega_L = 55$ kHz. CAD drawing a) of the multi-recess plate is given to show the orientation for the R image b) and Φ image c) with their horizontal interpolations shown in d). White dashed lines show the bounds of the horizontal interpolation. The images in b) and c) are filtered with a Gaussian filter with standard deviation of 1. Red dashed lines in d) show the calculated positions of the recesses.

see again the dispersive pattern demonstrated by the double-hole block in figure 3.11. This allows identification and localisation of the centre of the recess slot in the same method as for the double-hole block. The R value can then be taken for

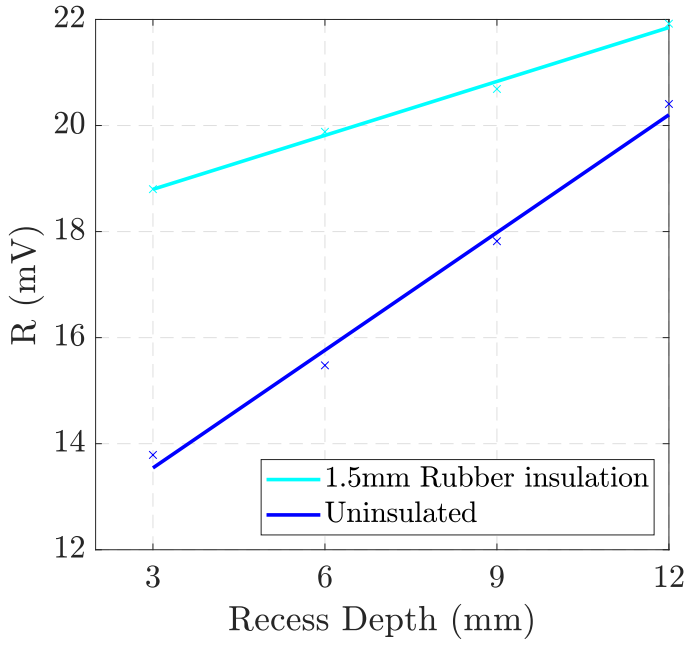

Figure 3.16: *R* versus recess depth for the uninsulated (blue) and 1.5 mm insulated multi-recess plate. Crosses represent the extracted data and lines show linear fits to the data.

at each slot centre and plotted against recess depth. This can be seen in figure 3.16 where the *R* value at each recess slot centre is plotted against the recess depths. A linear curve is fitted to the data, showing the proportionality of *R* to recess depth and demonstrating the efficacy of the technique for both insulated and uninsulated measurements. The difference in absolute *R* between the uninsulated and insulated measurements can be attributed to the effective lift-off that the 1.5 mm rubber layer introduces between the RF coil and the multi-recess plate, decreasing the induction caused by the primary field.

3.5 Discussion

The results show excellent promise for the development of RF-AMs into fully portable devices that can be used in real-world settings. The mechanically-translatable RF-AM demonstrates the ability to raster the sensor around an unshielded environment whilst imaging an immovable target. Accurate shape imaging was shown in figure 2.1 opening up the prospect of object detection. A direct application to the aerospace sector was investigated, presenting the ability to aid wing

manufacture by accurately detecting and localising pilot-holes covered by an Al skin without the need for permanent magnets or access to the other side of the skin. The use of a 2×2 array, as developed in [93], could allow access for a central drilling hole to be added to the sensor head and allow an operator to insert the drill when aligned over the pilot-hole. In section 3.1.6, imperfect bias field stabilisation was found to be the limiting factor of the mechanically translatable RF-AM. Optimising the stabilisation system will allow for more stable resonances at lower frequencies. A stable resonance would speed up measurements by only requiring a single measurement at ω_{RF} for each pixel, instead of building up a magnetic resonance at each pixel like in figure 3.2 and extracting the amplitude from the fit. More stable resonances at lower frequencies would also allow for lower ω_{LO} in dual-frequency images, which as can be seen from figure 3.12, would unlock exponentially deeper penetration and greater skin thicknesses. Finally, a direct application to the oil & gas industry is explored in the investigation of corrosion under insulation. Insulated recesses of various depths were identified and measured, with a linear response outputted by the technique.

Chapter 4

Towards a Cs Cold-Atom Magnetometer

This chapter presents progress towards a new setup for cold-atom magnetometry based on a ^{133}Cs BEC. While a ^{87}Rb BEC had been produced via a hybrid trap in the lab previously, ^{133}Cs requires different cooling mechanisms to reach BEC due to its collisional properties forbidding efficient evaporative cooling in a magnetic trap. So here I explored the use of 3D Raman sideband cooling (dRSC) to cool the atoms into a dipole trap for optical evaporation. The project started from repairs/upgrades to a vacuum chamber used for a previous ^{133}Cs experiment and progressed to dRSC before beginning the dipole trapping stage. The project was eventually interrupted at this stage due to difficulties introduced by the COVID-19 pandemic.

4.1 Setup

4.1.1 Pre-existing Setup

The project started from a setup previously used to obtain a Cs MOT in the laser cooling lab with the aim of using this setup for a Cs optical lattice. Prior to the beginning of the project, the chamber had severe technical issues resulting in the inability to maintain a pressure low enough for an optical lattice experiment to be achievable. As troubleshooting was performed throughout the start of the project, several leaks were discovered along with serious contamination of the chamber which led ultimately to the chamber being dismantled, cleaned and redesigned.

A homemade laser system was also in place to provide light for the MOT, along with an optical setup that could provide light to the LVIS MOT (low-velocity intense source). The homemade lasers were replaced by commercial lasers a few months into the project and hence the whole optical system was redesigned to accommodate for this change. The optical system for the LVIS MOT was eventually upgraded and optics for the science MOT, optical lattice and absorption imaging were designed and added.

4.1.2 Vacuum Chamber

The vacuum chamber is a necessity for working with cold atoms. Low pressures, below 10^{-7} mbar, are required to vastly reduce interatomic collisions which would destroy atom traps. It is vital to remove as many atoms from the chamber that are not in the trappable species, leaving a low pressure of the atoms to be manipulated. The background pressure in the chamber greatly affects the MOT dynamics with a trade-off of loading rate versus lifetime. As the pressure decreases, the reduction in background atomic density leads to fewer untrapped-trapped atomic collisions which leads to loss from the trap, however this also means that the background is more dilute during loading which reduces the loading rate of the MOT. The double MOT setup circumvents this trade-off by using two chambers that are connected by a vacuum impedance allowing for differential pumping. The LVIS chamber, is kept connected to the atomic source, at a pressure of $\sim 5 \times 10^{-8}$ mbar whilst the

second chamber, the science chamber, is kept at much lower pressures $<10^{-9}$ mbar. This allows an LVIS MOT with a high loading rate to form in the LVIS chamber and precool atoms before their transfer to the science chamber where a 3D MOT is formed from the beam of precooled atoms from the LVIS MOT.

4.1.2.1 Chamber Redesign

At the beginning of the project, the vacuum chamber required maintenance and several upgrades in order to be sufficient to provide the environment necessary for the experiment.

Figure 4.1 shows the CAD model of the new design for the chamber. The new design featured a number of improvements over the original. Firstly, the ion pumps were swapped between chambers to allow the more powerful pump (55 $\mathrm{L/s}$ Varian Starcell) to pump the lower chamber and achieve a lower pressure. A getter pump was added (SAES GP100) on the lower chamber to passively pump Cs atoms and improve the lower chamber pressure. The original aluminium middle plate was removed and replaced by more compact fixtures to allow more optical access and manoeuvrability around the glass cell. Finally the caesium ampoule was housed in a cross piece with two window flanges. This allowed visible verification of the ampoule fracture and facilitated the use of a resonant beam to monitor the atomic absorption upon intial release of caesium into the chamber.

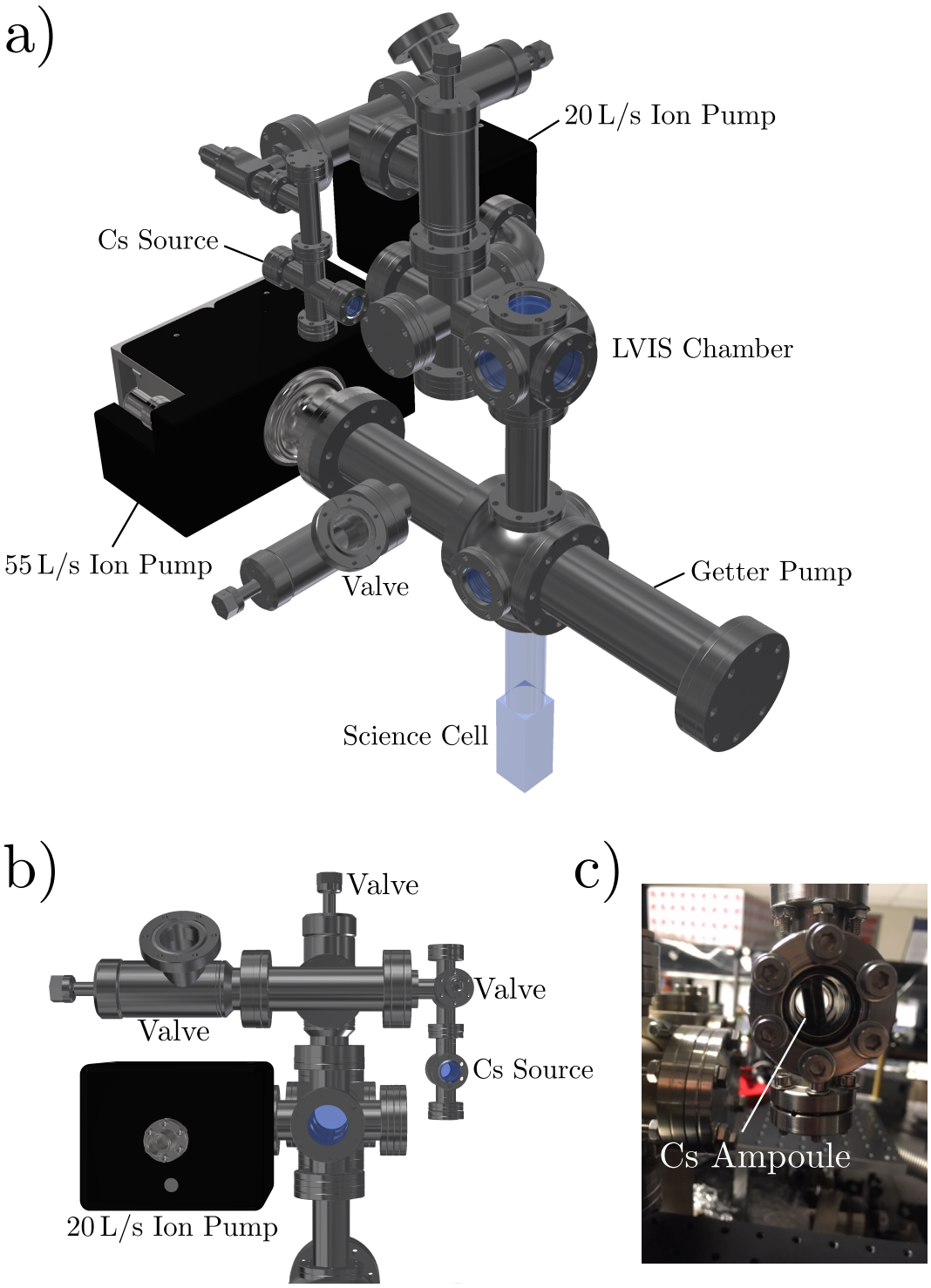

Figure 4.1: CAD model for the new vacuum system a) along with a view from the back of the LVIS chamber b) and a photograph of the Cs ampoule in the source section c).

4.1.2.2 Baking procedure

To achieve ultra high vacuum (UHV) in a vacuum chamber, it is necessary for the chamber to be pumped down and then baked at a high temperature (>150 °C) for several days. While the pumping will remove gases in the chamber, the high temperature is required to promote evaporation and desorption of molecules that are present in the walls of the chamber, that will outgas unless removed and contribute to the pressure in the chamber. The most prominent of these molecules is water, which appears in the chamber after exposure to air. Once the chamber was assembled, the process begins by attaching a turbo molecular pump to the chamber via two metal valves (one for the upper chamber and one for the lower chamber). A scroll pump is connected to the turbo pump to act as a backing pump. This was left to run for 2 hours until the air was fully removed. Then the chamber was heated with heating strips, which were evenly wrapped around the chamber with three layers of aluminium foil to aid the achievement of a uniform heating of the chamber. The temperature was increased by 20 °C/h until a temperature of 200 °C was achieved. This was left for 12 hours. Then the getter was activated, by passing current through its terminals it could be heated to 450 °C for 45 minutes to fully desorb any matter that had adsorbed onto the getter surface. After the getter cooled down, the ion pumps were activated and their pressures were monitored over time. Eventually the pressures recorded by the ion pumps decreased until hitting a minimum value. At this point the system was cooled back to room temperature and the turbo pump was valved off. The final pressures recorded by the ion pumps were 3×10^{-9} mbar in the LVIS chamber and 2.6×10^{-10} mbar in the science chamber.

4.1.3 Double MOT setup

As mentioned previously in section 4.1.2 the use of a loading MOT can greatly enhance the loading rate for a MOT in a UHV chamber, while preserving the MOT lifetime. There are several schemes used to achieve a precooled beam of atoms for loading a UHV MOT, including a 2D MOT, 2D+ MOT, the Zeeman slower and the Low Velocity Intense Source (LVIS) MOT [94]. For this experiment the LVIS MOT is used to act as the loading MOT. Figure 4.2 shows an illustration of the

double MOT system with the LVIS above feeding the atomic beam into the science MOT below. The LVIS MOT is fundamentally a 3D MOT with a 1 mm diameter hole in the centre of the retroreflection mirror in the z axis [95]. This retroreflection mirror is contained in the vacuum system and acts as the vacuum impedance used to connect the two sections of the chamber and allow differential pumping between them. The hole in the mirror cuts a hole in the cooling light reflected back to the MOT which creates a radiation-pressure imbalance in the column directly above the hole. This imbalance pushes atoms through the vacuum impedance to form a transversely cold atomic beam which escapes the LVIS MOT chamber and enters the science chamber to load the science MOT.

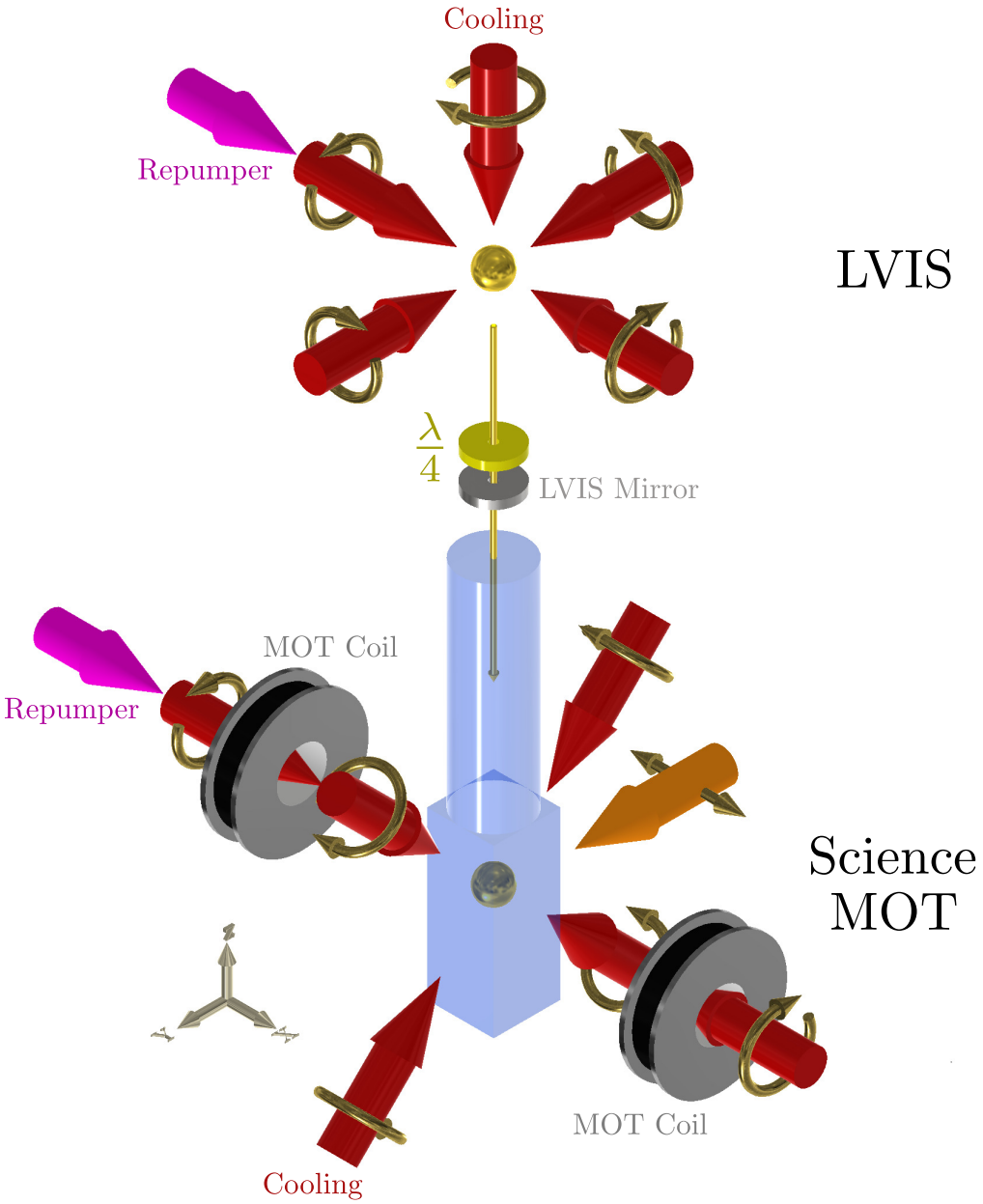

Figure 4.2: Illustration of the LVIS MOT and science MOT used in the Cs experiment. Red, magenta and orange arrows show the cooling, repumper and imaging beams with the copper arrows showing the polarisation of each beam. Gold spheres represent the atomic clouds with the gold arrow illustrating the atomic beam propagating through the vacuum impedance. The science MOT coils are exploded along the x axis to ease the view of the beams and the LVIS MOT coils are not included. Gravity points in the -z direction.

4.1.4 Laser Setup

The next few sections show how the beams for the experiment are generated and delivered to the chambers. We begin by showing the beams on a ^{133}Cs D_2 level diagram in figure 4.3 to summarise the frequencies of the near-resonant beams required for the experiment.

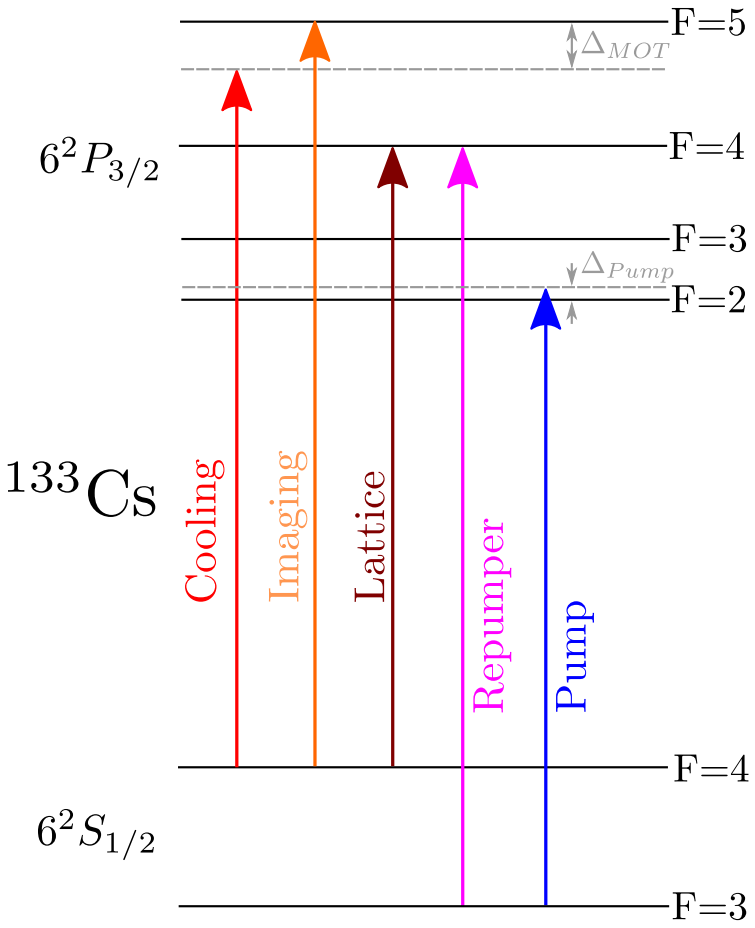

Figure 4.3: Level diagram of the Cs D_2 line [96] showing the tuning of each beam with respect to the hyperfine transitions.

The near-resonant beams are provided by two lasers, named the *cooling laser* and the *repumper laser* which provide the MOT cooling, LVIS cooling, imaging, lattice, repumper and Raman pump beams respectively. The cooling laser is locked to the $|F = 4\rangle \rightarrow |F' = 4/5\rangle$ cross-over resonance while the repumper laser is locked to the $|F = 3\rangle \rightarrow |F' = 3/4\rangle$ cross-over resonance. From there various acousto-optic modulators (AOMs) shift the individual beams to their intended frequency.

4.1.4.1 Cooling Laser Setup

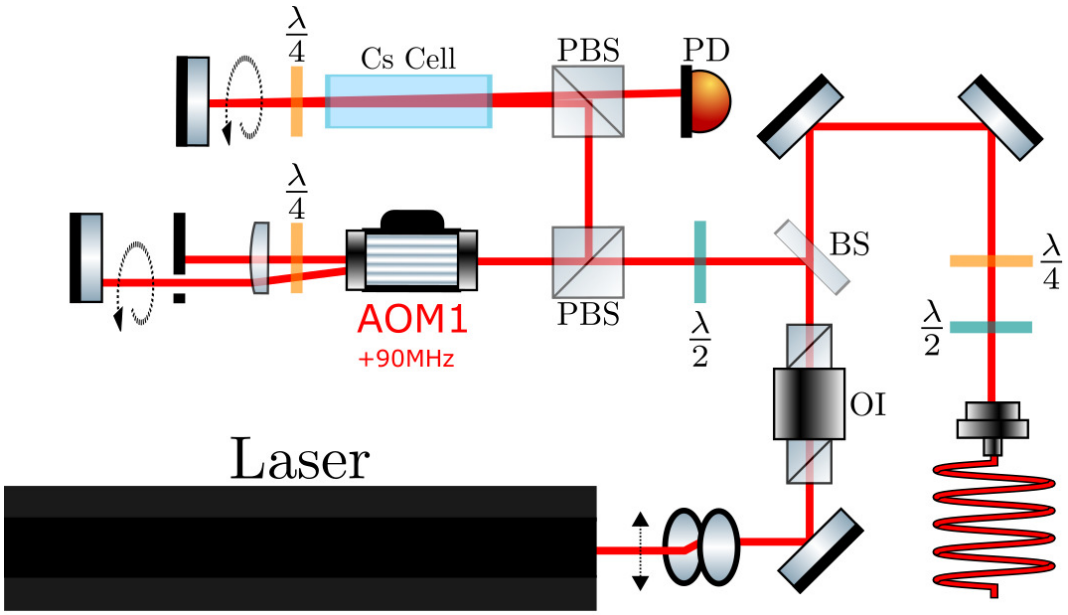

Figure 4.4: Schematic of the optical setup used to prepare the cooling light and deliver it to the MOT table. The black arrows are to signify the polarisation of the beam. *BS* here refers to the beam sampler.

Figure 4.4 shows the optical arrangement for the preparation of the cooling light. The 852nm light is produced by the NarrowDiodeA from Radiant Dyes. This system consists of a lower power (50 mW) external cavity diode laser (ECDL) which feeds into a optical amplifier which can amplify the laser power to levels exceeding 1.4 W. A periscope raises the height of the beam to the level of the optics in the system and directs it through an optical isolator (OI). A beam sampler (BS) directs a fraction of the beam (4%) towards a double pass AOM setup. The -1th order beam emerging from the AOM is reflected back through the AOM via a mirror. This will detune this light by a frequency f_{AOM1} on each pass to ultimately red detune the light by $\Delta_{AOM1} = 2f_{AOM1}$.

This light then passes into a saturated absorption spectroscopy (SAS) setup, where the beam passes through caesium vapour confined in a glass cell at low pressure (10^{-7}mbar). The hyperfine transitions of the $|F = 4\rangle \rightarrow |F'\rangle$ manifold can be resolved by sweeping the laser frequency. The laser current is modulated at 150 kHz to produce a modulation in laser frequency, a lock-in amplifier extracts this modu-

lation from the photodiode signal and generates an error signal based on the phase response of the hyperfine transition to the modulation. This allows for the generation of an error signal and allows the laser to be frequency locked to a specific hyperfine transition. Since the double pass AOM red detunes the light entering the SAS setup by $2f_{AOM1}$, when the laser is locked to a transition it is effectively blue detuned from that transition by $2f_{AOM1}$. This offers the advantage of being able to arbitrarily detune the laser at different stages of the experiment.

The majority of the laser light is transmitted through the beam sampler, where it is then coupled to a polarisation maintaining fibre (THORLABS P3-780PM-FC-10) which then carries the light to the MOT table.

4.1.4.2 Repumper Laser Setup

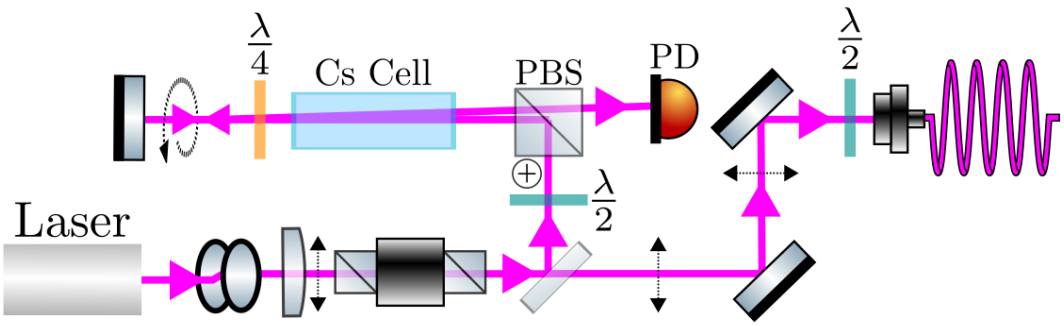

Figure 4.5: Schematic of the optical setup used to prepare the repumper light and deliver it to the MOT table

The diagram in figure 4.5 shows the optical arrangement that is used to prepare the repumper light for delivery to the MOT table. The laser is a MOGLABS ECDL with a maximum output power of 110mW. After a periscope to elevate the laser to the height of the other optics, the laser beam passes through a lens ($f = 1000\,\text{mm}$) to aid collimation of the beam. Then this passes through an optical isolator to prevent any light reflecting back into the laser cavity, which would create optical interference and potential damage to the laser. After the optical isolator, a small fraction of the beam is split via a beam sampler, to pass into a saturated absorption spectroscopy setup. The large majority of the light transmits through the beam sampler and is directed into a PM fibre, which carries the light to the MOT table.

4.1.4.3 MOT Table Optics

Figure 4.6 shows an optical diagram of the setup used to split the cooling light and prepare it for use in the MOT and LVIS MOT. Once the cooling and repumper light emerge from the PM fibres on the MOT table, they are split into the beams needed for the MOT and LVIS MOT: MOT cooling (red), LVIS cooling (dotted red), repumper (purple) and imaging (orange). A fraction of both the repumper and cooling light are separated via PBSs to form the light needed for the depump beam (maroon) and Raman pump beam (blue) for dRSC. The repumper, MOT cooling and LVIS cooling beams pass through three different AOMs. This allows independent power control over these three beams during an experimental sequence.

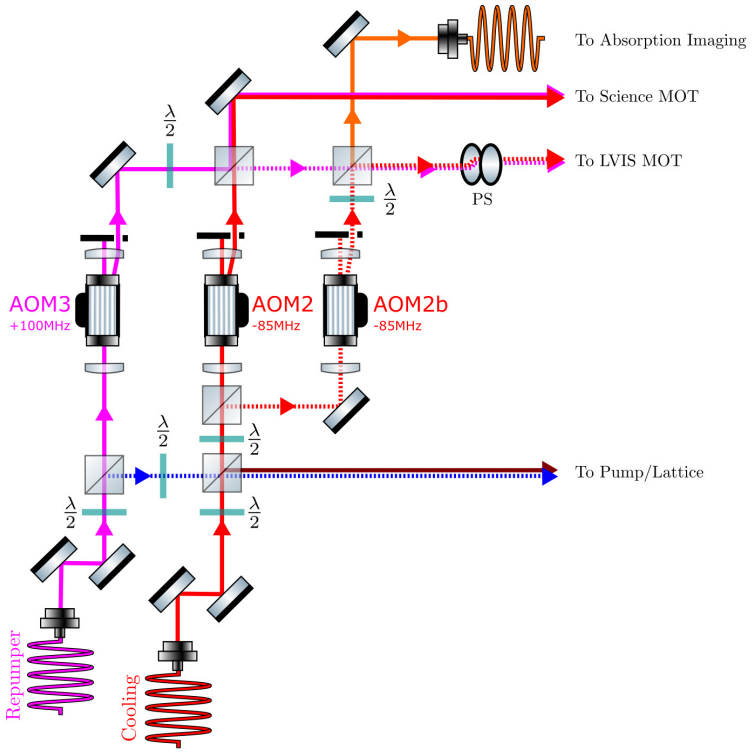

Figure 4.6: Schematic of the optical setup on the MOT table. Beams emerge from the fibre outputs and are then split and passed through AOMs to make the frequencies needs for MOT cooling, repumper and imaging. The beam splitters are all PBSs and the arrangement marked *PS* shows a periscope up to the plane of the LVIS MOT optics.

4.1.4.4 LVIS MOT

Figure 4.7 shows the schematic of the LVIS optical arrangement around the upper vacuum chamber. The optics are mounted on a breadboard that is elevated to the

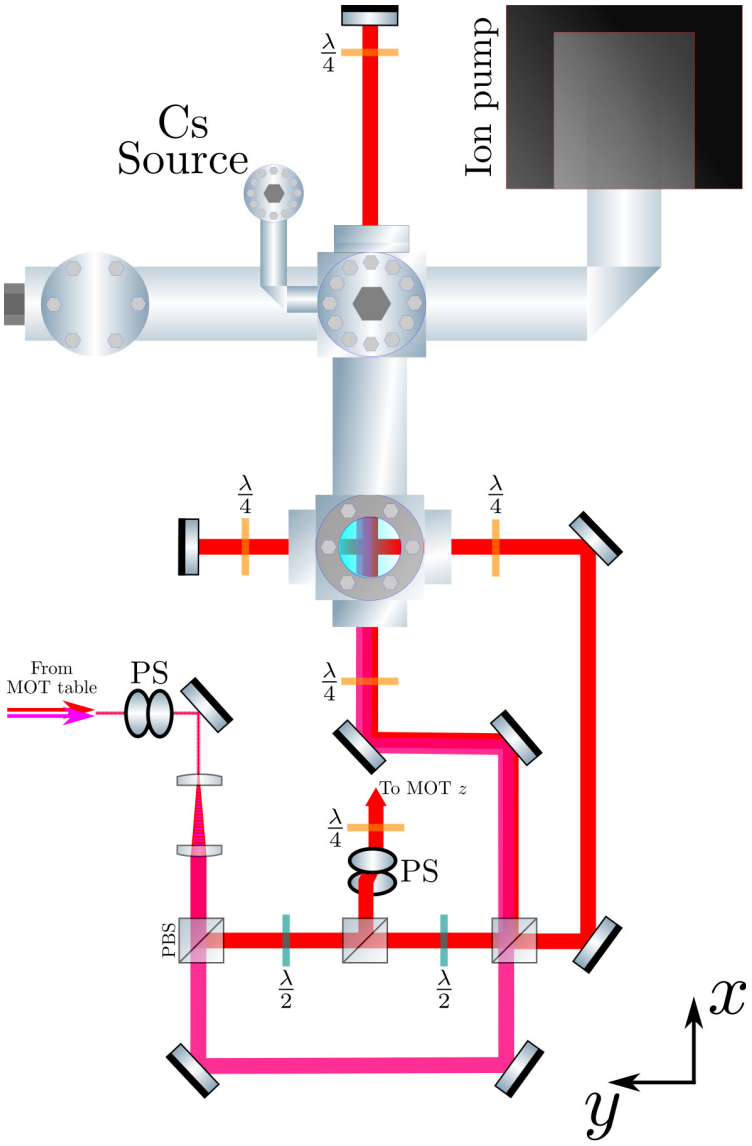

Figure 4.7: Schematic of the LVIS cooling (red) and LVIS repumper (magenta) arrangements around the upper chamber. The z cooling beam is directed down from above via a periscope (*PS*) though not shown in this diagram for simplicity.

height of the LVIS chamber, hence a periscope is required from the MOT table (see figure 4.6) to direct the beam to this level. The LVIS MOT is made with 3 pairs of retroreflected cooling beams. The beams are expanded to 20 mm via a lens system, before being split into beams for individual axes. The beams in x and y pass through the chamber window through their point of intersection at the centre of the anti-Helmholtz field and then exit the chamber through another window. The z beam is lifted above the chamber via a periscope and then directed down into the

top window by a mirror (not shown in diagram). This beam is retroreflected by the mirror housed in the vacuum with the 1 mm hole.

4.1.4.5 Science MOT

The science MOT is generated in the lower chamber, in a cuboidal glass cell with dimensions of $30 \times 30 \times 100\,\mathrm{mm}^3$. The beams are directed from the setup in figure 4.6 towards the cell and are expanded and split into 3 beams via the same method as in figure 4.7. Since the chamber is mounted vertically it is not possible to provide a counter-propagating pair of beams in the z axis, so the orthogonality between the pairs of beams is achieved by directing two of the pairs into the cell at an angles of $\pi/4$ to the x-y plane. Figure 4.8 shows how this is achieved.

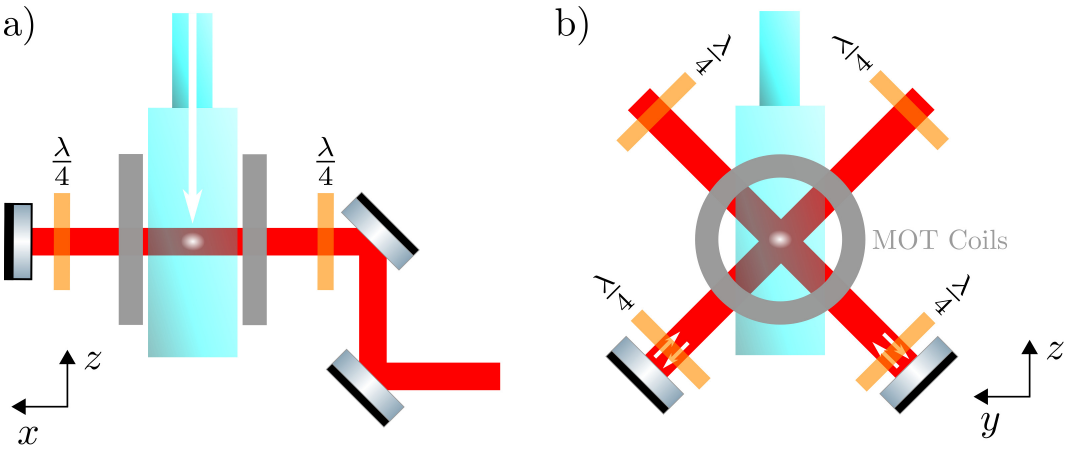

Figure 4.8: Schematic of the MOT cooling beam arrangement in the science MOT in the x-z plane a) and the y-z plane b). The anti-Helmholtz coils which provide the quadrupole field are shown. The white arrow demonstrates the direction of the LVIS beam as it enters the science cell. The white dot in the centre represents the trapped atoms in the chamber

4.1.5 Absorption Imaging

As seen in figure 4.6, the absorption imaging beam is derived from the LVIS cooling beam and coupled to a PM single-mode fibre. The fibre acts to carry the beam to the MOT whilst also providing spatial filtering for the imaging beam, to produce an approximately Gaussian intensity distribution. The atoms are imaged in a conventional resonant absorption imaging sequence whereby the atoms are exposed to a short pulse of weak resonant laser light which is then directed onto a camera

(Guppy F038b). This camera is triggered to capture an image within a few microseconds of the imaging beam turning on, with an exposure time of 20 µs. This image, called the ATOMS image is then compared to an image of the laser light with no atomic interaction, called the LIGHT image. In practice this is taken 200 ms after the ATOMS image is taken, as the atomic cloud is destroyed by the resonant imaging beam leaving no atoms to create absorption in the imaging beam. Finally a third image, called the DARK image is taken with no imaging light, in order to account for background light entering the camera. This image is taken 100 ms after the LIGHT image, with the imaging light turned off by AOM2b. The comparison of the ATOMS image to the LIGHT image allows measurements of atom number and cloud size. Figure 4.2 shows how the imaging beam (orange) propagates in the

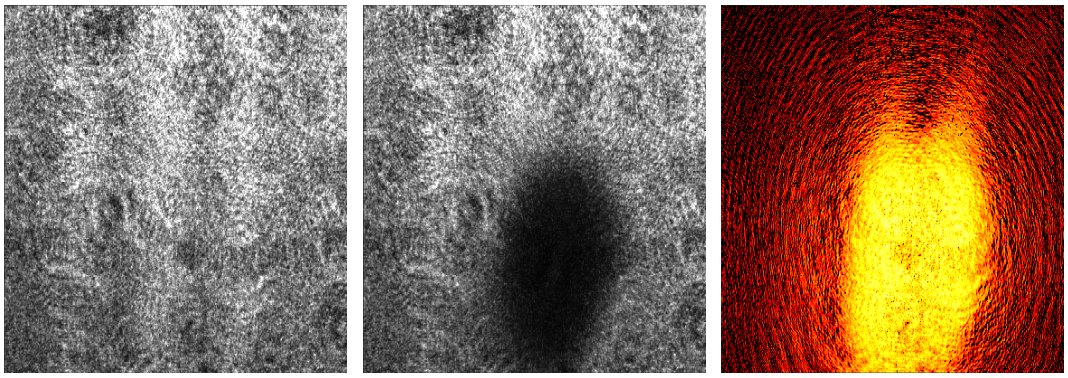

Figure 4.9: Images taken by the absorption imaging camera along with the difference image

y-axis, through the science MOT chamber and ultimately towards the camera. The AOMs in the setup presented in figure 4.6 set the frequency of the imaging light to be on resonance with the $|F = 4\rangle \rightarrow |F = 5\rangle$ cooling transition. With each shot, the RF driver of AOM 2b is shifted by -15 MHz which shifts the frequency of the laser to be on resonance with the $|F = 4\rangle \rightarrow |F' = 5\rangle$ transition, whilst also shifting the angle of the beam to align it to the fibre coupler on the other side of the PBS. The ATOMS image and LIGHT image can be seen in figure 4.9 along with the *OD* image which reveals the atomic distribution. Then the optical density image *OD* of

the MOT can be calculated

$$OD(x,y) = -\ln\left[\frac{ATOMS(x,y) - DARK(x,y)}{LIGHT(x,y) - DARK(x,y)}\right] \tag{4.1}$$

where DARK(x,y) is the dark image taken without the imaging beam on. From this image the *OD* distribution in each axis can be found by averaging through the other axis, for each point along the axis in question. Then a 2D gaussian function can be fitted to the *OD* image to determine the width of the cloud, σ_i, in each axis. The atom number N, is found by summing pixels of the *OD* image

$$N = \frac{A}{\sigma_{sc}} \sum_{x}^{N_x} \sum_{y}^{N_y} OD(x,y), \tag{4.2}$$

where A is the area of a pixel taken from the camera datasheet[1] to be $16.8\,\mu\text{m} \times 19.2\,\mu\text{m}$ and σ_{sc} is the scattering cross section for the $|F=4\rangle \rightarrow |F'=5\rangle$ transition. Since the absorption imaging beam is linearly polarised $\sigma_{sc} = 0.1945\lambda^2 = 1.412 \times 10^{-9}\,\text{cm}^2$ [97].

Atomic temperature was determined by the technique of time-of-flight (TOF). The atoms are released from trapping forces and allowed to freely expand. After a time t_{TOF} the imaging light is switched on and the absorption image is taken. As the imaging light is resonant the process is destructive and hence each shot must be taken with a new sample of atoms. The atoms are fitted to a 2D Gaussian and the widths in the x and z axis $\sigma_{x,z}$, are extracted to infer the positional distribution of the atoms at t_{TOF} after release. As many shots are taken over a time period it is possible to extract the average velocity of expansion by observing the rate of increase of $\sigma_{x,z}$ of the gaussian fits as a function of t_{TOF}

$$\sigma_i^2(t_{TOF}) = \frac{k_B T_i}{m} t_{TOF}^2 + \sigma_i^2(t_{TOF} = 0), \tag{4.3}$$

[1] This was confirmed with the freefall of the atoms, by comparing the measured vertical acceleration with g.

where k_B is the Boltzmann constant and m is the mass of a Cs atom. The temperature along a given dimension, T_i is then determined by fitting a linear function to the width of the atom cloud in that dimension squared, $\sigma_i^2(t_{TOF})$, versus the time-of-flight squared, t_{TOF}^2. The gradient of the linear fit can then be rearranged to find the temperature.

4.1.6 Pump/Lattice setup

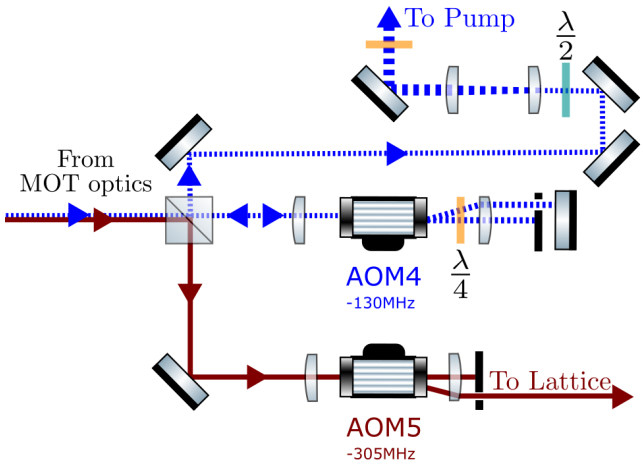

Figure 4.10: Setup used to derive the lattice (maroon) and pump (blue) beams from the cooling and repumper lasers.

For the dRSC phase of the experiment, beams for the optical lattice and a pump beam are required. The pump beam moves atoms to the stretched state of the $F = 3$ ground state. Typically this is a few MHz blue detuned from the $|F = 3\rangle \rightarrow |F' = 2\rangle$ transition and requires a few mW of optical power [98]. The lattice beams need to be red-detuned from the $|F = 3\rangle \rightarrow |F'\rangle$ transition by several GHz to avoid heating the atoms out of the lattice [68]. Using AOM5, the lattice beam can be derived from the cooling light by red-detuning it such that it is on resonance with the $|F = 4\rangle \rightarrow |F' = 4\rangle$ transition. Figure 4.10 shows the setup used to derive the pump and depump beams from the beams passed to the MOT table from the cooling and repumper laser. The pump beam (dotted blue) is passed into a double pass AOM system identical to the one presented in figure 4.4. The lattice beam (maroon) is passed into a single pass AOM. The beams are then combined together via a PBS, expanded with a telescope and then sent to the science MOT. They are then passed into a PBS that splits the main MOT cooling into sub beams for the x-axis, the y'-

axis and the z'-axis. The pump beam is directed along the x-axis so as to be collinear with the bias field.

4.1.7 Dipole Trap Setup

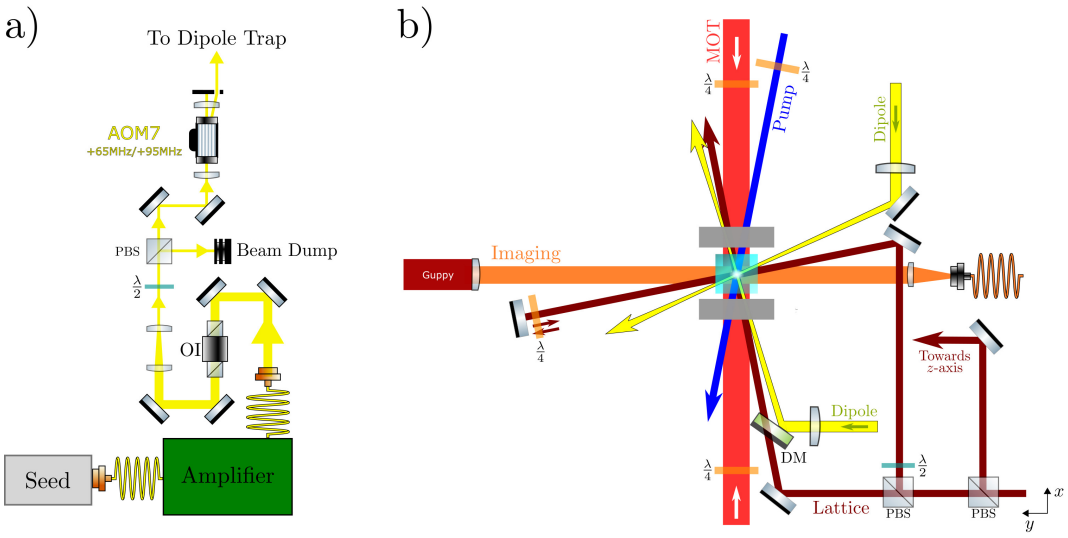

Figure 4.11: Schematics of the dipole trap beam optical setup showing the preparation optics for the high power beam a) and how the dipole beams are injected into the science cell b). Here the acronyms DM and OI refer to the *dichroic mirror* and *optical isolator* respectively.

The dipole trap beam is needed after the dRSC phase of the experiment. For this stage a far off-resonant optical trap (FORT) is superimposed onto the atomic cloud. The use of a FORT significantly reduces the induced heating of the atoms by scattering processes when compared to a near resonant optical trap but requires much higher intensities in order to maintain the trap depth [99]. In previous works, dipole trapping has been performed with FORTs utilising 1064 nm light at intensities of $32\,\mathrm{kW/cm^2}$ [69]. To create such high optical intensities at this wavelength, it is conventional to start with a high optical power ($\sim$10 W) and to focus the beam to have a tight waist ($\sim$100 µm) at the point of intersection with the atoms. Figure 4.11a shows the optics used to prepare the lattice beam. A single-frequency 1064 nm seed laser (INNOLIGHT Metphisto S) is fibre coupled to an optical amplifier (Nufern NUA-1064-PV-0050-D0). The seed couples 80 mW of light into the amplifier, which then amplifies the light to a maximum power output of 40 W. The output is fibre coupled to a fibre output coupler on the optical bench. The beam is

then steered into an optical isolator to prevent back reflection destroying the amplifier. After this the beam is passed through a telescope to reduce its diameter from 5 mm to 1.5 mm. This allows the beam to easily pass through the AOM aperture. The AOM (ISOMET M1080-T80L) is a high power AOM with a maximum optical power rating of 20 W. The preceding HWP/PBS pair allows the beam power to be reduced below the AOM maximum. Due to high optical powers, thermal effects in the AOM crystal can lead to pointing instability during intensity ramping of the RF driving of the AOM. Hence AOM7 is driven by two RF frequencies in order to combat this effect [100]. Instead of ramping the power of the RF driving frequency, the frequency of the AOM is rapidly shifted by turning the 65 MHz off and the 95 MHz on. This has the effect of redirecting the beam (to a beam dump) without affecting the RF power to the AOM. The dipole trap beam is then directed towards the Science MOT as shown in figure 4.11b. To gain optical access to the atoms, shortpass dichroic mirrors (DM) with cut-off frequency of 950 nm are used to combine the lattice beam into the same path as the MOT beam in the x axis. The lenses used to focus the dipole trap beam have a focal length of $f = 500$ mm. The dipole trap beam is focussed at the position of the atoms. The beam then emerges from the science cell and hits a beam dump.

4.1.8 Upgrade of computer control

The laser amplitudes and magnetic fields are controlled by a 32 channel analog output data acquisition (DAQ) board from National instruments (NI PCIe-6738). This replaced the original 8 analog and 8 digital output DAQ board (NI PCI-6713). The board was replaced due to its inability to support hardware timing on all channels. Hardware timing is critical to precise and repeatable timing of the signals generated by the LabVIEW code used to schedule events in the experimental sequence. Previously, code was written to work with software timing, which suffered inaccuracy on the order of 0.1 ms at each phase of the experiment. In software timing, the LabVIEW code keeps time with the iteration loop of the programme on the computer, which can suffer delays if the computer tries to run other tasks simultaneously. With hardware timing, new LabVIEW code was written to upload an experimental

sequence directly to the FPGA buffer on the DAQ board. The outputted signals are then synchronised to the clock on the DAQ board and are insensitive to timing errors produced by the computer.

4.1.9 Active Magnetic Field Stabilisation

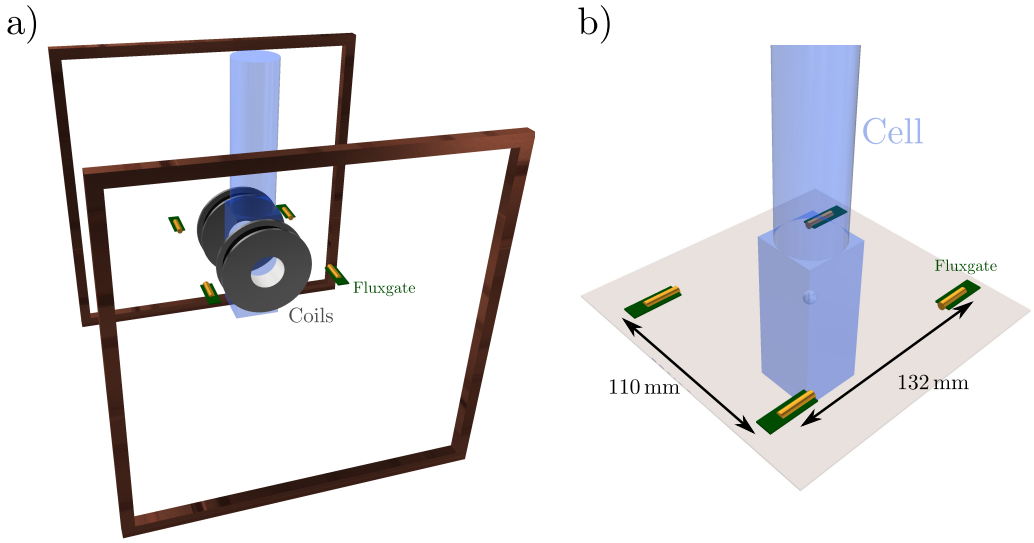

Figure 4.12: 3D drawings of the setup used to stabilise $\mathbf{B}_{Bias}$. a) shows the full setup and b) shows the setup without the circular MOT coil and square bias field coils.

Accurate measurement of the bias magnetic field at the centre of the atomic cloud is an important component of the experiment and moreover, active stabilisation of $\mathbf{B}_{Bias}$ can be critical to prevent dephasing in the magnetometer [32]. Since direct measurement of the magnetic field at the atomic cloud would be invasive to the vacuum chamber, four fluxgate sensors (Stefan-Mayer FLC100) are positioned to sit in the corners of a square lying in the x-z plane, centred on the position of the atoms. Figure 4.12 demonstrates how this looks in the experimental setup. The sensors are aligned parallel (or anti-parallel) with the x axis to measure the field in the $\mathbf{B}_{Bias}$ direction generated by the $310 \times 310\,\mathrm{mm}^2$ square Helmholtz coils separated by 310 mm. In the limit that only linear magnetic field gradients in the measurement axis are significant, $\mathbf{B}_{Bias}$ can be inferred by summing the measurement of each fluxgate sensor $\mathbf{B}_{Flux}$ together [101, 102, 103] such that

$$4\mathbf{B}_{Bias} = \sum \mathbf{B}_{Flux} \tag{4.4}$$

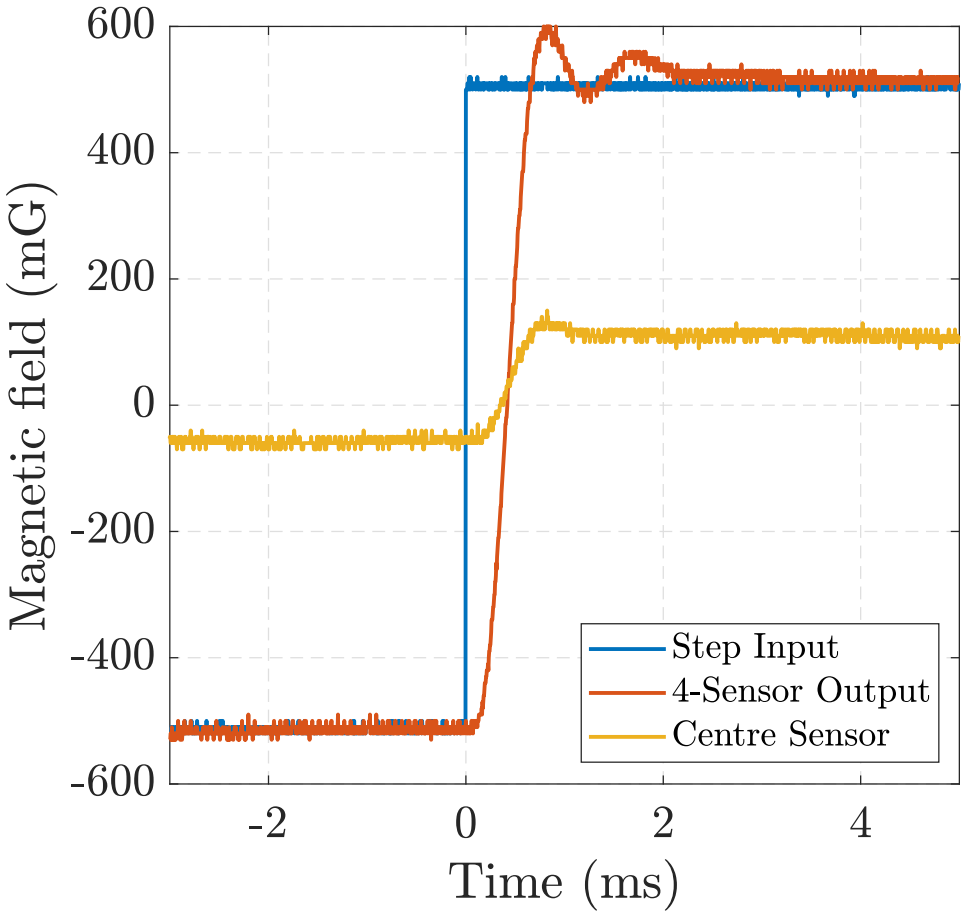

Figure 4.13: Performance of the $\mathbf{B}_{Bias}$ feedback loop with response to a step change in the setpoint of the PID controller.

and therefore the fluxgate signals are added together with an analogue adder circuit before being used as the input for a PID feedback loop, which modulates the bias field Helmholtz coil to stabilise $\mathbf{B}_{Bias}$ to a set value. The validity of equation 4.4 was demonstrated experimentally, by building the stabilisation setup outside the experiment to the same dimensions and then probing the centre of the square with an additional fluxgate sensor. The setpoint of the PID controller was then modulated to tune the PID and measure the performance of the feedback loop. Figure 4.13 shows the response curve observed by both the 4-sensor fluxgate array and the probe fluxgate sensor after a step change in the setpoint of the PID controller. The rise time of $\sim$1 ms is limited by the 1 kHz bandwidth of the fluxgate sensors.

4.2 Cooling Sequence

4.2.1 Experimental Sequence

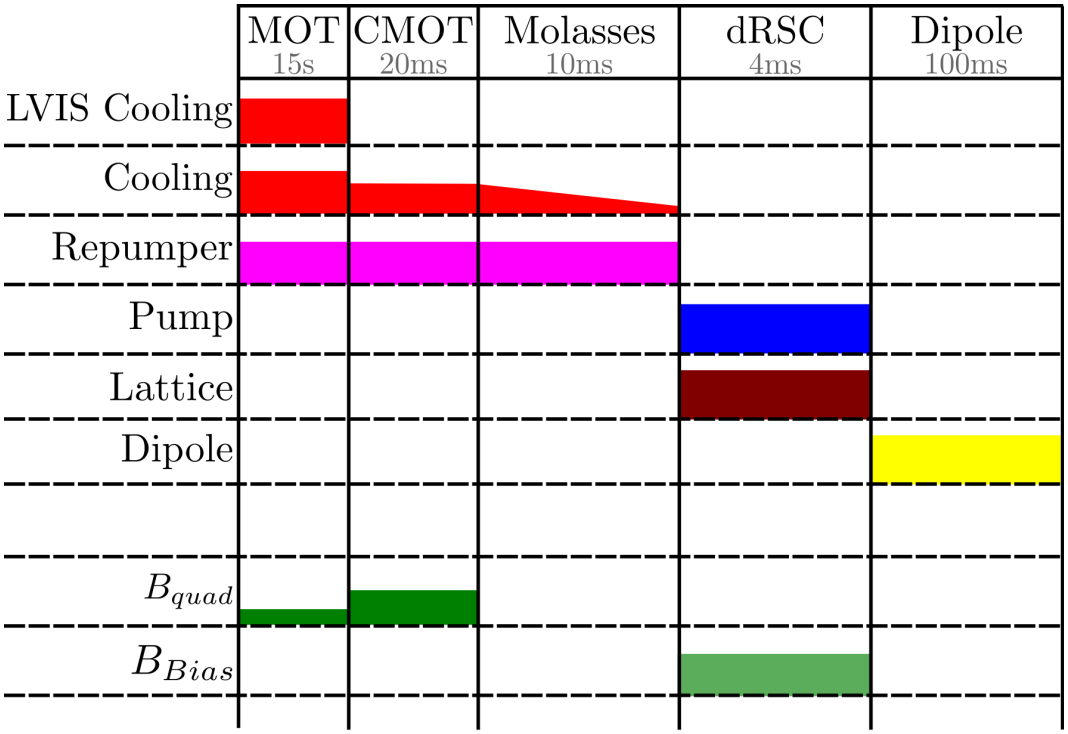

Figure 4.14: Experimental sequence of the Cs cooling cycle. The sequence is broken up into distinct phases with each phase duration indicated in grey underneath. The list is broken into two groups, the upper group (LVIS Cooling, Cooling, Repumper, ...) illustrates the corresponding laser intensity, while the lower group (B_{quad},B_{Bias}) represents the magnitude of the magnetic field.

The phases of cooling and trapping are performed sequentially. This is controlled by LabVIEW software which outputs voltages to the analog output DAQ device from National Instruments (PCIe-6738). Figure 4.14 shows an illustration of the experimental sequence up to the current point of work.

4.2.2 MOT

4.2.2.1 MOT detuning

Once the MOT was established, it was necessary to find the optimal detuning of the cooling beams, which would maximise the number of atoms trapped in the MOT. To perform this measurement the detuning of the LVIS and MOT cooling beams were swept incrementally by changing the frequency of AOM_1 (see figure 4.4). Then the

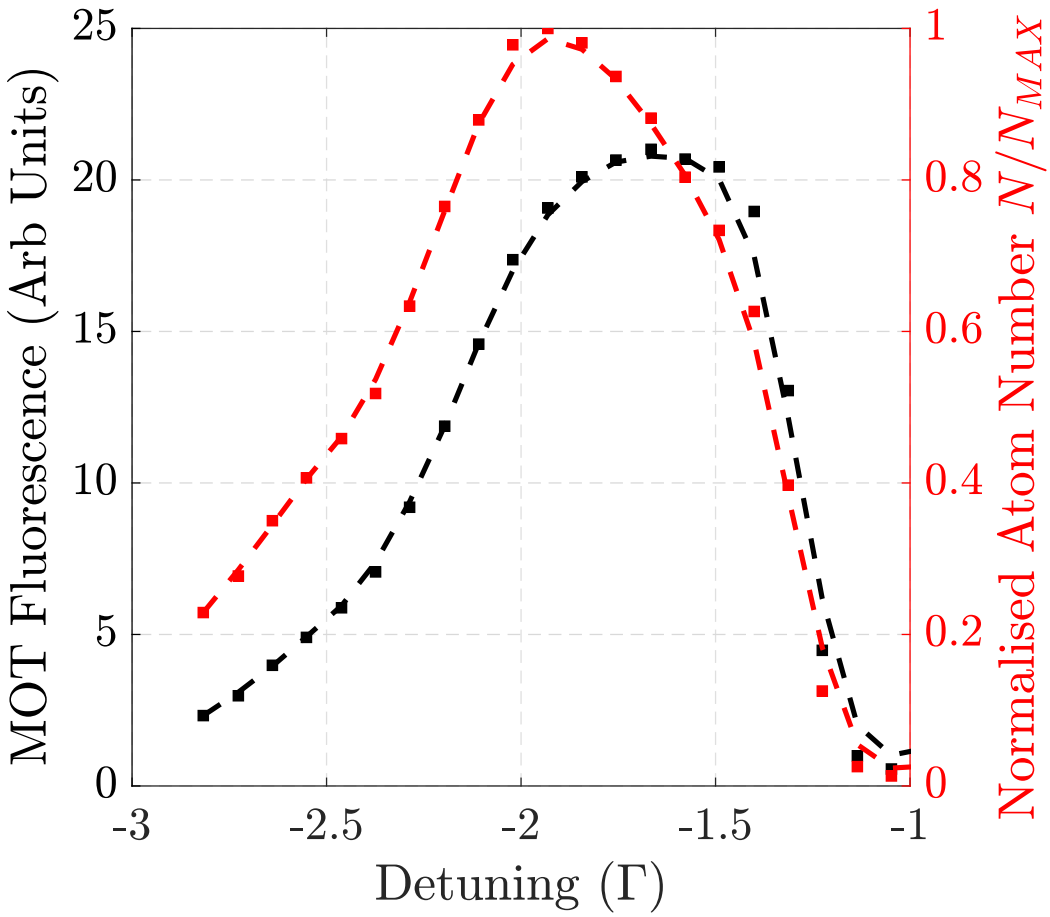

Figure 4.15: MOT fluorescence versus detuning of the MOT and LVIS cooling beams. The error bars are obscured by symbol used. Dashed lines show smoothed averages of the data points.

fluorescence of the MOT was recorded for each detuning. With each iteration, the MOT coils were initially turned off and then back on, and the whole loading curve of the MOT was recorded, until the atoms reached steady state. The maximum value of the fluorescence was then extracted and is plotted against detuning in figure 4.15. The fluorescence captured by the camera F is proportional to the scattering rate of the atoms, R_s and the number of atoms in the MOT N_{MOT}

$$F \propto N_{MOT} R_s; \qquad R_s = \frac{\Gamma}{2}\left(\frac{I/I_{SAT}}{1+I/I_{SAT}+4\left(\frac{\Delta}{\Gamma}\right)^2}\right), \tag{4.5}$$

where I is the intensity of each MOT beam, I_{SAT} is the saturation intensity and Δ is the detuning of the MOT beams from the cooling transition. By calculating R_s for each detuning and computing F/R_s, a calculation of N (with arbitrary units) can be achieved. From this, the maximum N versus Δ can be found and hence optimise the MOT. The atom number is normalised by the number at the maximum N_{MAX} in the results in figure 4.15. It can be seen that N_{MAX} occurs when $\Delta_{MOT} = -1.9\Gamma$ and thus the cooling beams were set to this detuning.

4.2.2.2 MOT temperature

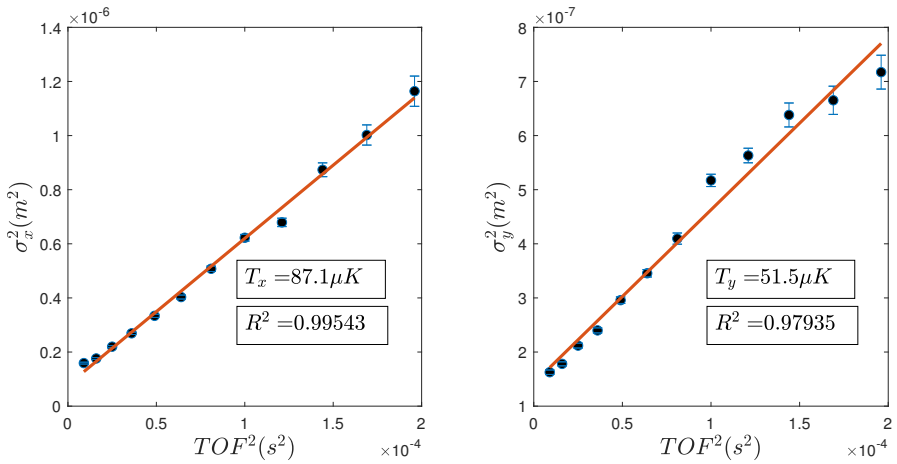

Figure 4.16: The squared width of the atomic cloud in x and y, σ_x^2 and σ_y^2 versus t_{TOF}^2. The red lines indicate the linear fits obtained from the data.

Results of performing TOF on the MOT are shown in figure 4.16. The extracted values of T_x and T_y are of similar value to previous works [104, 105] (70 µK, 20 µK). These temperatures are below the Doppler limit of $T_{Doppler} = 125\,\mu\text{K}$ [96] for the Cs D_2 line. This breach of the limit is facilitated by polarisation gradient cooling at the MOT centre where the magnetic field is zero [71, 106].

4.2.3 Compressed MOT (CMOT)

4.2.3.1 CMOT Gradient

The compressed magneto-optical trap (CMOT) allows for the density of the MOT to be increased without losing atoms. This is achieved by rapidly increasing the magnetic field gradient used to create the MOT. This creates a non-adiabatic compression of the MOT cloud by rapidly decreasing the volume of the trap. Initially

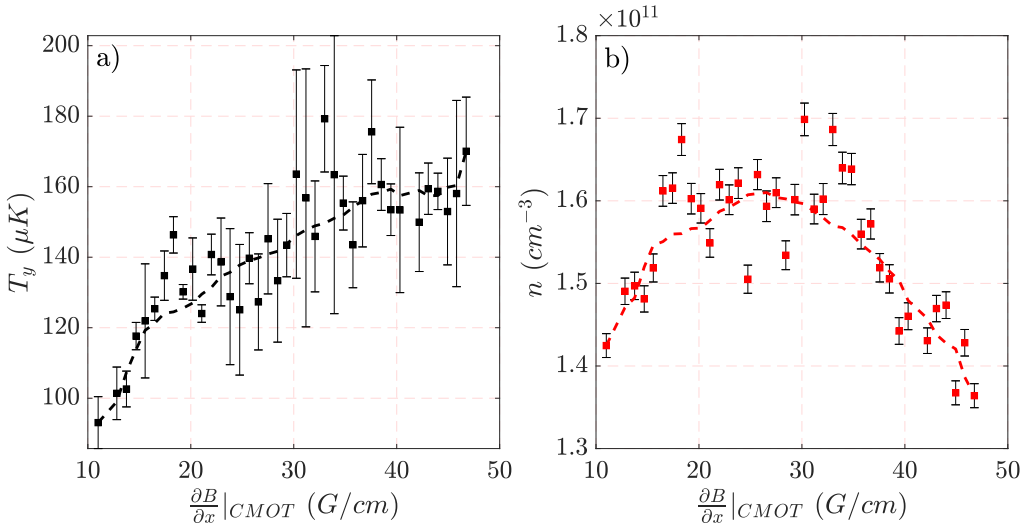

Figure 4.17: Number density n_{CMOT} and temperature T_{CMOT} in the CMOT phase of the experimental sequence. Symbols show the data points while the lines show smoothed averages.

it was necessary to characterise the effect of the rapidly increasing magnetic field gradient for the CMOT and to optimise the height of the step input of current to the MOT coils. The MOT is loaded for 4 seconds at a detuning of $\Delta_{MOT} = -1.9\,\Gamma$ and a field gradient of $\frac{\partial B}{\partial x}|_{MOT} = 20.4\,\mathrm{G/cm}$. Then the CMOT phase is enacted for 20 ms. The anti-Helmholtz field is ramped up in 100 µs to a value of $\frac{\partial B}{\partial x}|_{CMOT}$ which was varied from 20-90 G/cm. The detuning of the cooling light is also further red detuned to $\Delta_{CMOT} = -3.2\,\Gamma$. At the end of the CMOT phase the MOT cooling beams are extinguished leaving the atoms to expand freely. A TOF image is then taken 4 ms later.

The CMOT number density n_{CMOT} increase as $\frac{\partial B}{\partial x}|_{CMOT}$ is increased from $\frac{\partial B}{\partial x}|_{MOT}$ can be seen in figure 4.17. n_{CMOT} increases to a maximum value and then begins to decrease with increased gradient which is consistent with [107]. The value of $\frac{\partial B}{\partial x}|_{CMOT} = 68\,\mathrm{G/cm}$ was chosen as the optimal gradient to maximise the density to $n_{CMOT} = 1.6 \times 10^{11}\,\mathrm{cm}^{-3}$. The temperature of the sample T_{CMOT} can also be seen to rise as the trap is further compressed.

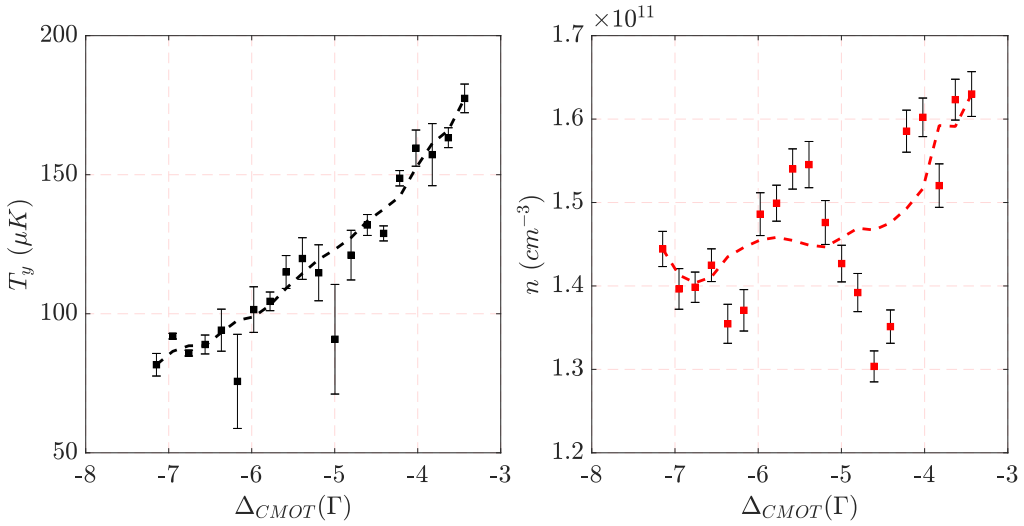

Figure 4.18: Temperature T_{CMOT} and number density n_{CMOT} with increasing red-detuning of the cooling laser in the CMOT phase. Δ_{CMOT} is expressed in units of the spontaneous decay rate from the cooling transition Γ.

4.2.3.2 CMOT detuning

To counteract the temperature rise in the CMOT phase, the detuning of the cooling light Δ_{CMOT} can be adjusted. With $\frac{\partial B}{\partial x}|_{CMOT} = 68\,\mathrm{G/cm}$, the detuning of the cooling light was then swept to determine the optimal value. At the beginning of the CMOT phase the MOT cooling detuning was linearly ramped from Δ_{MOT} to Δ_{CMOT} over the 20 ms duration. The impact of adjustment in the cooling red-detuning can be seen in figure 4.18. At $\Delta_{CMOT} = -7\Gamma$ the beams have counteracted the heating due to the compression and the atoms achieve temperatures that are similar to T_{MOT} whilst preserving the increased density, hence this value is chosen as the detuning for the CMOT phase.

4.2.4 Molasses

4.2.4.1 Molasses Temperature

The molasses stage of the experiment involves sub-Doppler cooling of the atoms via polarisation gradient cooling. This is achieved by rapidly removing the gradient magnetic field (in less than 100 µs), linearly increasing the detuning Δ_{MOL} and lowering the intensity of the cooling beams I_{MOL}, over the molasses phase duration. The temperatures of the molasses are much lower than the temperatures observed

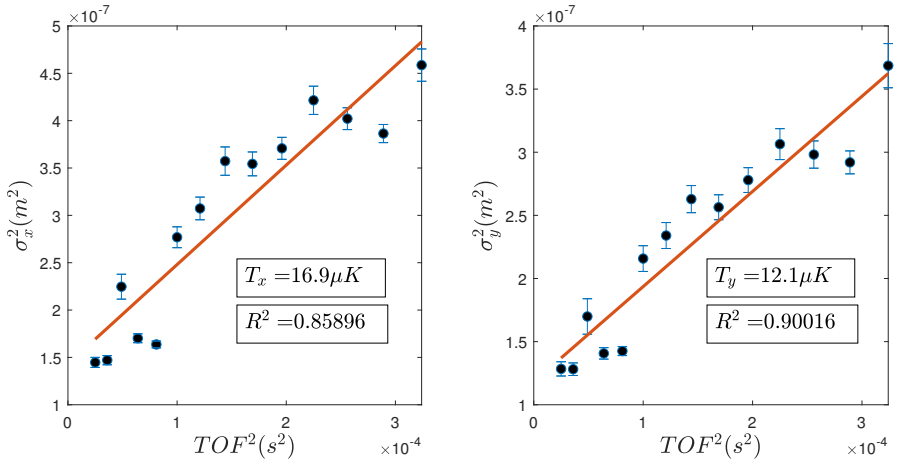

Figure 4.19: Temperature measurements, T_x and T_y after 10 ms of CMOT and 15 ms of optical molasses. For these results, $\Delta_{MOL} = -4\Gamma$ and $I_{MOL} = 0.2I_{SAT}$.

in the MOT (see figure 4.19). This demonstrates that the sub-Doppler cooling is being achieved in the molasses stage and the temperatures are comparable to other experiments performing the same cooling scheme [108, 109, 110].

4.2.4.2 Molasses Detuning

Once the optical molasses had been achieved, it was necessary to optimise the detuning of the cooling light. Figure 4.20 shows the temperature of the molasses in the y direction after release from the 15 ms of molasses cooling against the detuning used for the molasses cooling stage. The intensity of the light was dropped to $I = I_{SAT}/2$. From the results in figure 4.20 the optimal value of Δ_{MOL} is -10Γ as this is the coldest temperature. The trend implies that further detuning could help to cool even further however detuning past -10Γ was not possible in this configuration. The number density of the atoms at this detuning after the molasses cooling is measured to be 1.2×10^{11} cm^{-3}.

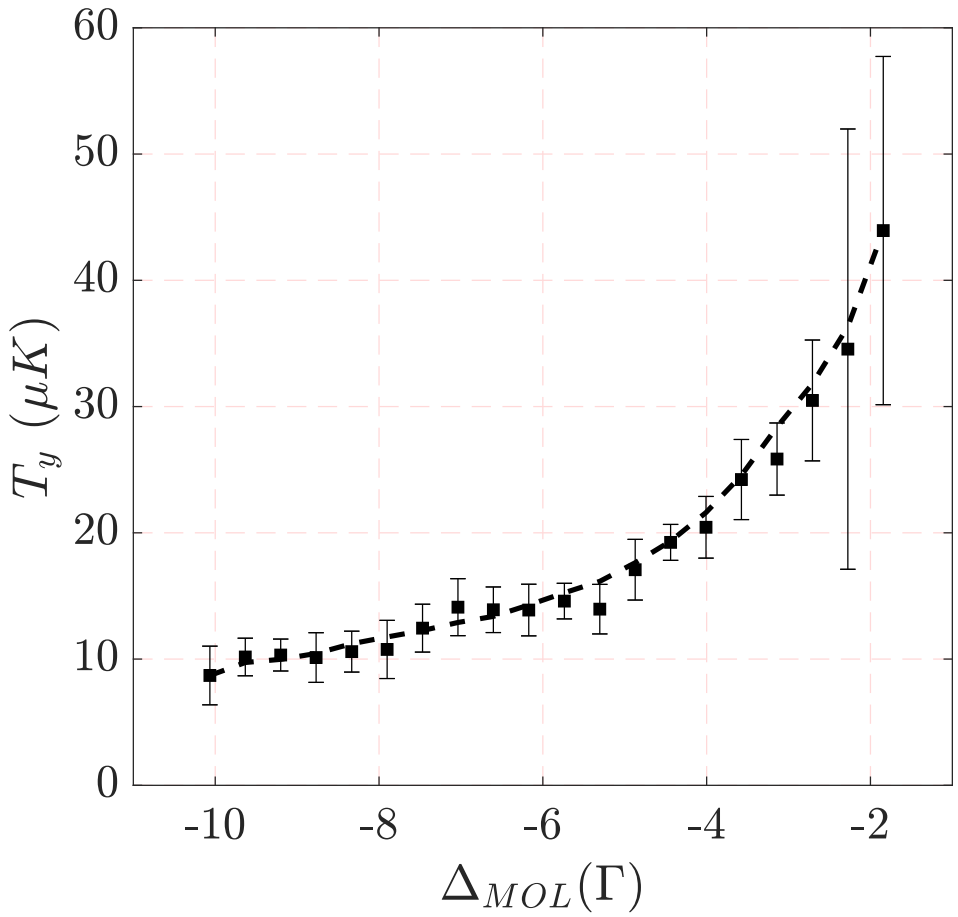

Figure 4.20: Temperature measurement, T_y after 20 ms of CMOT and 4 ms of optical molasses at various detunings of the cooling beam. $I_{MOL} = I_{SAT}/2$.

4.2.4.3 Molasses Intensity

The molasses cooling is also sensitive to the intensity of the cooling beams in the molasses phase. The cooling beam intensity is linearly ramped from I_{MOT}, the intensity used in the MOT/CMOT phase, to the final intensity I_{MOL} over the duration of the molasses cooling phase.

This can be seen in figure 4.21 showing that the temperature can be lowered with a lower final value of I_{MOL}. However at intensities below $I_{MOL} = I_{SAT}$ there is a sharp falloff in atomic density. Previous works suggest the need to maintain the atomic density at early cooling stages to maximise the atom number overlapping the dipole trap beam waists [111]. For this reason the intensity of the molasses beams was

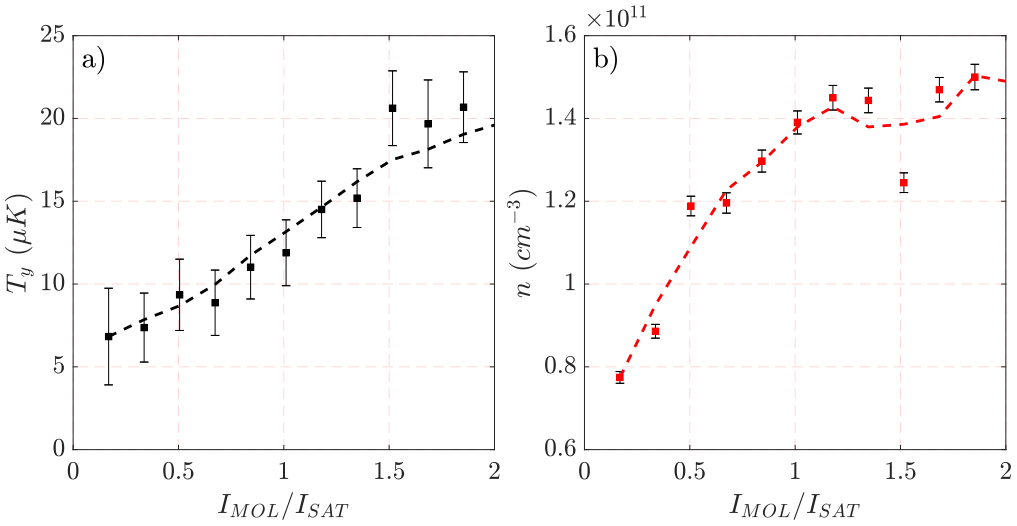

Figure 4.21: Temperature measurement, T_y and number density n after 20 ms of CMOT and 4 ms of optical molasses at varying final intensity of the cooling beam intensity ramp I_{MOL}. The value of I_{MOL} refers to the total intensity divided into six beams to give the average intensity per cooling beam and is normalised to the saturation intensity of the Cs cooling transition $I_{SAT} = 1.1023\,\mathrm{mW/cm^2}$ [96].

chosen to be $I_{MOL} = I_{SAT}$ and detuning $\Delta_{MOL} = -10\Gamma$.

4.2.5 dRSC

4.2.5.1 Raman Lattice Setup

To create the 3D lattice, 4 linearly polarised beams are arranged to intersect at the position of the atoms. The arrangement is shown in figure 4.22. Two beams counterpropagate in the $\pm y$ direction while the other two beams are running beams in the $+z$ and $+x$ direction. This 4 beam lattice arrangement has been used in several other experiments employing dRSC [68, 69]. The frequency of the lattice light is resonant with the $|F = 4\rangle \rightarrow |F' = 4\rangle$ transition, this acts to provide both the light for the depumping of the atoms from $F = 4$ to $F = 3$ and the lattice light red-detuned by $-9.2\,\mathrm{GHz}$ from $|F = 3\rangle \rightarrow |F' = 4\rangle$ [112, 113]. The polarisations of the x and z lattice beams are parallel which allows optical interference between these beams. An angle α in the linear polarisation between the $-y$ and $+y$ beams ensures interference between the $\pm y$ lattice beams and the x and z lattice beams. The magnetic field for creating the necessary Zeeman splitting in the ground state $\mathbf{B}_{dRSC}$ is

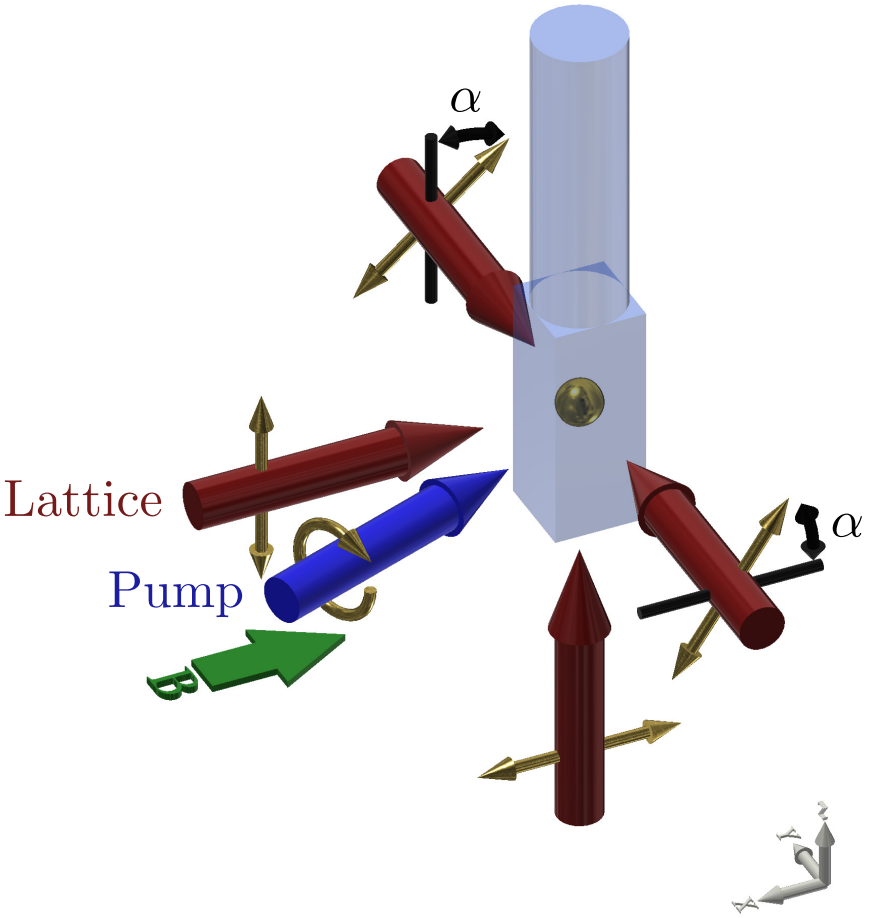

Figure 4.22: Optical arrangement for the lattice beams (maroon) needed for the 3D optical lattice and the pump beam (blue) for dRSC. The gold arrows represent the polarisation state of the light. The direction of the magnetic field used to induce degeneracy in the magnetic sublevels is shown in green.

provided by the compensation coils used for the optical molasses as described in section 4.2.4. A non-zero angle β between $\mathbf{B}_{dRSC}$ and the pump beam is required in order to produce the π polarised pump light. This angle has been reported to be optimal at $\beta \approx 5^\circ$ [70, 114]. The pump beam is thus arranged to create this condition. Figure 4.23 shows the schematic for the optical arrangements of the beams for the optical lattice. As the lattice beams must be linearly polarised it is not simple to mix them with the circularly polarised MOT and imaging beams so the $\pm y$ and x lattice beams are aligned with a slight angle to the y and x axis. The z beam has

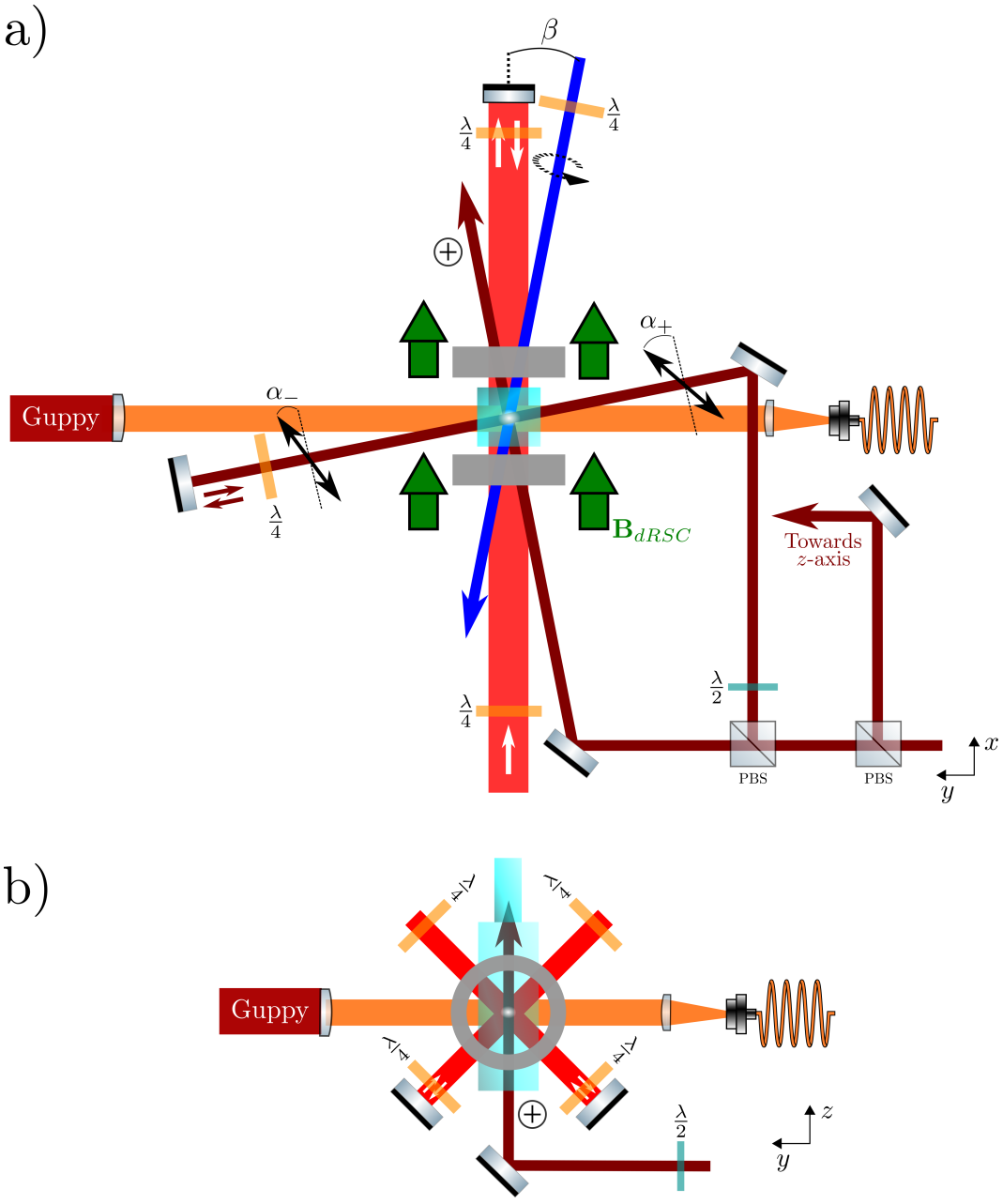

Figure 4.23: Schematics for the arrangement of the 4 beams required to create the 3D lattice (maroon) and the Raman pump beam (blue) for the dRSC. The MOT beams (red) and the imaging beam (orange) are also shown. a) shows the view from above while b) shows the view from the side.

full optical access from below the cell and hence can be aligned to be parallel with the z axis. The $\pm y$ lattice beam is created by retroreflection via a mirror and a QWP which turns the polarisation of the returning wave to create the angle α_-. Typically $\alpha_\pm = 45 \pm 10°$.

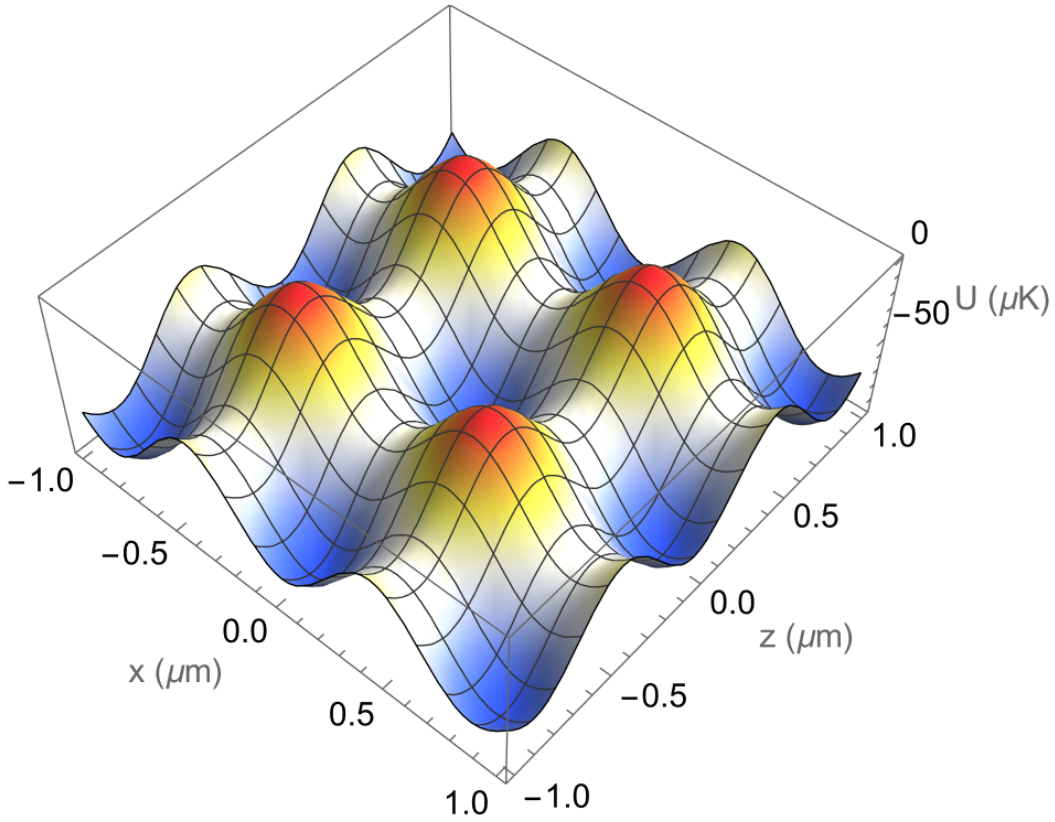

Figure 4.24: Calculated potential surface of the real part of equation 2.43 with the intensity and detuning parameters used in the dRSC stage at the origin of the lattice.

4.2.5.2 Calculation of Raman Lattice Parameters

Calculating the parameters of the Raman lattice is useful for estimating the efficacy of the cooling scheme. The dipole force from a laser occurs due to the AC stark shift of the hyperfine levels of the atoms by the electric field of the laser light. The lattice beams are resonant with the $|F = 4\rangle \rightarrow |F' = 4\rangle$ transition which detunes the lattice beams from the $|F = 3\rangle \rightarrow |F' = 4\rangle$ transition by $\Delta = -2\pi \times 9.2\,\text{GHz}$. This detuning is large enough to be considered off-resonant and therefore U_0 can be approximated by equation 2.53 [115]. The power of each lattice beam was $P = 10\,\text{mW}$ with a $1/e^2$ waist radius $w_0 = 1\,\text{mm}$. The orientations of the polarisations give rise to Raman coupling in the x-z plane and thus it is useful to consider the optical potential of the Raman lattice in that plane. Figure 4.24 shows the potential landscape of the Raman lattice in the x-z plane at the origin where the lattice beams are at peak intensity. We see the minimum potential depth of $V_0 = 97\,\mu\text{K}$ is nearly a factor of

10 higher than the molasses temperature of $T_{MOL} = 12\,\mu K$, allowing for trapping. To get an understanding of the average trap frequency in the x-z plane, the average intensity for the trapping beams is used to recalculate the surface in figure 4.24. This yields an average potential depth of $V_1 = 48.5\,\mu K$ which can then be used to calculate the vibrational frequency of the optical lattice in the x axis ω_x

$$\omega_x = \sqrt{\frac{2V_1k^2}{m}}, \tag{4.6}$$

which yields $\omega_x = 2\pi \times 91\,kHz$. This result can then be used to estimate the strength of the bias field B_x required to bring the vibrational levels of the Raman lattice into degeneracy

$$B_x = \frac{\omega_x \hbar}{g_L \mu_B}, \tag{4.7}$$

which gives $B_x = 261\,mG$. It is also important to realise that the lattice beams can heat the atoms through photon-atom scattering and so it is useful to calculate the expected heating rate of a single lattice beam $\dot{T}_{LAT}$,

$$\dot{T}_{LAT} = T_{rec}\Gamma_{sc}, \tag{4.8}$$

where T_{rec} is the recoil temperature of Cs (200 nK [96]) and Γ_{sc} is the scattering rate of the lattice photons given by

$$\Gamma_{sc} = \frac{3c^2}{2\hbar\omega_0^3}\left(\frac{\Gamma}{\Delta}\right)^2 I(z,r). \tag{4.9}$$

Multiplying for all 4 lattice beams at the average beam intensity $P/(\pi w_0^2) = 397\,mW/cm^2$ gives the total heating rate as $4\dot{T}_{LAT} = 377\,nK/ms$. Over a brief lattice duration (10 ms) this should not heat the atoms to a temperature higher than the trap depth.

4.2.5.3 Cooling into the Raman Lattice

The trap depth of the Raman lattice is on the same order of magnitude as the temperature of the atoms in the molasses phase so this makes it difficult to fully trap the

atomic sample. This can be overcome with dRSC as the atoms can cool while the lattice turns on which allows for a more efficient loading and trapping of the atoms in the lattice [116]. Initially, the lattice parameters are suboptimal for loading the Raman lattice fully, so the conditions for dRSC are enacted for a phase duration τ_{dRSC} allowing for a fraction of the atoms to cool into the Raman lattice. This effect

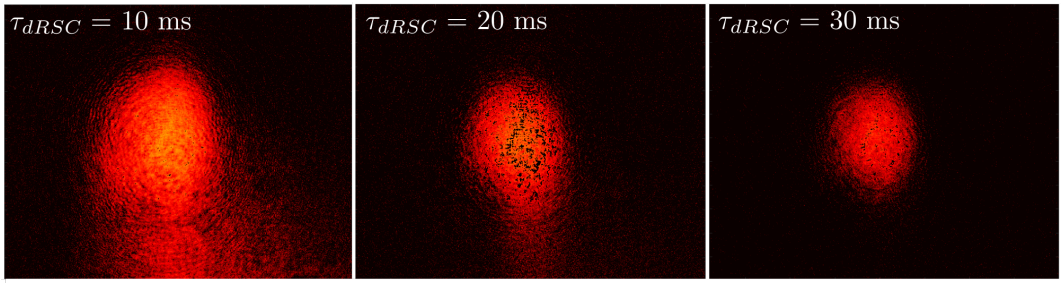

Figure 4.25: Absorption images of the atoms after a dRSC phase of varied duration τ_{dRSC}. The images are taken after 4 ms TOF from release of the lattice. Gravity points downward.

can be seen in figure 4.25, where as τ_{dRSC} increases the atoms that are not trapped in the Raman lattice fall under gravity out of the image, while the atoms that are trapped remain in the lattice. From this point, it was a matter of optimising the various parameters of the dRSC phase in order to maximise the PSD.

Figure 4.26 shows the atom lifetime in the dRSC phase. Inter-atomic collisional losses lead to an exponentially decaying lifetime in the dRSC lattice with a measured $1/e$ lifetime of 8.4 ms. The atomic decay from the trap encourages the optimisation of τ_{dRSC}.

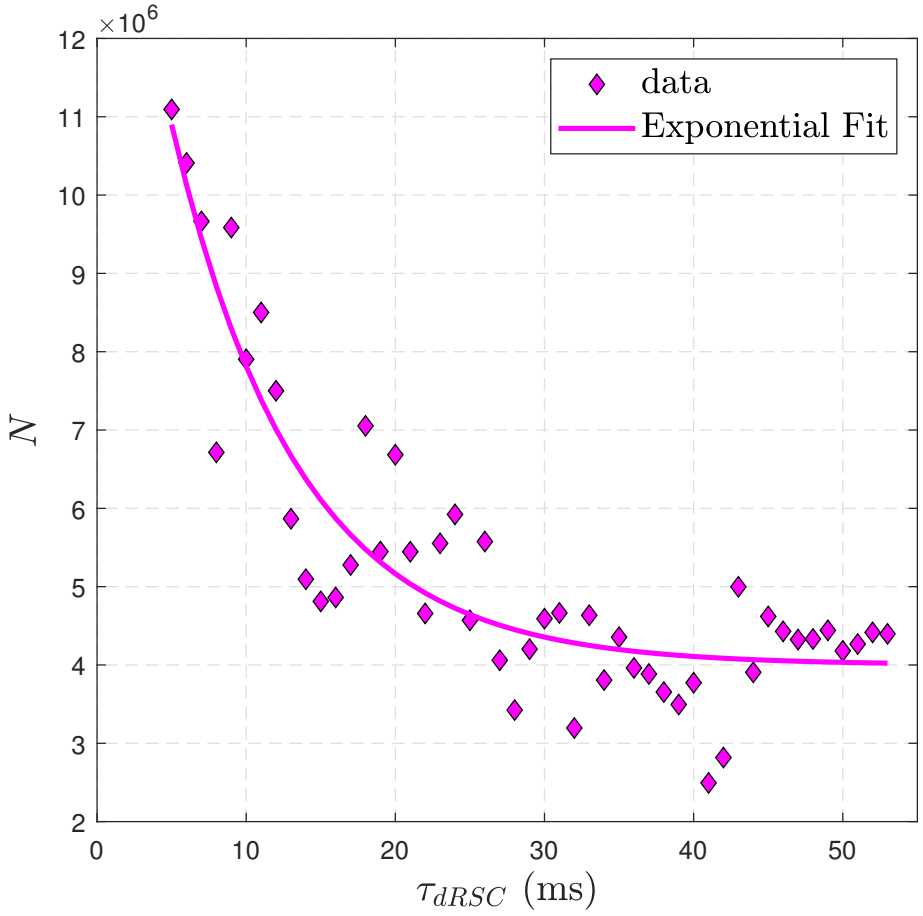

Figure 4.26: Atom number measured immediately after the dRSC phase for varying duration τ_{dRSC}. An exponential fit is overlayed on the data.

4.2.5.4 Measuring Raman Lattice Trap Depth

Verifying the lattice depth is comparable to the estimates calculated in section 4.2.5.2 is useful for determining whether or not the variables have been appropriately optimised. It is possible to infer the trap depth by driving the lattice light amplitude at double the vibrational frequency of the trap to induce parametric heating of the atoms and forcing atomic loss from the lattice [117, 118]. The amplitude of the lattice beams was modulated at a frequency ω_{AM} at a depth of 50% over the full duration of the dRSC phase where $\tau_{dRSC} = 20\,\text{ms}$.

Figure 4.27 shows that when $\Omega_{AM} = 2\pi \times 75\,\text{kHz}$ there is a strong decline in atomic density in the lattice. This is the point where the atoms are experiencing reso-

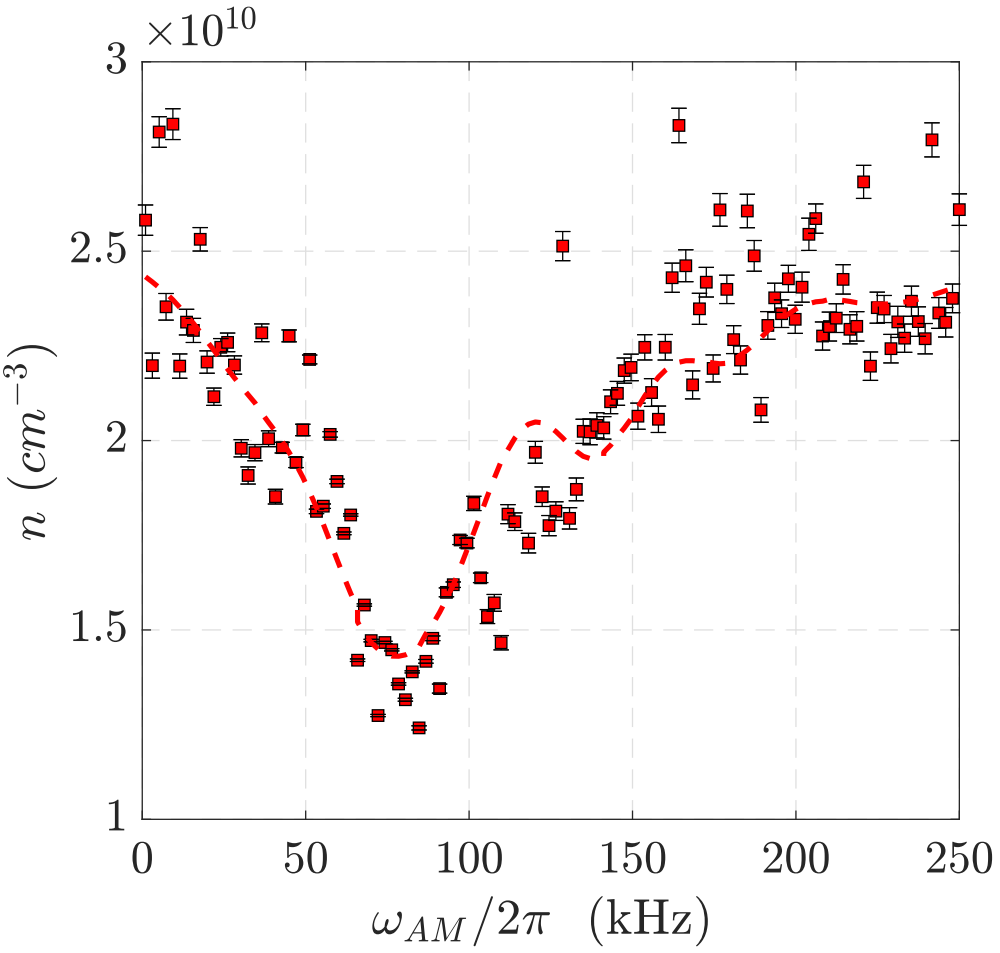

Figure 4.27: Number density of the atoms remaining in the lattice after modulating the trap depth by 50% at a frequency ω_{AM}.

nant parametric heating and escaping the optical potential. Assuming that this is excitation of the x degree of freedom then $2\Omega_x = 2\pi \times 75\,\text{kHz}$ which would give $B_x = 107\,\text{mG}$ more than a factor of two smaller than the value calculated in section 4.2.5.2.

4.2.5.5 Raman Pump Parameters

The parameters of the Raman pump were investigated to examine their performance. The detuning of the Raman pump Δ_{pump} from the $|F=3\rangle \rightarrow |F'=2\rangle$ transition, is critical to reaching optimal cooling into the Raman lattice. Figure 4.28 shows the density of the atoms loaded into the Raman lattice after 20 ms of dRSC. The loaded density is strongly asymmetric about the resonance of the $|F=3\rangle \rightarrow |F'=2\rangle$ transition with the maximum occurring at $+3\,\Gamma$. This asym-

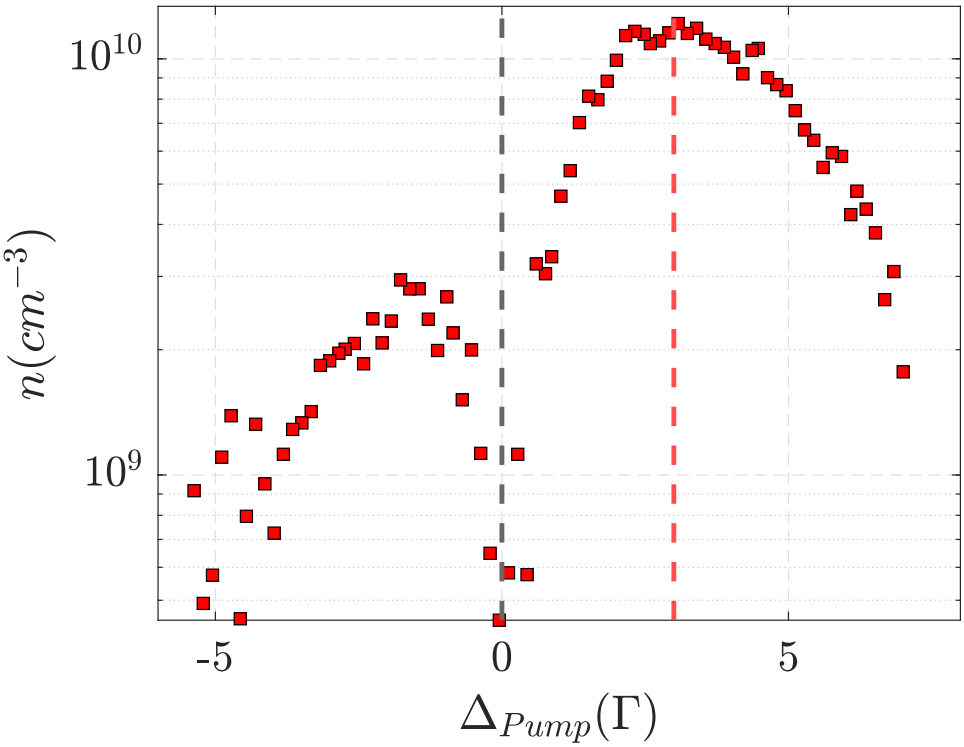

Figure 4.28: Number density of the atoms loaded into the lattice with varying Raman pump detuning Δ_{pump} from the $|F=3\rangle \rightarrow |F'=2\rangle$ transition. The dashed red line signifies the maximum at $+3\Gamma$.

metry is also reported in [70, 116, 119] and is explained by the vector light shift introduced by the Raman pump beam. The Raman pump introduces an effective magnetic field which detunes the magnetic sublevels of $F = 3$ from degeneracy, decreasing the cooling efficiency. This effective magnetic detuning from the dRSC resonance is in competition with the optical pumping. For red-detunings, this effective magnetic field opposes the bias field and thus reduces the splitting between the magnetic sublevels. Whereas for blue-detunings, the effective magnetic field aligns with the bias field and increases the sublevel splitting which enhances the optical pumping and leads to a loading enhancement. One will also notice the distinct destruction of the dRSC cooling when tuned to resonance with $|F=3\rangle \rightarrow |F'=2\rangle$, it is at this point that the light shift is so intense that the Zeeman sublevels are shifted

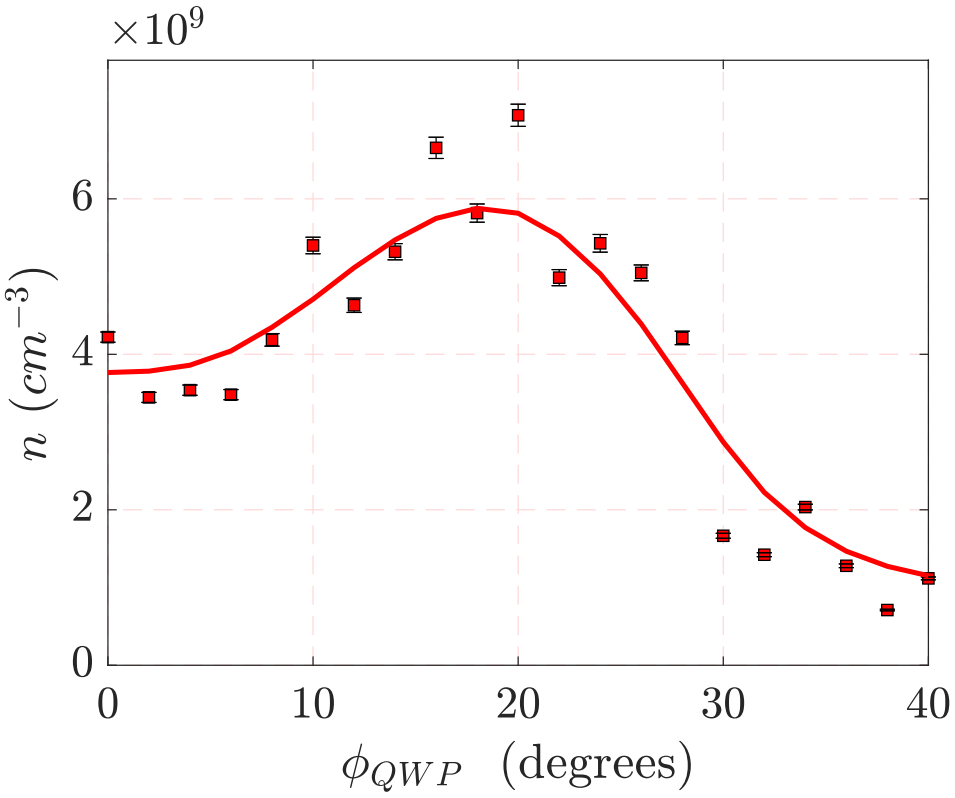

Figure 4.29: Number density of the atoms loaded into the dRSC lattice with varying pump QWP angle ϕ_{PUMP}. The solid line represents an exponential smoothing of the data with a bin width of 5 degrees.

so far out of degeneracy that the cooling is nullified [119][2].

Another property of the pump beam that needs consideration during optimisation is the ellipticity of the pump polarisation. This is initially set to be as close as possible to circularly polarised with coarse measurement, however the glass cell can distort the polarisation of the incoming beam so it is useful to check the pump polarisation by varying the QWP angle of the pump ϕ_{PUMP} and optimising the loaded density in the dRSC phase. Figure 4.29 shows the density of the atoms loaded into the dRSC lattice after a duration of $\tau_{dRSC} = 20\,\text{ms}$. The maximum occurs at $\phi_{PUMP} = 18^\circ$ and is hence set at this angle.

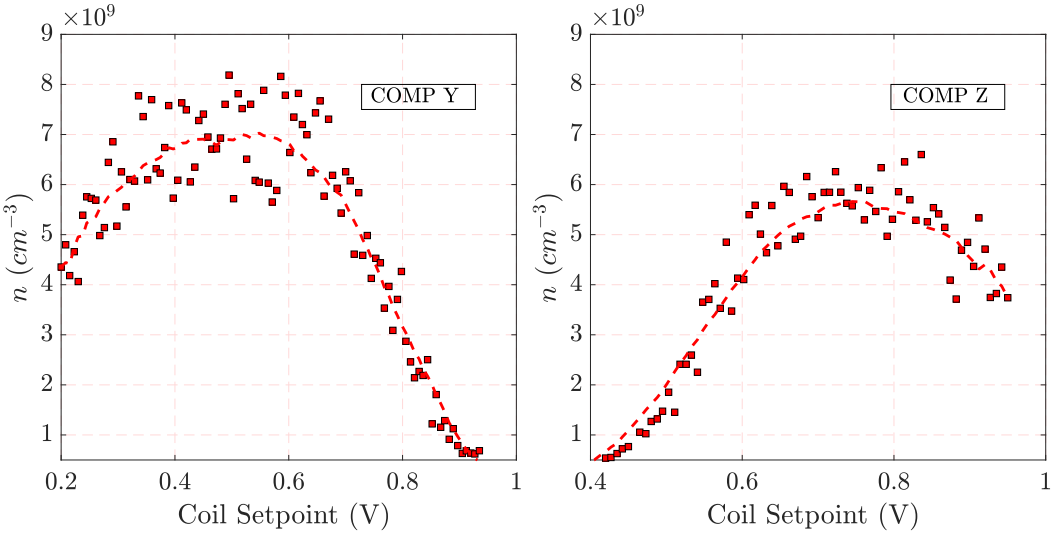

Figure 4.30: Number density of the atoms loaded into the dRSC lattice with varying compensation coil magnetic fields.

4.2.5.6 Aligning the Bias Field

As discussed in 2.3.4 a small amount of π polarised light is required to prevent a dark state from forming in the $|F=3, m_F=-2\rangle$ sublevel. To inject π polarised light into the system, the pump beam is aligned to be at a slight angle ($\approx$ 5-10°) to $\mathbf{B}_{dRSC}$ in the x-z plane. This is coarsely aligned via the position of the optics and then fine aligned by tuning the y and z compensation coils to tilt $\mathbf{B}_{dRSC}$. This can be shown in figure 4.30, the alignment of the compensation fields has a drastic impact on the density of the atoms after a duration of τ_{dRSC} =20 ms demonstrating an improvement in cooling efficiency with better $\mathbf{B}_{dRSC}$ alignment.

4.2.5.7 dRSC

To verify the efficacy of the dRSC phase, the pump beam polarisation was flipped with the bias field scanned in both directions. Figure 4.31 shows the normalised density of the atomic cloud after $\tau_{dRSC} = 20$ ms. The number density is maximised at the point of greatest cooling efficiency, which occurs at opposite bias field polarity for the σ^+ and σ^- polarisations. For the σ^- light, the maximum number density is about 20% higher than the σ^+ light, which is possibly due to imperfections in

[2]In theory, the light shift should cross zero at resonance, but various broadening effects (e.g power broadening from the pump, residual magnetic field inhomogeneity) will prevent all atoms from being on resonance with the pump simultaneously.

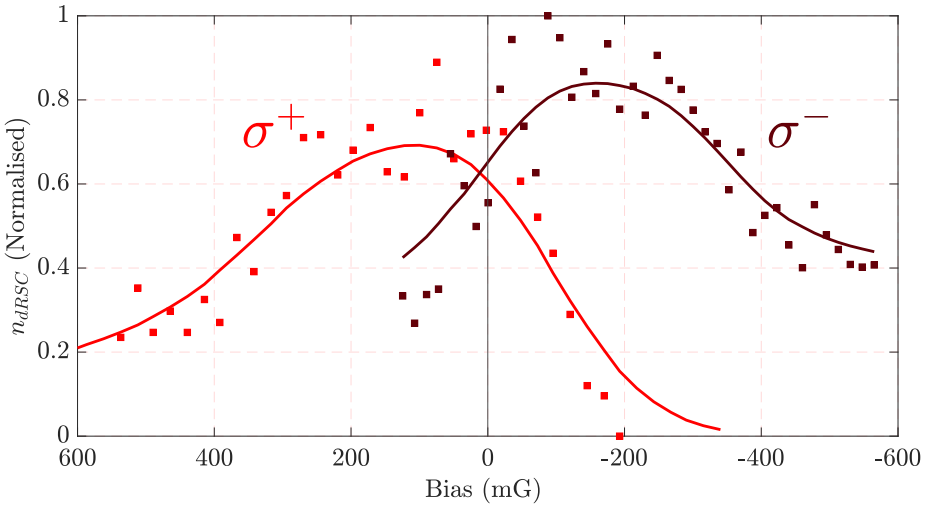

Figure 4.31: Normalised number density in the dRSC phase against bias field for the two helicities of the pump beam polarisation. The number density is normalised to the largest density recorded for all data in the figure. Squares show the data points while solid lines show a smoothed average. The line shows the midpoint between the two peaks which was calibrated to 0 mG.

the pump QWP. σ^- light was then chosen for the pump polarisation. The known symmetry of dRSC with bias field polarity allows the extraction of the true magnetic zero as the midpoint between the two peaks, therefore allowing fine calibration of the bias field measurement[3].

Figure 4.32 shows how the temperature changes as B_{Bias} is swept through the resonance. From the moving average, $B_x \approx 100\,\text{mG}$ provides the optimal cooling, which is more in line with the value predicted from the trap frequency measurement in 4.2.5.4 than from the calculated value in section 4.2.5.2. With further optimisation, the final temperature measured in the dRSC phase was measured as $T_{dRSC} = 3.1\,\mu\text{K}$ which gives a factor of 4 improvement on the molasses $T_{MOL} = 12.2\,\mu\text{K}$.

[3]This accounts for any imperfections in the alignment/positioning of the fluxgate sensors that measure the bias field (see section 4.1.9) or any non-linear magnetic field gradients that might add a residual offset to the measured bias field.

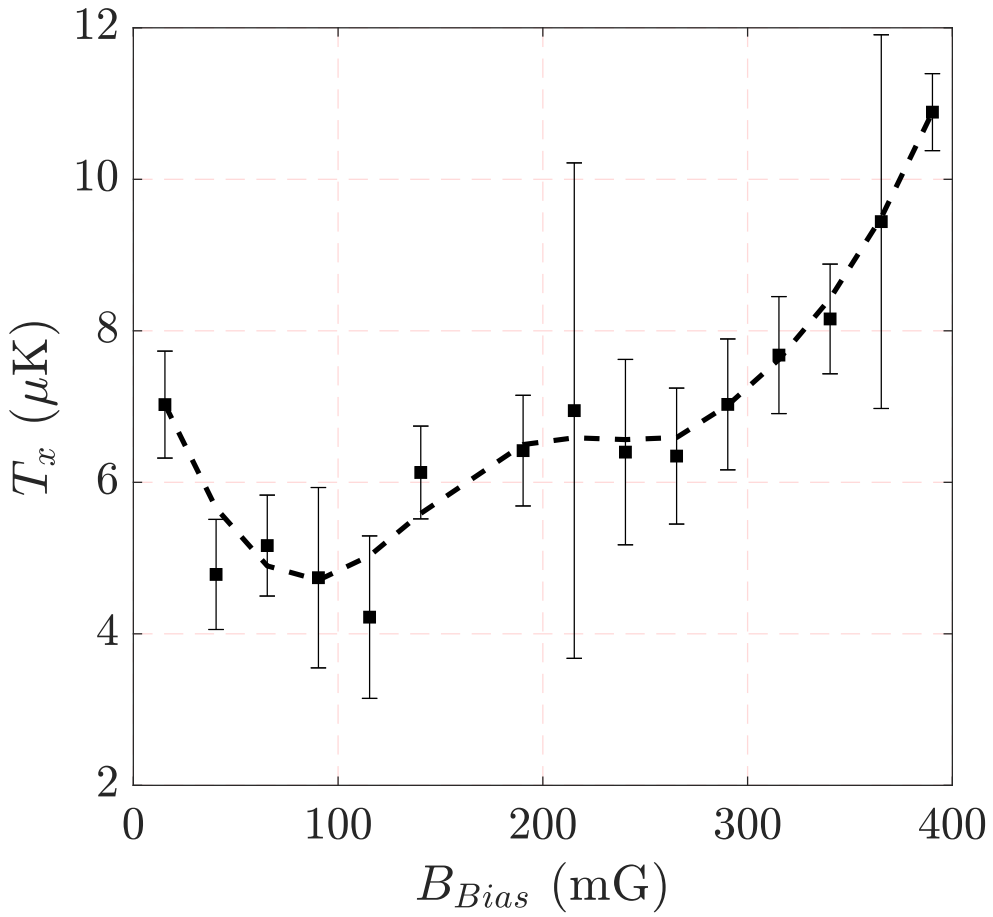

Figure 4.32: Temperature in the dRSC phase against bias field for $\tau_{dRSC} = 5\,\text{ms}$. The dashed line shows a smoothed average.

4.2.6 Dipole Trap

4.2.6.1 Lens testing

As discussed in section 4.1.7 very high intensities are required to create an optical trap potential deep enough to trap atoms in the optical dipole trap after the dRSC stage. Lenses are used to focus the light down onto the atomic cloud and reduce the waist of the beam such that the optical intensity is very high. The theoretical diffraction-limited minimum waist w_{min} can be found to be

$$w_{min} = \frac{2\lambda f}{\pi D} \tag{4.10}$$

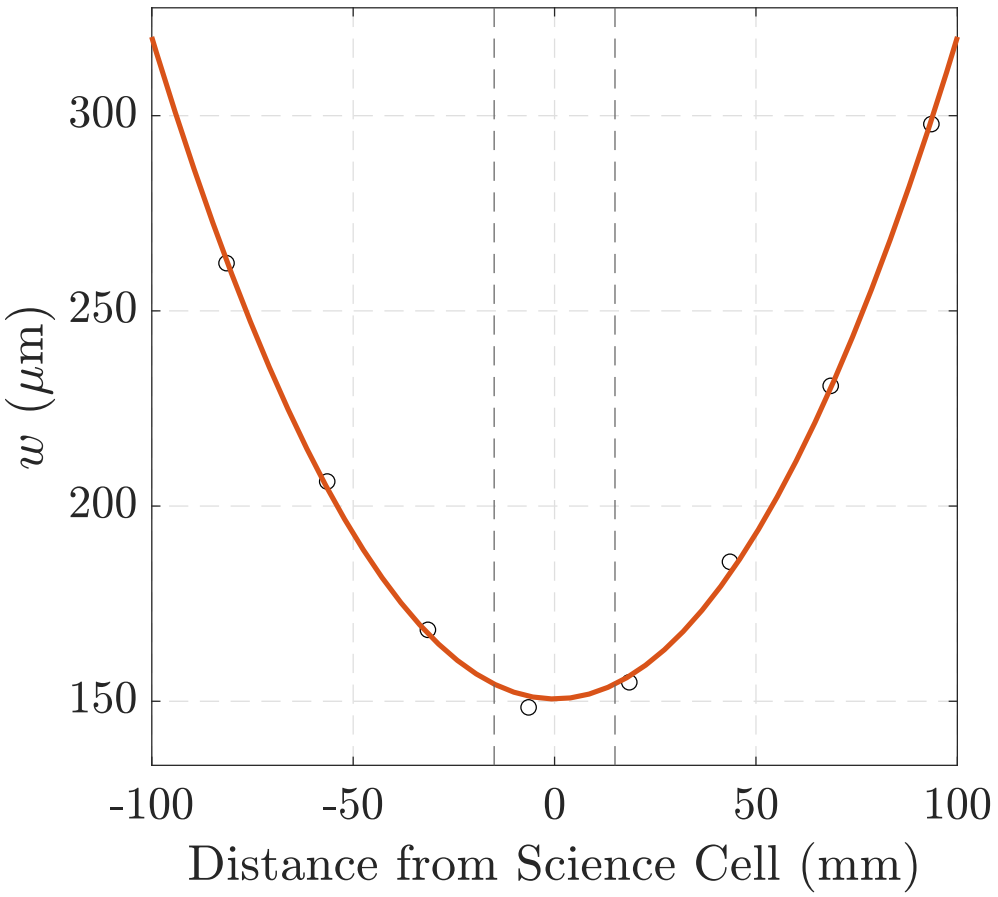

Figure 4.33: Beam radius of dipole trap beam versus the distance from the centre of the science cell. The open black dots represent the beam radius measurement while the red line is the fitted model of equation 2.52 to the data. The dotted lines represent the walls of science cell.

where D is the diameter of the collimated beam on the lens. Inputting the conditions of the dipole setup where $D = 10\,\text{mm}$ and $f = 750\,\text{mm}$ gives $w_{min} = 51\,\mu\text{m}$. Since it is difficult to accurately measure the beam path (as it passes through several optical elements) and imperfections can cause the effective focal length to change, it is vital to measure the waist in situ to make sure the focal point overlaps the atoms. To do this, the waist measurements are made indirectly by using the knife-edge method at a location 75 mm before the cell and then moving the lens axially along the beam. Once the minimum is found the lens can be moved 75 mm from this point towards the cell and the focus can be assumed to overlap the centre of the science cell. The results in figure 4.33 show the waist of the dipole trap beam through the focal point.

The results were then fit to equation 2.52 and returns the value of $w_0 = 151\,\mu m$.

4.2.6.2 Dichroic Mirror Testing

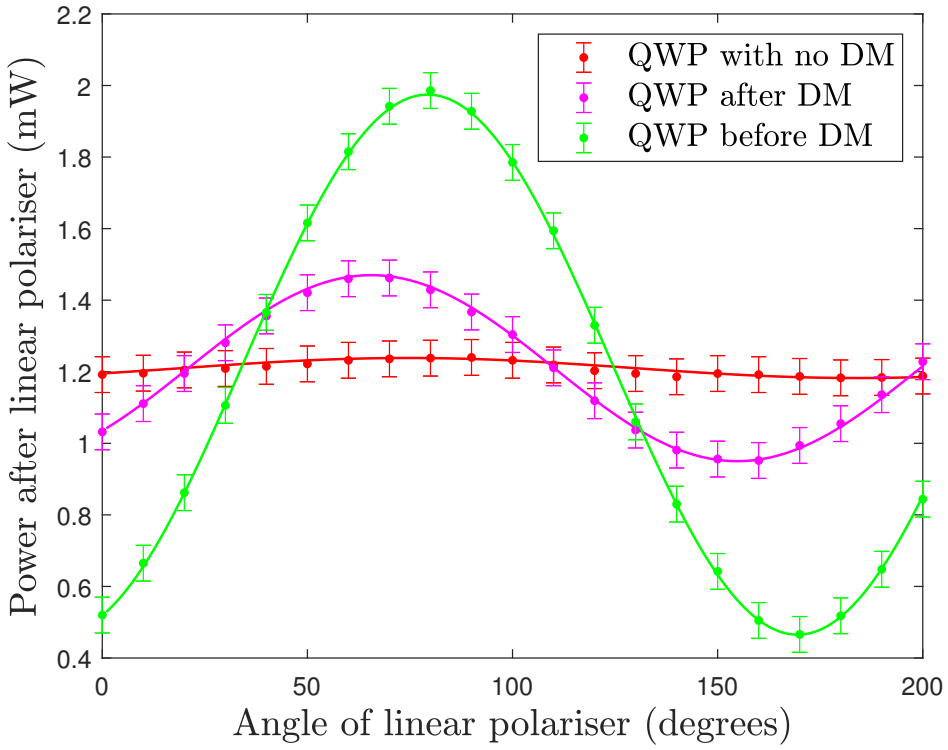

Figure 4.34: Transmitted power after the linear polariser versus the angle of the polariser for the three configurations of QWP and DM. The solid lines show the fitted curves with equation 4.11.

Setup	P_{cir} (mW)
No DM	1.18
QWP after DM	0.95
QWP before DM	0.47

Table 4.1: Extracted values of P_{cir} from the data in figure 4.34.

The dichroic mirrors (DM) are used to allow both the MOT and the dipole trap beams to propagate in the same optical path so as to greatly reduce the geometric complexity of the experiment. However this optic can produce unwanted polarisation changes in the MOT beam due to a disparity in the reflectivities of p and s polarisations on the DM surface. To test this the MOT beam was passed through the QWP used to circularly polarise it. After this it was passed through the DM and then a linear polariser. The polarisation of the MOT beam could then be extracted

by sweeping the angle of the linear polariser, ϕ_{Pol} and observing the transmitted power, P, with a powermeter. This measurement was then repeated with the DM mirror and the QWP position swapped, and again repeated with the DM removed. Figure 4.34 shows the data sets for each case. The results for each case can be fitted to the equation

$$P = P_{lin}\cos^2(\phi_{Pol} - \phi_0) + P_{cir} \tag{4.11}$$

where P is the power of the light after the polariser, ϕ_0 represents the angle of linear polarisation with respect to the polariser at 0 degrees and P_{lin} and P_{cir} represent the power contributions from linear and circular polarisation respectively. The circular contributions for the three setups can be summarised by table 4.1. This leads to the conclusion that placing the QWP behind the DM maximises the circular polarisation in the MOT beam and hence the optics are placed in this order. This can be seen in figure 4.11. This decision has the tradeoff that the 1064 nm dipole trap beam will pass through the 852 nm QWP for the MOT beam. The optical lattice needs to be linearly polarised to minimise the effect of differential light shift [120, 121], so a 1064 nm HWP is placed in the path of the lattice beam before hitting the DM. This allows the linear polarisation of the dipole trap beam to be aligned to the fast axis of the 852 nm QWP after the DM, which prevents the dipole trap light from becoming elliptically polarised.

4.2.6.3 Modelling the Dipole Trap

Similarly to the Raman lattice, modelling the dipole trap yields estimations on the parameters of the trap to predict efficacy and performance. The intensity of a focused laser beam is given by the function in equation 2.52. The dipole potential given by this beam is calculated in a similar way to the Raman lattice, except now the wavelength of the light is 1064 nm and so the coupling to the D_1 line is now no longer negligible with respect to the coupling to the D_2 line. For the single-beam dipole trap (SD) assuming the measured beam waist $w_0 = 151\,\mu\text{m}$ and an input power of $P = 10\,\text{W}$ gives a potential surface that can be seen in figure 4.35. This calculation yields a minimum trap depth of $V_{SD} = 68\,\mu\text{K}$

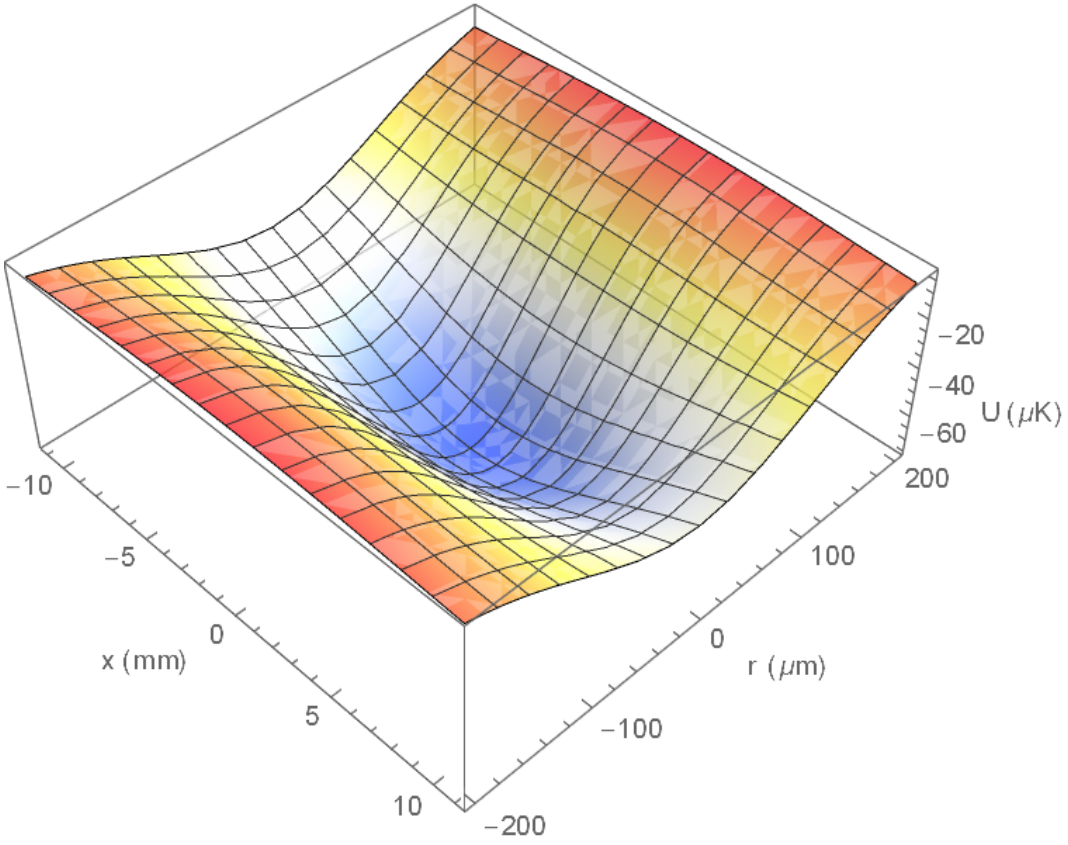

Figure 4.35: Optical potential surface for the single-beam dipole trap as calculated with the measured beam quantities. Calculation was made utilising equation 2.54.

4.3 Discussion

Ultimately the Cs apparatus was successful at cooling to the μK level using dRSC. The final conditions of 2×10^7 atoms at $T = 3\,\mu K$ are consistent with several other experiments employing dRSC to cool Cs [97, 110, 122] (1 μK, 1.4 μK, 2 μK). The temperature measured is over an order of magnitude lower than the modelled trap depth for the single beam dipole trap outlined in section 4.2.6.3 which is a promising start point for loading the dipole trap. Several Cs BEC experiments have started from similar starting conditions and managed to load a crossed dipole trap with $\simeq 10^6$-10^7 atoms which can then be optically evaporated to form BECs of $\simeq 10^5$-10^6 atoms [97, 122, 123]. The dipole trap system was built, tested and several attempts were made to trap atoms after the dRSC stage but were unsuccessful. It is likely that dipole beam alignment was the issue, as the sensitivity to this variable is

extremely high for the dipole trap due to the small length scales involved[4]. The trap depth may also have deviated from the calculated result: the glass cell could have caused lensing of the dipole beam changing the true waist size at the atoms, the M^2 value of the beam profile could have changed at very high power and the focussing lenses themselves could have been experienced thermal effects leading to a change in their nominal focal point. Additionally, the effect of the gravitational potential of the atoms (see section 5.1.4) could have proved detrimental to the trapping and would have required a vertical magnetic gradient field for levitation. In the end, disruptions due to COVID-19 meant that the project was put on hold in order to concentrate time and resources on the Rb BEC experiment.

[4]This can be seen for the Rb dipole trap in section 5.1.3.

Chapter 5

Bose-Einstein Condensate Magnetometer

In this chapter I present work developing an RF-AM based on a ^{87}Rb BEC. This work started with the optimisation of an existing ^{87}Rb BEC setup to improve the atomic number and density after the final optical evaporation sequence. From here an RF-AM was demonstrated using atoms trapped in a dipole trap and the work led to a publication

- Y. Cohen, B. Maddox, C. Deans, L. Marmugi, and F. Renzoni, "A radio-frequency Bose–Einstein condensate magnetometer," *Applied Physics Letters*, vol. 120, no. 16, p. 164002, 2022

5.1 Rb BEC

5.1.1 BEC Setup

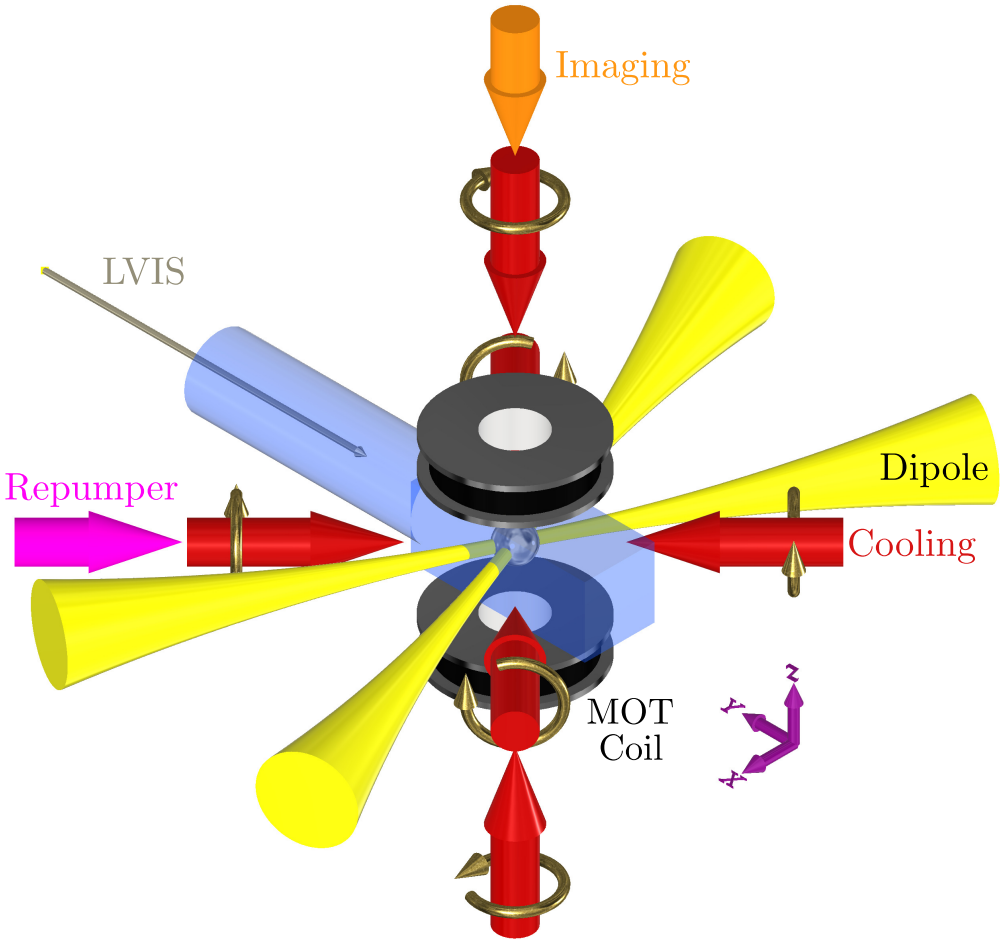

Figure 5.1: Diagram of the experimental setup used to produce the BEC for magnetometry. The atoms are shown as a silver sphere in the centre of the glass cell. Red, magenta and orange arrows represent the cooling, repumper and imaging beams respectively. Copper arrows are used to represent the polarisation of the beams. The conical yellow cylinders represent the dipole beams focussed down onto the atoms. The science MOT is loaded via an LVIS beam which is shown propagating in the y axis. Gravity points in the -z direction.

The Rb BEC experiment starts with a double MOT system housed in a vacuum chamber very similar to the design in the Cs experiment outlined in section 4.1.2. The whole system comprises two chambers: an LVIS chamber and a science MOT chamber connected by a vacuum impedance. The LVIS MOT chamber is pumped by a small ion pump (20 L/s Varian Starcell) to hold the Rb vapour at 5×10^{-8} mbar.

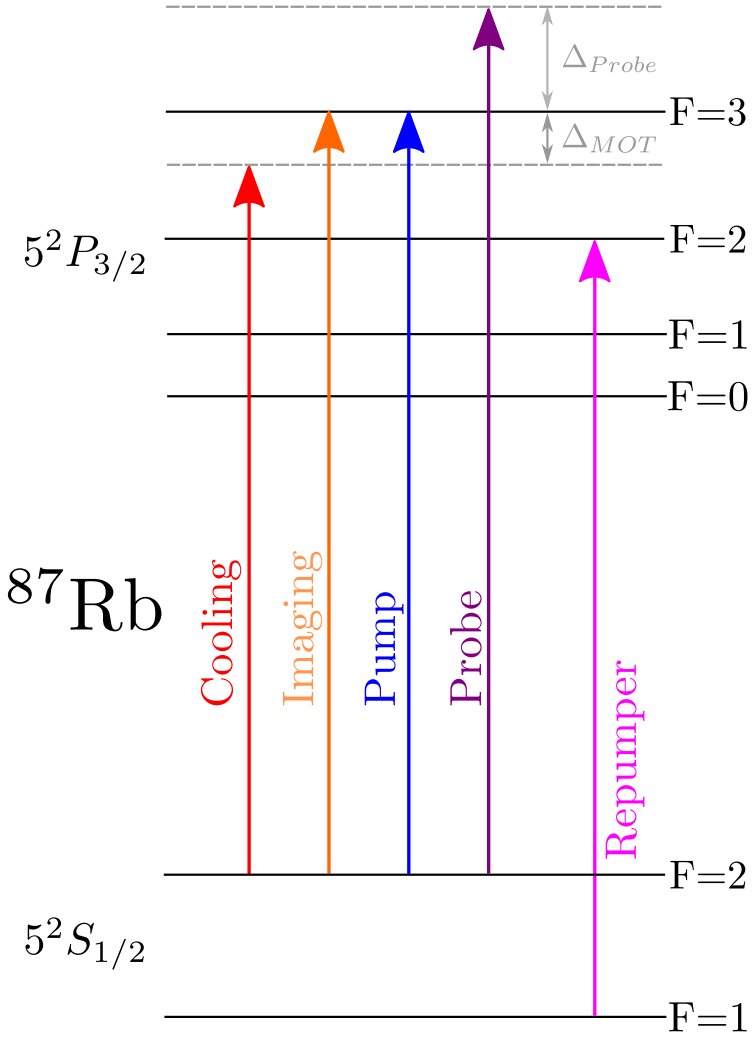

Figure 5.2: Level diagram of the ^{87}Rb D_2 line [84] showing the tuning of the near-resonant beams with respect to the hyperfine transitions.

The Rb is provided by a solid reservoir attached in a smaller valved off section and is heated at 110 °C. The science MOT features a glass cell with the same geometry as the Cs experiment and pumped down via a larger ion pump (55 L/s Varian Starcell) and a getter pump to $<1\times10^{-10}$ mbar. Figure 5.1 shows the science MOT setup with the LVIS beam loading. The MOT cooling beams, each 20 mm in diameter, form 3 orthogonal molasses beam pairs, one pair in the z axis and two pairs in the lines bisecting the x and y axes. The rempumper is mixed into one of the cooling beams via a PBS. The MOT coils are aligned along the z axis and provide 2.8 (G/cm)/A of gradient in the z direction. The imaging beam propagates down the z and is lensed onto a CCD camera to provide absorption imaging of the

atoms.

5.1.2 Experimental Sequence

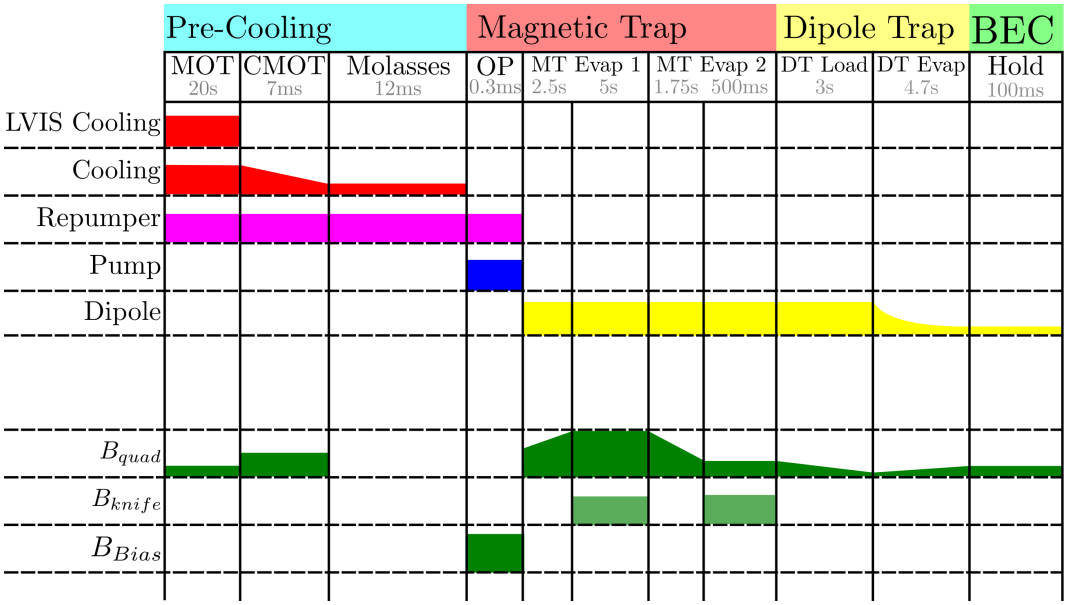

Figure 5.3: Experimental sequence of the Rb BEC cooling cycle. The main stages are subdivided into several phases with each phase duration indicated in grey underneath. The list is broken into two groups, the upper group (LVIS Cooling, Cooling, Repumper, ...) illustrates the corresponding laser intensity, while the lower group (B_{quad}, ...) represents the magnitude of the magnetic field.

The experimental sequence to cool to the BEC can be divided up into four distinct stages, precooling, magnetic trapping, dipole trapping and evaporative cooling.

The precooling begins by loading 3×10^8 atoms into the science MOT for 20 s via the LVIS beam. For the MOT, B_{quad} is set at 30.4 G/cm with the cooling beams at 4.2 mW/cm^2 (2.5 I_{SAT}). The cooling light for the LVIS is then shuttered off and then a CMOT phase is enacted for 12 ms whereby B_{quad} is increased to 41 G/cm. The CMOT cooling light intensity is then ramped down to 3 mW/cm^2 (1.8 I_{SAT}) and detuned to -2.8Γ. Then a molasses phase of 7 ms cools the atoms to a sub-Doppler temperature of 20 µK. For this phase, the quad coils are turned off and the cooling detuning is increased to -5.6Γ. The atoms are then optically pumped for 0.3 ms into the magnetically-trappable state $|F = 2, m_F = 2\rangle$ state along a bias field

B_{Bias} in the z axis. The pump light is provided by the imaging beam.

Then the MT stage begins by stepping B_{quad} back up to 77 G/cm and then linearly ramped from this value to 156 G/cm over a duration of 2.5 s. The atoms are then held in this phase for 5 s as an RF knife magnetic field B_{knife} is linearly frequency chirped from $\omega_{knife} = 13 \rightarrow 3.5$ MHz to force evaporation from the MT. Then B_{quad} is linearly reduced to 28 G/cm in 2.2 s and then another burst of linearly chirped RF knife from $\omega_{knife} = 3.5 \rightarrow 0.5$ MHz is applied. This cools the atoms to 4 µK, ready to be trapped in the XDT.

The DT stage is partially overlapped with the MT stage. The dipole beams are activated to full power at the start of the forced evaporation in the MT and atoms are loaded into the XDT as they are cooled.

5.1.3 Dipole Trap Alignment

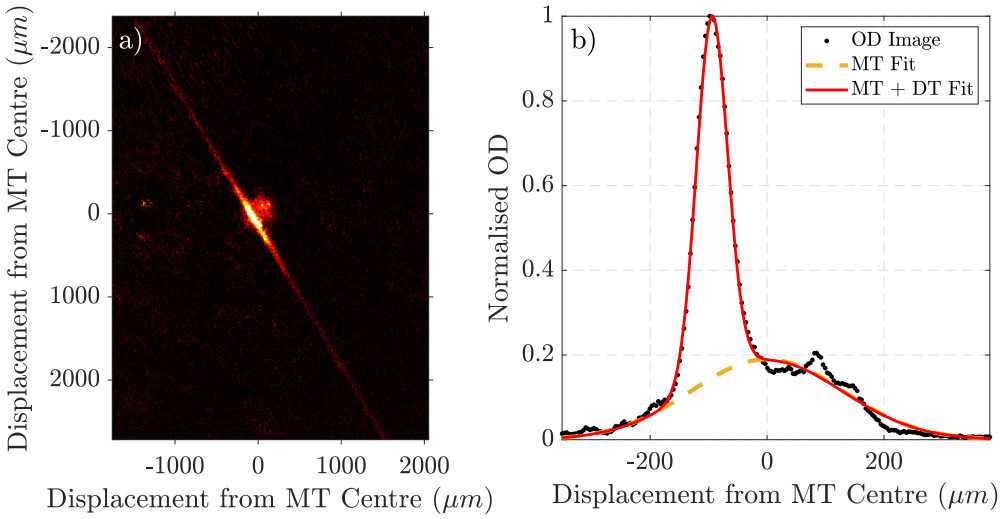

Figure 5.4: (a) Absorption image of the single-beam dipole trap (DT) intersecting with the magnetic trap (MT) at the end of the magnetic trap evaporation. (b) Interpolated cross-section of the OD image across the MT centre perpendicular to the axial direction of the DT.

After the magnetic trap phase, the atoms are loaded into a crossed dipole trap to vastly increase the density of the atomic cloud and begin further evaporation. The dipole beams are produced from an Ytterbium 1064 nm laser (IPG Photonics YLR-

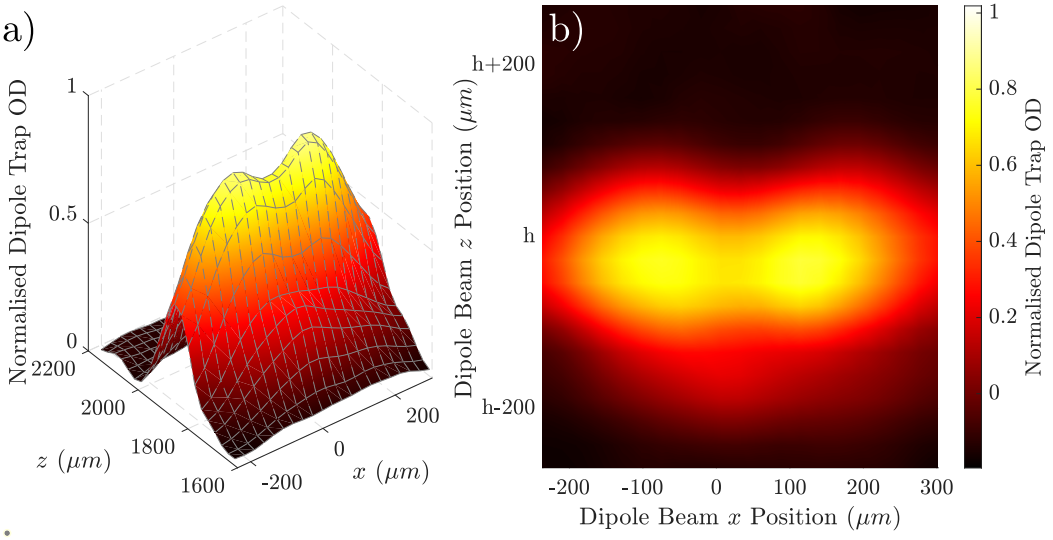

Figure 5.5: Surface plot a) of the normalised DT amplitude extracted from the DT+MT fit as the beam is raster scanned across the MT along with a flattened view b) of the surface plot. The dipole trap beam position is calibrated from the DT+MT fit.

20-LR). The dipole laser is split into two subsequent beams which are aligned to the magnetic trap in the x-y plane along two vectors x' and y' which intersect to form an angle of 26°. The x' (y') beam has a power of 4.4 W (2.6 W) and is narrowed to a waist of $w_{DT} = 80\,\mu\text{m}$ via $f = 500\,\text{mm}$ lenses. To facilitate efficient loading into the DT, the DT stage overlaps the MT stage by turning the DT on at the start of the MT stage.

Piezo mirrors are utilised to align the dipole trap beams. Initially this is done with each beam individually with the other dipole beam blocked. Figure 5.4a shows an absorption image of the dipole beam intersecting with the magnetic trap. Interpolating the OD image through a vector r that is perpendicular to the direction of the dipole trap can be seen in 5.4b. The data can be fitted with the summation of two gaussian distributions, one for the magnetic trap (MT) and one for the dipole trap (DT)

$$OD_r = A_{DT}\exp\left\{\frac{-(r-r_{DT})^2}{2\sigma_{DT}^2}\right\} + A_{MT}\exp\left\{\frac{-(r-r_{MT})^2}{2\sigma_{MT}^2}\right\} + c \qquad (5.1)$$

where A_{DT} and A_{MT} are amplitude coefficients proportional to the number of

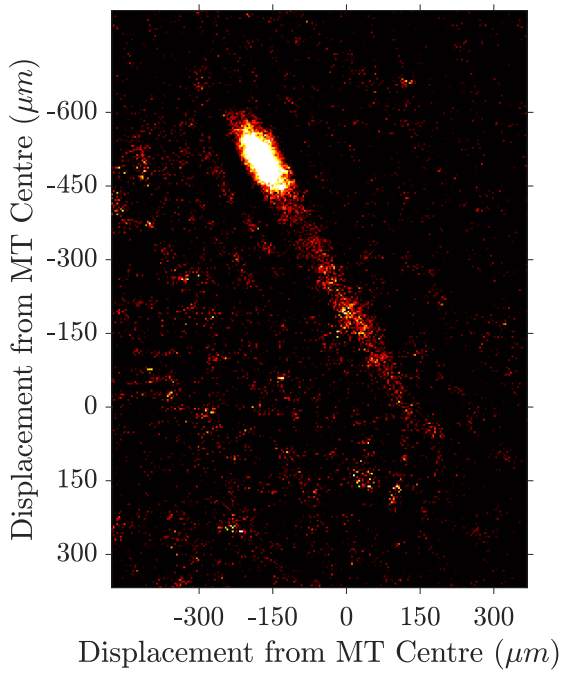

Figure 5.6: Absorption image of the XDT taken at 0.5 ms TOF after the DT hold phase.

trapped atoms in the DT and MT respectively. The piezo mirrors are stepped linearly and each shot is taken at 0.5 ms TOF. Since the pixel width PW is known and the absorption imaging beam propagates in the z axis, it is possible to calibrate the displacement of the DT centre to the MT centre in the x-y plane as $(\sigma_{MT} - \sigma_{DT})PW$. This can therefore calibrate the stepping of the piezo mirror in the x-y plane. Vertically, this calibration is impossible as the z axis is imperceptible to the imaging. However, as the piezo mirror stepping is symmetric in both axes, the scale of the movement in z can be inferred from the scale in the x-y plane. Figure 5.5 shows a surface plot of the A_{DT} extracted via equation 5.1 as the piezo mirror of the x' dipole beam was raster scanned across the MT. The surface shows two maxima symmetrically separated about the MT centre by approximately two beam widths. This is consistent with the notion of the Majorana losses as the dipole beams will cause the atoms to spend more time at the magnetic zero in the centre of the MT lengthening the duration in which they can undergo transitions between the m_F states

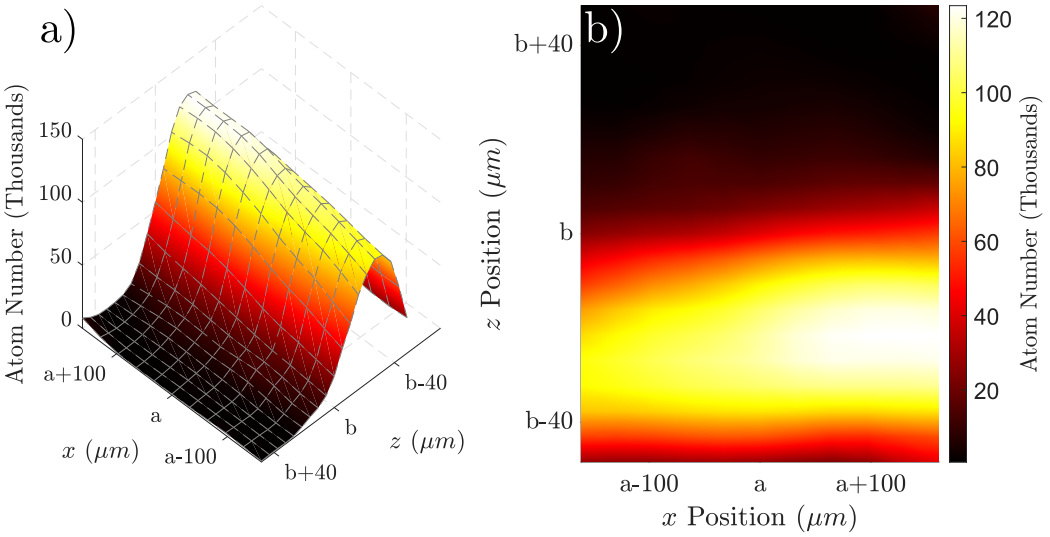

Figure 5.7: Surface plot a) and flattened view b) of the number of atoms loaded into the XDT as a result of rastering the y' with the x' beam held static. Absorption imaging is taken at 0.5 ms TOF. The positioning is arbitrarily defined as $a(b)$ in the $x(z)$ axis however the length scale uses the calibration from figure 5.5.

[124]. Once the optimum positioning was found for x' dipole beam the y' dipole beam was unblocked and raster scanned with the x' beam held at a fixed position to make a crossed dipole trap (XDT). For this step, the cooling sequence progresses past the magnetic trap, such that the XDT becomes the only relevant trapping force. This makes the alignment extremely sensitive as the atoms not trapped in the dimple of the XDT will be lost. Figure 5.6 shows an example of the image taken at TOF$=0.5$ ms after the DT load phase ends. The dimple can be seen clearly as the bright spot while the atoms caught in the x' beam are much less dense. The number of atoms trapped in the XDT as a result of the raster scan of the y' dipole beam can be seen in figure 5.5. The vertical alignment of the beams is clearly far more sensitive than the horizontal alignment which is consistent with the beams always being able to intersect in the x-y plane. Vertically, the XDT is almost completely destroyed by a misalignment of $w_{DT}/2 = 40\,\mu$m.

5.1.4 Dipole Trap Evaporation

Once the atoms are trapped in the XDT the final cooling stage initates via the trap weakening method. The total potential U_{TOT} becomes the sum of the XDT, the MT

and the gravitational potential of the mass of the atoms

$$U_{TOT}(x,y,z) = U_{XDT}(x,y,z) + U_{MT}(x,y,z) + gmz \tag{5.2}$$

which in the vertical direction z becomes

$$U_{TOT}(0,0,z) = U_{XDT}(0,0,z) + \mu_B m_F g_F \frac{\partial B_{MT}}{\partial z} z + gmz \tag{5.3}$$

where m is the mass of ^{87}Rb and g is the gravitational acceleration. From equation 5.3 the gravitational potential is linear across the trap centre. In the ideal anti-Helmholtz coil the magnetic gradients in each axis are approximately linear across the centre. The linearity of $\partial B_{MT}/\partial z$ can therefore cancel the detrimental effect of the gravitational potential and levitate the atoms in the XDT. Equating the magnetic forces and the gravitational forces acting on the atoms at the trap centre $\mu_B m_F g_F (\partial B_{MT}/\partial z) - mg = 0$ gives the approximate MT levitation gradient as $\partial B_{MT}/\partial z|_{LEV} = 15.2\,\mathrm{G/cm}$. To begin the evaporation process, the trap depth is progressively lowered by ramping the XDT beam powers down according to an exponential decay function. At the same time $\partial B_{MT}/\partial z$ is also ramped up linearly. The atoms are then held at the end of the ramping process for 100 ms for a final hold. Figure 5.8 shows the measured number density in the final hold of the dipole evaporation with varying final setpoints of the MT gradient and XDT potential. The final atom number is maximal at the strongest MT gradient and DT potential. This is consistent with the trap weakening method of evaporation, as the trap depth lowers, the hotter atoms escape the trap leaving a colder ensemble. The final number density however, has a maximal band across the parameter space. As U_{TOT} is lowered, the loss of atoms contributes to a colder sample which in turn leads to a higher density, however the geometry of the U_{TOT} depends on the ratio of MT gradient and DT potential. Therefore maximising the density requires tuning the potential landscape to maintain tight confinement as U_{TOT} is lowered. We can also see the effect of gravity, as the final MT gradient is lowered past the optimum, density drops off rapidly due to lack of vertical confinement.

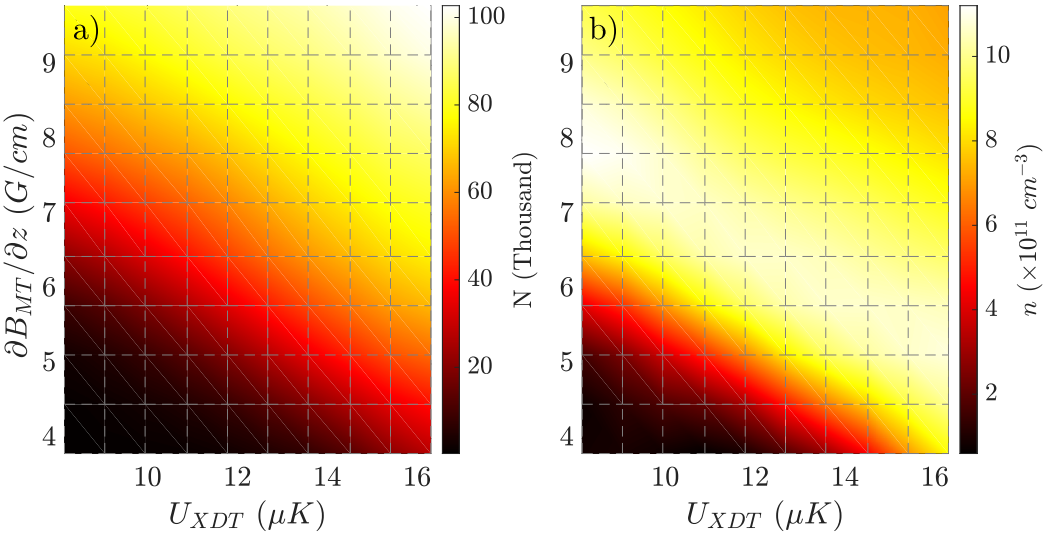

Figure 5.8: Surface plot of the number N a) and number density n b) of the atoms that survive the dipole trap evaporation sequence against the final values of the MT gradient and the optical potential of the XDT. TOF = 5 ms. The surfaces are smoothed by a Gaussian filter with standard deviation of 1.

5.1.5 BEC Formation

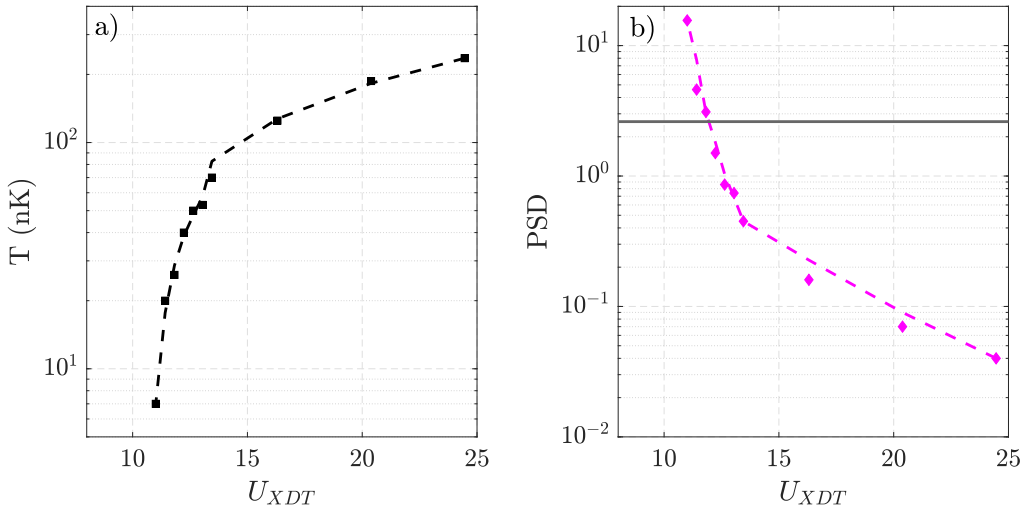

Figure 5.9: Final temperature a) and PSD b) of the atoms that survive the dipole trap evaporation sequence against the final values of the optical potential of the XDT. The grey horizontal line in b) shows the nominal PSD threshold of $D_{BEC} = 2.612$. Dashed lines show smoothed averages of the data.

The final PSD of the atomic cloud comes down to the final potential depth of the trap at the end of the optical evaporation. Figure 5.9 shows how lowering U_{XDT} increases the rate of evaporation and ultimately yields a colder sample yielding temperatures on the order of 10 nK that are over an order of magnitude below the recoil tem-

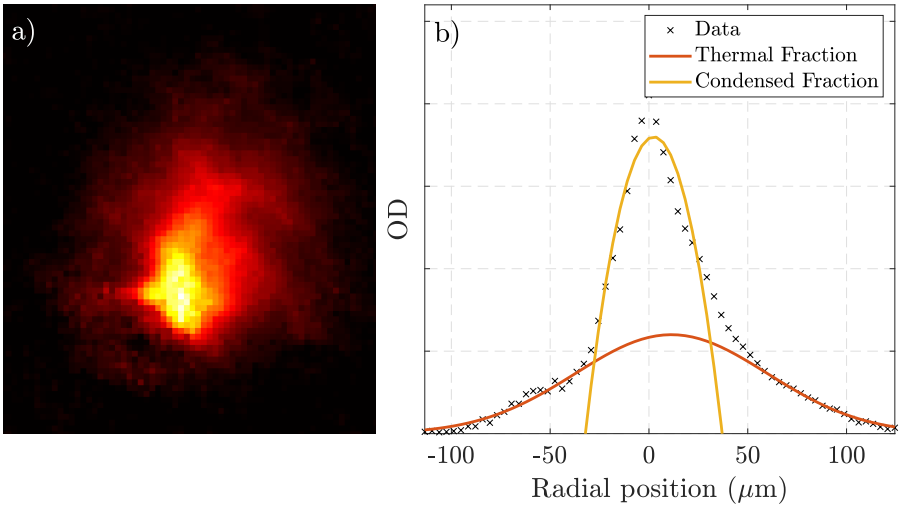

Figure 5.10: OD image a) and radial interpolation of the OD image of the atomic cloud b) when the BEC forms at the end of the evaporative cooling. Here $N_a = 40k$, TOF$= 15\,$ms and $D = 5.5$.

perature $T_{recoil} = 362\,$nK. Below $U_{XDT} = 12\,\mu$K the atoms cross the nominal PSD threshold of $D_{BEC} = 2.612$. Figure 5.10 shows an OD image of the atomic cloud at the end of the optical evaporation with an interpolation of the OD through the cloud along a radial vector. In the image we see a very dense centre with a more dilute periphery. By looking in the interpolation, it is clear to see that the density profile can no longer be described by just a gaussian distribution. As discussed in 2.5, the density profile of the BEC can be approximated as a parabola at the Thomas-Fermi limit. Hence we can fit the OD in 1D with a gaussian and an inverted parabola to represent the thermal and condensed fractions respectively.

5.2 Ultra-cold Magnetometry

5.2.1 Ultra-cold Magnetometer

Figure 5.11 shows the setup for the ultra-cold magnetometer. Aside from the atomic sample itself, the geometry of the beams and magnetic fields is identical to the standard RF magnetometer arrangement [125, 126]. During the MT stage of cooling, the pump beam spin-polarises the atoms into $|F = 2, m_F = 2\rangle$ along B_{Bias} in the z axis. The ultra-cold magnetometer can function in two regimes, with the atoms probed whilst held in the DT, or with atoms released from the MT/MOT that are

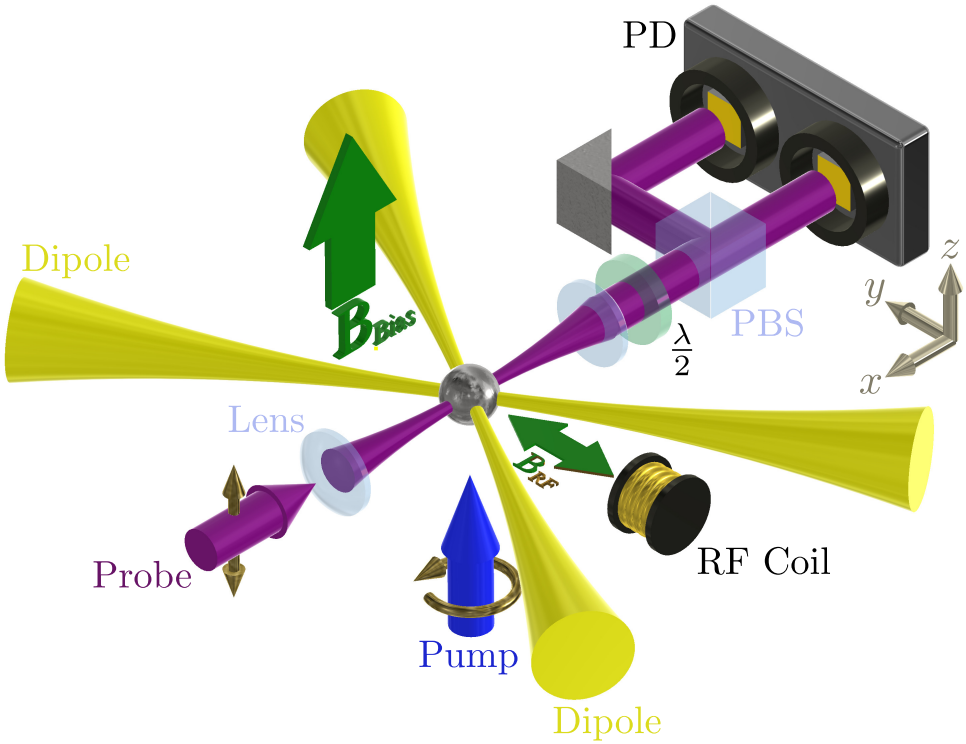

Figure 5.11: Diagram of the BEC magnetometer setup. The atoms appear as a silver sphere and illustrated as sitting in the bottom of the dipole trap potential. The probe beam enters along the x axis gets focussed onto the atoms via a lens and is then collected by a second lens and aligned to a polarimeter setup. The RF coil is aligned along y which provides B_{RF} perpendicular to the z axis. Gravity points in the -z direction. The pump beam is shown here to expound its orientation, but in reality it is pulsed on prior to the magnetometry stage and not active during the measurement. Figure adapted from [7].

untrapped and probed whilst falling.

5.2.2 Probe Beam Alignment

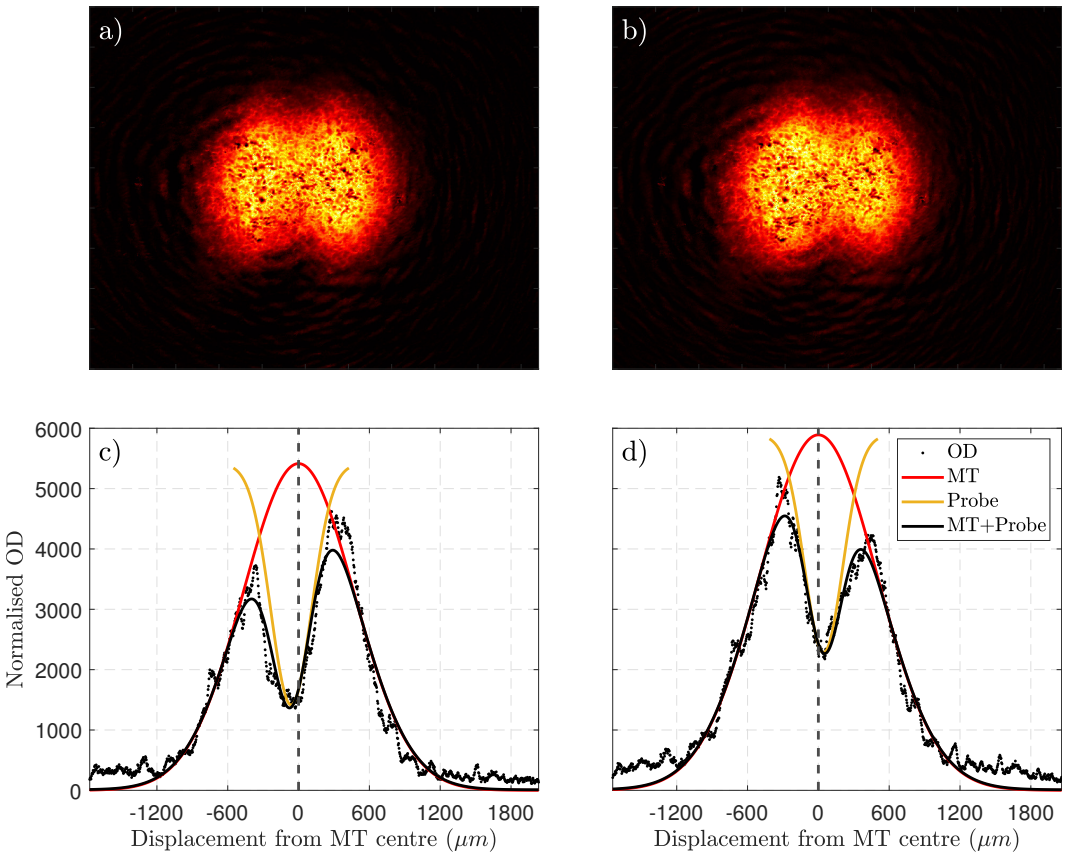

Figure 5.12: Absorption images (a+b) and corresponding horizontal interpolations (c+d) of the MT after a 1 ms pulse of probe light for two different angles of the probe mirror. The probe propagates vertically in the images and pushes atoms out of the trap. The horizontal interpolations of the OD and fitted with the sum of two gaussians, the large gaussian of the atoms in the MT and a smaller negative gaussian of the imprinted pattern of the probe beam profile on the atoms in the MT.

The probe beam was mode matched to the size of the atomic cloud in order to reduce photon shot noise at the polarimeter and also reach desired intensities. With the atomic cloud width being on the order of tens of microns, alignment was challenging and hence the piezo mirror was again implemented to steer a focussed probe beam down onto the atoms. Rastering the probe beam across the atoms allows both the alignment and the probe beam size to be determined. Initially the probe beam was detuned from $|F = 2\rangle \rightarrow |F' = 3\rangle$ by $\Delta_{Probe} = +330\,\text{MHz}$ to allow the probe beam to be destructive to the atomic sample. The probe was aligned to the magnetic trap as this is on the order of mm in width. The probe was strong enough to imprint

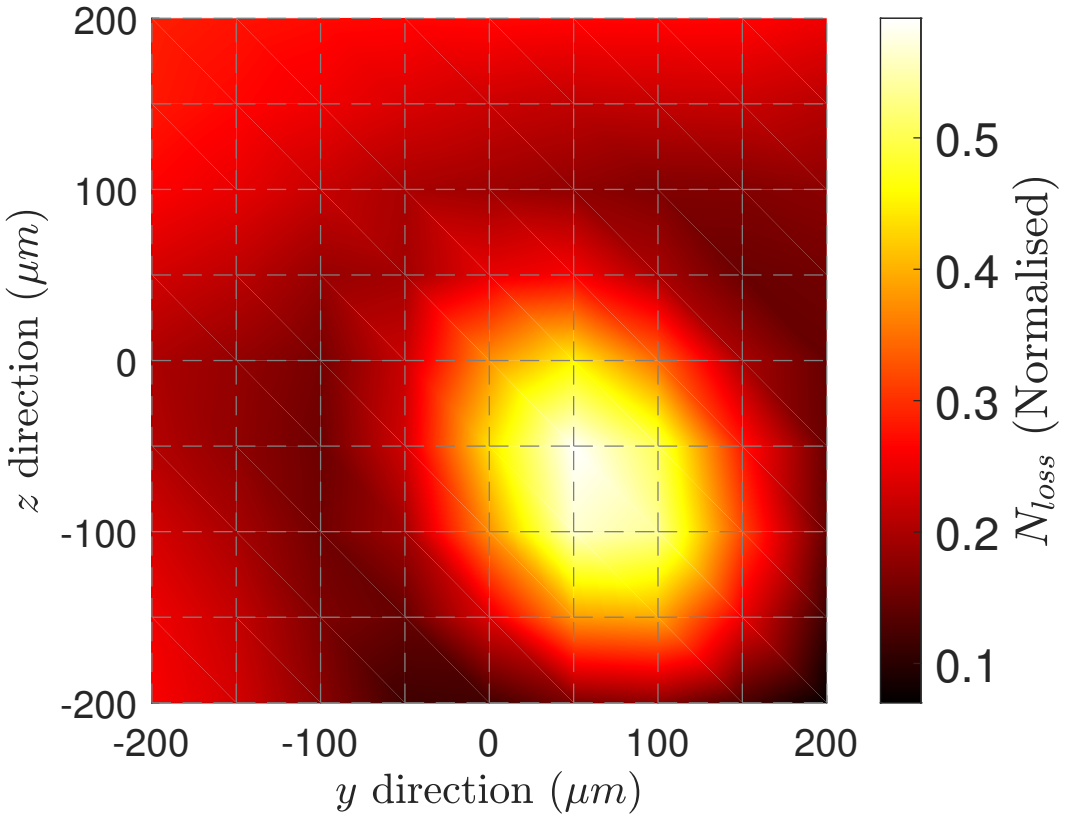

Figure 5.13: Normalised atomic loss from the dipole trap N_{loss} as the focussed 780 nm probe beam is rastered in the y-z plane. For each point a 2 ms probe pulse is applied to the atoms and the remaining atoms are measured with absorption imaging. The stepping of the piezomirror was calibrated from the results in figure 5.12. The surface is made from a 9-by-9 array which is smoothed by a Gaussian filter with standard deviation of 1.

a destructive gaussian shape on the OD image of the MT. Figure 5.12a shows the effect the probe had on the MT as it was aligned to the MT. The probe beam cuts a column out of the OD of the atomic cloud and this can be seen more clearly in the horizontal interpolation of the OD in figure 5.12c. The imprint of the probe beam can then be fitted to the OD interpolation and the centre of the beam can be determined. The probe beam was then rastered across the MT to calibrate the piezo scan. Figure 5.12b and 5.12d show the atoms after the piezo is jogged to the right of the MT centre. Fitting several of these shots allowed the calibration of the probe piezo mirror raster length scale. The process is then repeated in the dipole trap but now with the probe beam focussed into the chamber. The atomic loss from the dipole

trap N_{loss} is proportional the convolution of the probe beam profile and the atomic distribution in the DT

$$N_{loss} \propto I_{pr} \exp\left[-\frac{2r^2}{w_{pr}^2}\right] * n_0 \exp\left[-\frac{r^2}{2\sigma_{DT}^2}\right] \tag{5.4}$$

where I_{pr} and w_{pr} represent the probe intensity and waist respectively. Since equation 5.4 is the convolution of two gaussians, the solution is a gaussian with a width $\sigma_{N_{Loss}}$ defined as

$$\sigma_{N_{Loss}} = \sqrt{\sigma^2 + \frac{w_{pr}^2}{4}}. \tag{5.5}$$

Figure 5.13 shows N_{loss} as the 780 nm probe beam was rastered in the y-z plane. As expected this forms a 2D gaussian shape about the dipole trap which was fitted to find $\sigma_{N_{Loss}} = 40\,\mu\text{m}$ in the y axis. The DT absorption image in the absence of the probe was also fitted to find $\sigma_{DT} = 27\,\mu\text{m}$ also in the y axis. Using these values equation 5.5 gives the probe waist to be $w_{pr} = 59\,\mu\text{m}$.

5.2.3 Calibrating B_{RF}

Determining the AC sensitivity of the magnetometer relies on accurate knowledge of the magnitude of B_{RF}. While it is straightforward to measure the current of the coil and estimate the magnetic field induced by the coil, it requires a number of assumptions, namely that the coil geometry is that of an ideal solenoid and that the distance between the RF coil and the atoms is well known. These assumptions can be bypassed by instead calibrating B_{RF} with the linewidth of the magnetometer. Here I follow the method outlined in [85] where the the RF excitation can be modelled as a two-level Rabi oscillation from $|m_F = 1\rangle \leftrightarrow |m_F = 2\rangle$ where the Rabi coupling Ω_{RF} can be written as [127, 128]

$$\Omega_{RF} = \frac{1}{\hbar} \langle m_F = 1 | \, \mu \cdot \mathbf{B}_{RF} \, | m_F = 2 \rangle = \frac{g_F \mu_B}{\hbar} B_{RF} = \gamma_{Rb} B_{RF} \tag{5.6}$$

where $\boldsymbol{\mu}$ is the magnetic moment of the atom and γ_{Rb} is the gyromagnetic ratio of the electron in the ground state of ^{87}Rb. Figure 5.14 shows the results of the measured linewidth of the magnetometer as a function of the voltage supplied to the RF coil

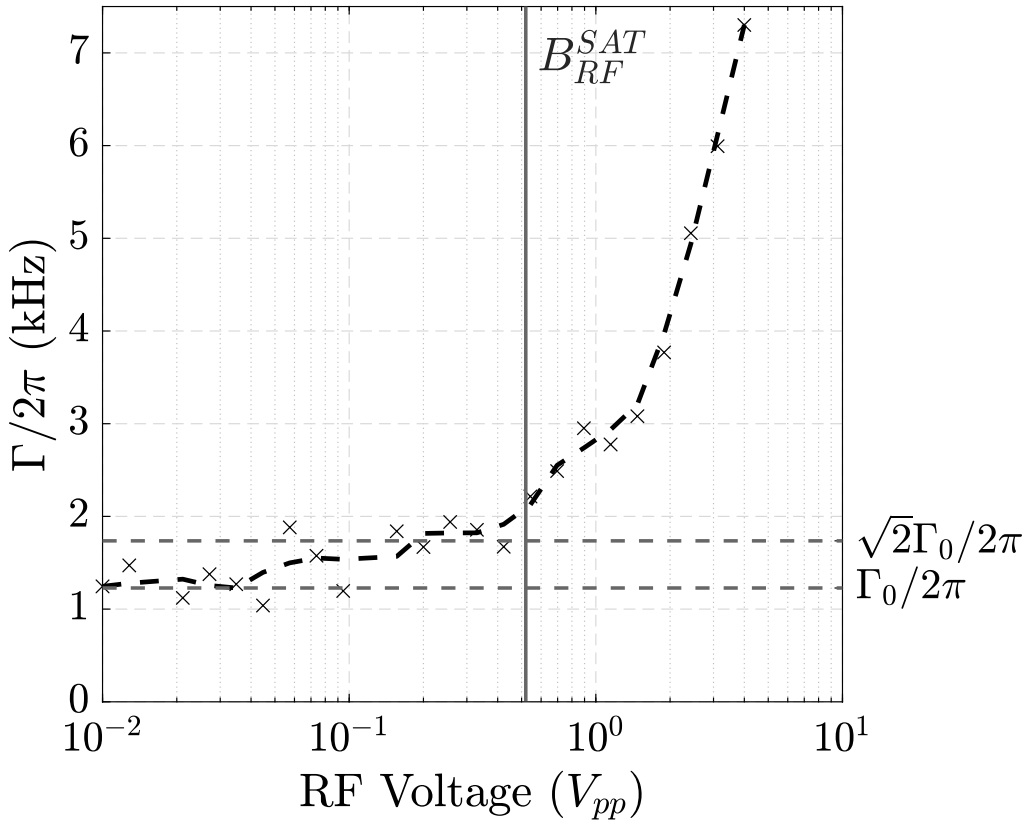

Figure 5.14: Linewidth of the magnetometer in the MT phase of the experiment as a function of the RF coil voltage. The black crosses represent the data points while the dashed black line represents a smoothed average. The vertical line shows the saturation point where the linewidth starts to become much broader than the saturation linewidth.

V_{RF}. For these measurements, the MT magnetometer was utilised to have the maximum atom number and therefore the strongest polarisation rotation signal possible. Ω_{RF} was swept incrementally over 40 shots to build up a spectrum at each increment of V_{RF}. The polarimeter signal was recorded on the oscilloscope for each shot and lock-in amplification was done in MATLAB to get the Lorentzian and dispersive lineshapes. The linewidth can be seen to clearly increase as a function of V_{RF}. At low values of B_{RF} where there is no RF broadening we define Γ_0 as the unbroadened linewidth of the magnetometer measured as $\Gamma_0/2\pi = 1.2\,\text{kHz}$ The saturation point $B_{RF}^{[SAT]}$ of the magnetometer is then defined as the point where the RF field broadens the linewidth to $\Gamma_{SAT} = \sqrt{2}\Gamma_0$. As in [85] it is then assumed that all the broadening that is added up to this point is the result of RF power broadening of the magnetic

transition and hence this difference in linewidth equates to the Rabi frequency of the RF such that $B_{RF}^{[SAT]} = \Omega_{RF}/\gamma_{Rb} = (\Gamma_{SAT} - \Gamma_0)/\gamma_{Rb} = 50.2\,\mathrm{nT_{rms}}$. In the figure, we see that the linewidth rises significantly above Γ_{SAT} after $V_{RF}^{[SAT]} = 0.52\,\mathrm{V}$ as indicated by the vertical line. Since the current I_{RF} in the RF coil of impedance Z will scale linearly with voltage $I_{RF} = V_{RF}/Z$ then B_{RF} is linearly proportional to V_{RF} and hence we arrive at the calibration $B_{RF}^{[SAT]}/V_{RF}^{[SAT]} = 96.5\,\mathrm{nT_{rms}/V}$.

5.2.4 Dipole Trap Magnetometry

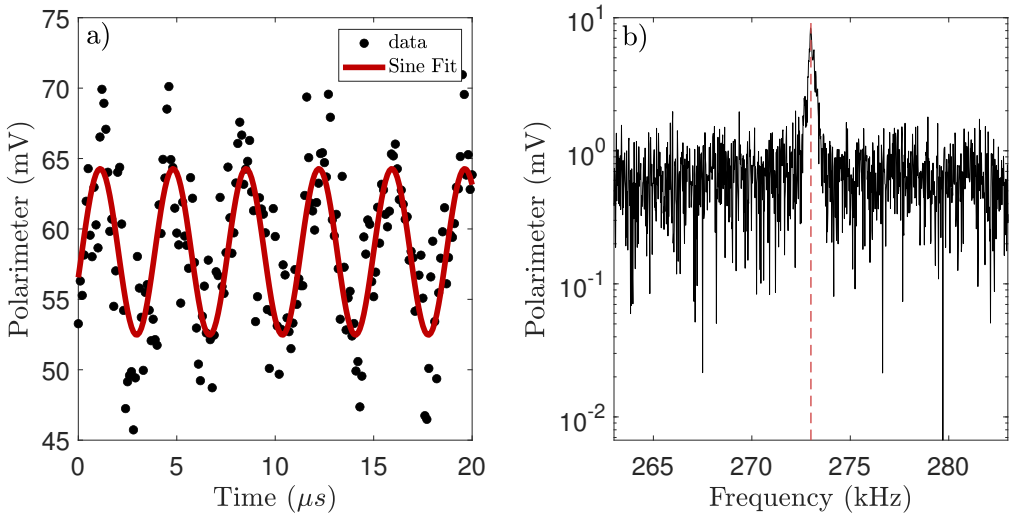

Figure 5.15: Polarimeter signal a) and FFT b) of the RF magnetometer in the dipole trap. The polarimeter signal is fitted with a sine function to show the polarisation oscillation. The fitted sine wave gives a frequency of 273 kHz which can be seen as the dashed vertical line in b which gives the peak in the FFT.

The DT magnetometer allows for long duration stationary measurements in a microscopic probe volume with only optical trapping. To prepare the DT magnetometer, the cooling sequence is interrupted during the DT evaporation stage and DT beams are held at constant power. The bias field B_{Bias} is then generated in the z axis and PID stabilised. B_{RF} is then generated in the y axis and the probe is pulsed. Figure 5.15 shows the raw output and the FFT of the polarimeter. The polarisation rotation signal is extremely small and dominated by photon shot noise but can be resolved in the FFT.

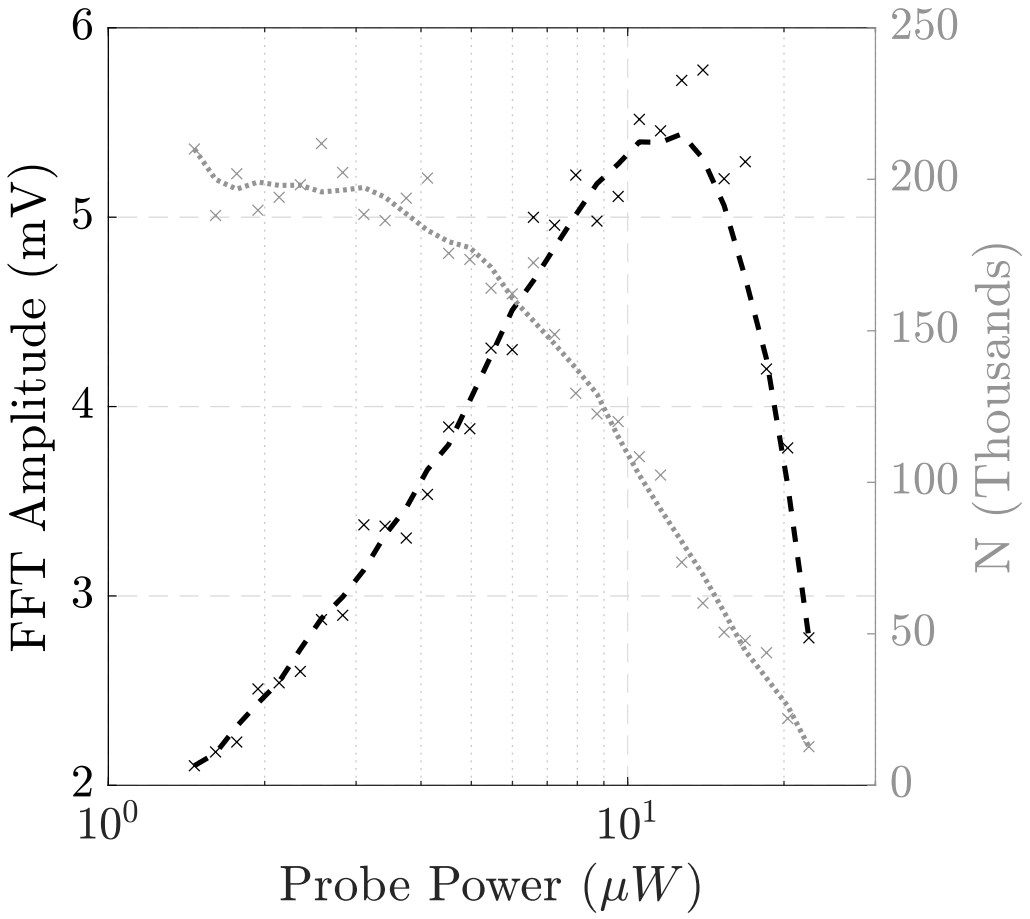

Figure 5.16: DT Magnetometer FFT amplitude (black) and surviving atom number (grey) after a 2 ms pulse of 780 nm probe light in the DT with varying probe power. The crosses show the raw data points and the lines shows a smoothed average of the data (8 point average). For each point, measurements were made at $\Omega_L/2\pi = 131$ kHz.

5.2.4.1 Probe Power

Figure 5.16 shows the effect of the 780 nm probe for pulses of 2 ms on the magnetometer FFT amplitude. The probe appears to hit an optimal power at ∼20 µW and then decays after this. The probe is inherently destructive to the DT and this can be shown by the decay in atom number that survive in the dipole trap with increasing probe power. The magnetometer amplitude becomes the combination of two competing effects: the intensity of probe light which linearly increases the amplitude, and the atom-loss with probe destruction which reduces the atom number that can be probed in the measurement.

5.2.4.2 AC Sensitivity

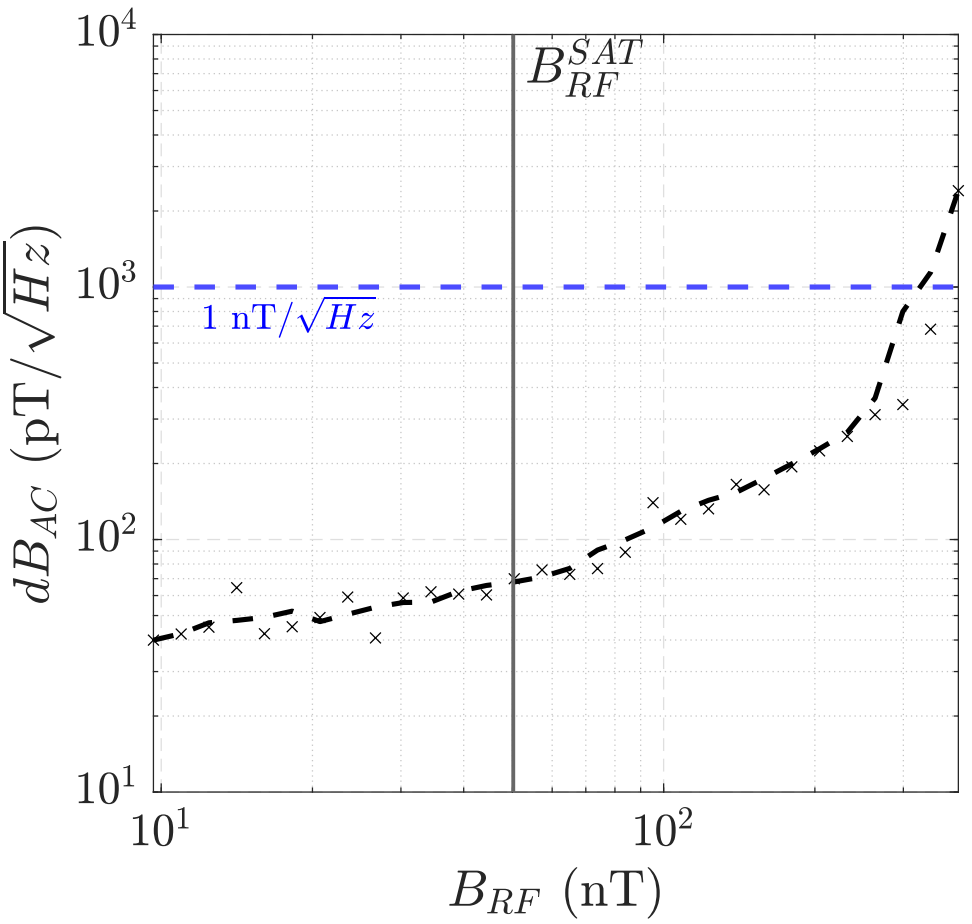

Figure 5.17: AC sensitivity of the DT magnetometer with varying magnitudes of B_{RF}. Measurements were made at $\Omega_L/2\pi = 131\,\text{kHz}$ with a duration of 4 ms. The black dashed line shows a smoothed average of the data points. B_{RF} was calibrated from the results in figure 5.14. The blue dashed line represents the level of $1\,\text{nT}/\sqrt{\text{Hz}}$. The green vertical line shows the $B_{RF}^{[SAT]}$ RF power.

Figure 5.17 shows the AC sensitivity dB_{AC} in the DT magnetometer calculated using equation 2.37 as a function of B_{RF}. For $B_{RF} > B_{RF}^{[SAT]}$, dB_{AC} degrades significantly, consistent with the RF broadening increasing the linewidth and therefore lowering the peak height and thus reducing the SNR. For $B_{RF}^{[SAT]} > B_{RF}$ we see dB_{AC} converge to $dB_{AC}^{[DT]} = 40\,\text{pT}/\sqrt{\text{Hz}}$.

5.2.5 BEC Magnetometry

In the BEC magnetometer, the atom number is significantly reduced to $N_a = 60k$ and as expected the signal height drops. Figure 5.18 shows the ASD of the mag-

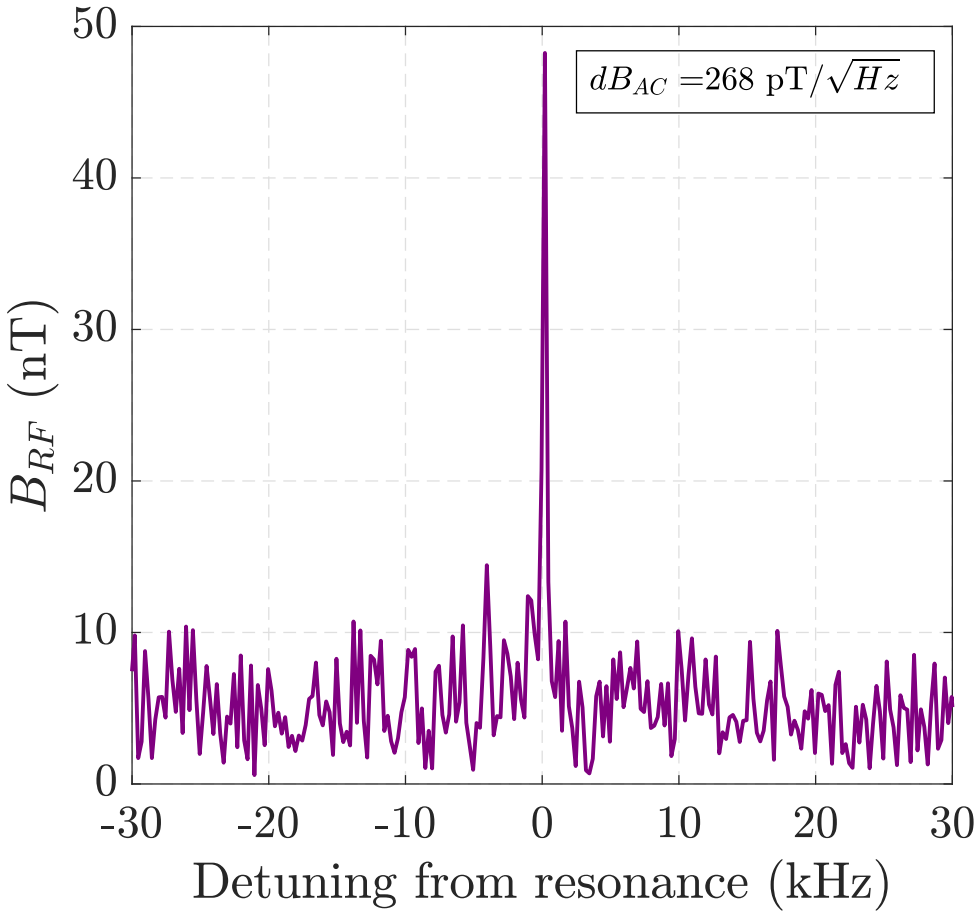

Figure 5.18: Amplitude spectrum of the BEC magnetometer after application of the reference field $B_{RF}^{[REF]} = 48.2\,\mathrm{nT_{rms}}$ as calibrated in section 5.2.3. The vertical scale is normalised by equating the peak height in the amplitude spectrum to $B_{RF}^{[REF]}$. The spectrum yields an SNR of 11.4 and was recorded with a 4 ms measurement duration which gives $dB_{AC} = 268\,\mathrm{pT}/\sqrt{\mathrm{Hz}}$.

netometer in the BEC phase. The amplitude of the polarimeter signal was scaled using the calibration in figure 5.14. This ultimately yielded the final sensitivity in the BEC to be $dB_{AC}^{[BEC]} = 268\,\mathrm{pT}/\sqrt{\mathrm{Hz}}$.

Considering equation 2.29 and the specific parameters of the BEC magnetometer, we find the atomic-projection-noise limit yields $dB_{SQL}^{[BEC]} = 8.1\,\mathrm{pT}/\sqrt{\mathrm{Hz}}$. Since the measured sensitivity is a factor of 33 higher, this suggests that the BEC magnetometer is either photon shot noise limited or technical-noise limited. Futher improvement in sensitivity could therefore be achieved by using a further detuned probe or by investigating electronic noise sources in the measurement technique. The

volumetric sensitivity yields the value $dB_{AC}^{[BEC]}\sqrt{V} = 50.2\,\mathrm{fT}\sqrt{\mathrm{cm}^3/\mathrm{Hz}}$. EMI was recently demonstrated at high spatial resolution by a NV magnetometer [65] which had a volumetric sensitivity of $112\,\mathrm{fT}\sqrt{\mathrm{cm}^3/\mathrm{Hz}}$. Since the result in the BEC magnetometer surpasses this value, it suggests that high-resolution EMI is achievable with this system.

5.3 Discussion

The implementation of the RF-AM in the ^{87}Rb BEC was ultimately successful, achieving a sensitivity of $dB_{AC}^{[BEC]} = 268\,\mathrm{pT}/\sqrt{\mathrm{Hz}}$. The volumetric sensitivity of $dB_{AC}^{[BEC]}\sqrt{V} = 50.2\,\mathrm{fT}\sqrt{\mathrm{cm}^3/\mathrm{Hz}}$ is comparable with recent high-spatial resolution EMI achieved in a diamond NV experiment, which suggests that high spatial resolution EMI imaging with the BEC is a realistic capability. This is also supported by a recent realisation of EMI of conductive targets in cold atoms using a MOT [129]. The reported sensitivity of $200\,\mathrm{pT}/\sqrt{\mathrm{Hz}}$ is comparable to the BEC RF-AM reported here but has a much larger probing volume (MOT diameter of 700 µm compared to BEC diameter of 27 µm) suggesting the BEC system could achieve a higher spatial resolution. The BEC RF-AM was found to not be currently atomic shot noise limited despite the low atomic number of $N_a = 65k$, suggesting that other factors like photon-shot-noise or technical noise can be combatted to achieve greater sensitivity in the future.

Chapter 6

Outlook

The main outcomes of this thesis were to look at two modalities of sensing RF magnetic fields with atomic magnetometers. One magnetometer based on the conventional thermal atomic vapour deployed as a moveable sensor head that could perform unshielded EMI imaging on stationary targets. The other, an RF-AM based on ultra-cold atoms with a view to using this sensor for high spatial-resolution EMI imaging.

The mechanically translatable RF-AM shows immediate promise in industrial applications by utilising EMI imaging with a compact unshielded sensor that can be moved about the target system. Two real-world problems from the aviation and oil&gas industry were investigated, with the mechanically translatable RF-AM able to provide a solution to these problems and show benefits over existing solutions. For pilot-hole detection, the system could image pilot-hole in an Al target concealed by a 0.41 mm Al skin, without the need for contact with the skin or for access to the pilot-hole. For corrosion detection, the system could detect thinning in an Al target with a linear response with recess depth. This could be achieved despite a layer of electrical and thermal insulation in the form of a 1.5 mm rubber sheet. The sensor was shown to work well and be very stable over days of measurement with minimal adjustment required. For this first proof-of-concept design, several opportunities to increase the performance were identified. The magnetic compensation system

worked well for accommodating the changes in background magnetic field with position, but magnetic gradients were found to change across the measurement area, which caused a discrepancy between the fluxgate reading and the field felt by the cell. A new compensation system based on multiple internal sensors could circumvent this issue and this concept was tested for the Cs experiment in section 4.1.9. Feedback loops to lock a magnetic gradient coil could also help to limit broadening due to field inhomogeneity and increase sensitivity. Using Cs could also provide more atoms at room temperature due to the higher vapour pressure which would improve sensitivity. Finally, adopting the pump-probe geometry put forward in [90] would make the pilot-hole defects radially symmetric, allowing the characteristic shape of the pilot holes to be identifiable in every direction, which could reduce the problem to scanning the sensor head in a line over the pilot-hole, instead of having to acquire a whole image.

The BEC RF-AM was able to sense RF magnetic fields at an extremely small probe volume of $3.2 \times 10^{-8}\,\mathrm{cm}^{-3}$ opening up the potential for high spatial-resolution EMI imaging by introducing an object close to the RF coil near the vacuum chamber. Results showed that again this sensor, operating in unshielded conditions, did not reach the atomic shot noise limt, suggesting further improvements can be made to the setup to enhance sensitivity. The use of a much further detuned probe for example, could reduce the atomic loss caused by the probe and allow for a higher number of photons to be used which could improve limitations with photon shot noise. Creating an array of BECs [76] could allow probing of many pixels simultaneously, allowing for very small scale gradiometry or one-shot high spatial-resolution EMI imaging. Finally, the use of a BEC can unlock the opportunity to exploit interatomic interactions and improve sensitivity with spin-squeezing effects [44].

Bibliography

[1] I. Savukov, S. Seltzer, and M. Romalis, "Detection of NMR signals with a radio-frequency atomic magnetometer," *Journal of Magnetic Resonance*, vol. 185, no. 2, pp. 214–220, 2007. (document), 1.2.1, 1.3

[2] C. Deans, *Electromagnetic Induction Imaging with Atomic Magnetometers*. PhD thesis, University College London, 2018. (document), 2.1, 2.1, 2.2.3, 3.1.6

[3] P. Bevington, R. Gartman, W. Chalupczak, C. Deans, L. Marmugi, and F. Renzoni, "Non-destructive structural imaging of steelwork with atomic magnetometers," *Applied Physics Letters*, vol. 113, no. 6, p. 063503, 2018. (document), 3.4

[4] A. Wickenbrock, N. Leefer, J. W. Blanchard, and D. Budker, "Eddy current imaging with an atomic radio-frequency magnetometer," *Applied Physics Letters*, vol. 108, no. 18, p. 183507, 2016. (document)

[5] C. Deans, Y. Cohen, H. Yao, B. Maddox, A. Vigilante, and F. Renzoni, "Electromagnetic induction imaging with a scanning radio frequency atomic magnetometer," *Applied Physics Letters*, vol. 119, no. 1, p. 014001, 2021. (document), 3.8

[6] B. Maddox, Y. Cohen, and F. Renzoni, "Through-skin pilot-hole detection and localization with a mechanically translatable atomic magnetometer," *Applied Physics Letters*, vol. 120, no. 1, p. 014002, 2022. (document), 1.1, 3.1, 3.11, 3.13

[7] Y. Cohen, B. Maddox, C. Deans, L. Marmugi, and F. Renzoni, "A radio-frequency Bose–Einstein condensate magnetometer," *Applied Physics Letters*, vol. 120, no. 16, p. 164002, 2022. (document), 5.11

[8] C. Deans, L. D. Griffin, L. Marmugi, and F. Renzoni, "Machine learning based localization and classification with atomic magnetometers," *Physical Review Letters*, vol. 120, no. 3, p. 033204, 2018. 1.1

[9] H.-Y. Wei, L. Ma, and M. Soleimani, "Volumetric magnetic induction tomography," *Measurement Science and Technology*, vol. 23, no. 5, p. 055401, 2012. 1.1

[10] W. Yin and A. Peyton, "A planar EMT system for the detection of faults on thin metallic plates," *Measurement Science and Technology*, vol. 17, no. 8, p. 2130, 2006. 1.1

[11] H. Griffiths, W. Stewart, and W. Gough, "Magnetic induction tomography: a measuring system for biological tissues," *Annals of the New York Academy of Sciences*, vol. 873, no. 1, pp. 335–345, 1999. 1.1

[12] L. Marmugi, C. Deans, and F. Renzoni, "Electromagnetic induction imaging with atomic magnetometers: Unlocking the low-conductivity regime," *Applied Physics Letters*, vol. 115, no. 8, p. 083503, 2019. 1.1, 2.1

[13] B. J. Darrer, J. C. Watson, P. A. Bartlett, and F. Renzoni, "Electromagnetic imaging through thick metallic enclosures," *AIP Advances*, vol. 5, no. 8, p. 087143, 2015. 1.1

[14] J. S. Bennett, B. E. Vyhnalek, H. Greenall, E. M. Bridge, F. Gotardo, S. Forstner, G. I. Harris, F. A. Miranda, and W. P. Bowen, "Precision magnetometers for aerospace applications: A review," *Sensors*, vol. 21, no. 16, p. 5568, 2021. 1.1

[15] H. Griffiths, "Magnetic induction tomography," *Measurement science and technology*, vol. 12, no. 8, p. 1126, 2001. 1.2.1

[16] A. Korjenevsky, V. Cherepenin, and S. Sapetsky, "Magnetic induction tomography: experimental realization," *Physiological measurement*, vol. 21, no. 1, p. 89, 2000. 1.2.1

[17] C. Reig, M.-D. Cubells-Beltrán, and D. R. Muñoz, "Magnetic field sensors based on giant magnetoresistance (GMR) technology: Applications in electrical current sensing," *Sensors*, vol. 9, no. 10, pp. 7919–7942, 2009. 1.2.2

[18] F. Hankard, J. Gattacceca, C. Fermon, M. Pannetier-Lecoeur, B. Langlais, Y. Quesnel, P. Rochette, and S. A. McEnroe, "Magnetic field microscopy of rock samples using a giant magnetoresistance–based scanning magnetometer," *Geochemistry, Geophysics, Geosystems*, vol. 10, no. 10, 2009. 1.2.2

[19] F. Hankard, J. Gattacceca, C. Fermon, M. Pannetier-Lecoeur, B. Langlais, Y. Quesnel, P. Rochette, and S. A. McEnroe, "Magnetic field microscopy of rock samples using a giant magnetoresistance–based scanning magnetometer," *Geochemistry, Geophysics, Geosystems*, vol. 10, no. 10, 2009. 1.2.2

[20] B. D. Josephson, "Possible new effects in superconductive tunnelling," *Physics letters*, vol. 1, no. 7, pp. 251–253, 1962. 1.2.3

[21] J. Clarke and A. I. Braginski, *The SQUID handbook*, vol. 1. Wiley Online Library, 2004. 1.2.3

[22] J. Zhang, L. Xu, G. Bian, P. Fan, M. Li, W. Liu, and H. Yuan, "Diamond nitrogen-vacancy center magnetometry: Advances and challenges," *arXiv preprint arXiv:2010.10231*, 2020. 1.2.4

[23] G. Balasubramanian, I. Chan, R. Kolesov, M. Al-Hmoud, J. Tisler, C. Shin, C. Kim, A. Wojcik, P. R. Hemmer, A. Krueger, *et al.*, "Nanoscale imaging magnetometry with diamond spins under ambient conditions," *Nature*, vol. 455, no. 7213, pp. 648–651, 2008. 1.2.4

[24] J. M. Taylor, P. Cappellaro, L. Childress, L. Jiang, D. Budker, P. Hemmer, A. Yacoby, R. Walsworth, and M. Lukin, "High-sensitivity diamond magne-

tometer with nanoscale resolution," *Nature Physics*, vol. 4, no. 10, pp. 810–816, 2008. 1.2.4

[25] M. W. Mitchell and S. P. Alvarez, "Colloquium: Quantum limits to the energy resolution of magnetic field sensors," *Reviews of Modern Physics*, vol. 92, no. 2, p. 021001, 2020. 1.2.4

[26] K.-M. C. Fu, G. Z. Iwata, A. Wickenbrock, and D. Budker, "Sensitive magnetometry in challenging environments," *AVS Quantum Science*, vol. 2, no. 4, p. 044702, 2020. 1.2.4

[27] H. Dang, A. C. Maloof, and M. V. Romalis, "Ultrahigh sensitivity magnetic field and magnetization measurements with an atomic magnetometer," *Applied Physics Letters*, vol. 97, no. 15, p. 151110, 2010. 1.2.5

[28] I. M. Savukov, S. Seltzer, M. Romalis, and K. Sauer, "Tunable atomic magnetometer for detection of radio-frequency magnetic fields," *Physical review letters*, vol. 95, no. 6, p. 063004, 2005. 1.2.5, 2.2.2

[29] S.-K. Lee, K. Sauer, S. Seltzer, O. Alem, and M. Romalis, "Subfemtotesla radio-frequency atomic magnetometer for detection of nuclear quadrupole resonance," *Applied Physics Letters*, vol. 89, no. 21, p. 214106, 2006. 1.2.5

[30] P. Bevington, R. Gartman, D. Botelho, R. Crawford, M. Packer, T. Fromhold, and W. Chalupczak, "Object surveillance with radio-frequency atomic magnetometers," *Review of Scientific Instruments*, vol. 91, no. 5, p. 055002, 2020. 1.2.5

[31] L. Marmugi, C. Deans, and F. Renzoni, "Electromagnetic induction imaging with atomic magnetometers: Unlocking the low-conductivity regime," *Applied Physics Letters*, vol. 115, no. 8, p. 083503, 2019. 1.2.5

[32] C. Deans, L. Marmugi, and F. Renzoni, "Sub-picotesla widely tunable atomic magnetometer operating at room-temperature in unshielded environments," *Review of Scientific Instruments*, vol. 89, no. 8, p. 083111, 2018. 1.2.5, 4.1.9

[33] D. A. Keder, D. W. Prescott, A. W. Conovaloff, and K. L. Sauer, "An unshielded radio-frequency atomic magnetometer with sub-femtotesla sensitivity," *Aip Advances*, vol. 4, no. 12, p. 127159, 2014. 1.2.5

[34] R. Zhang, T. Dyer, N. Brockie, R. Parsa, and R. Mhaskar, "Subpicotesla scalar atomic magnetometer with a microfabricated cell," *Journal of Applied Physics*, vol. 126, no. 12, p. 124503, 2019. 1.2.5

[35] D. Hunter, S. Piccolomo, J. Pritchard, N. Brockie, T. Dyer, and E. Riis, "Free-induction-decay magnetometer based on a microfabricated cs vapor cell," *Physical Review Applied*, vol. 10, no. 1, p. 014002, 2018. 1.2.5

[36] J. Kitching, S. Knappe, V. Shah, P. Schwindt, C. Griffith, R. Jimenez, J. Preusser, L.-A. Liew, and J. Moreland, "Microfabricated atomic magnetometers and applications," in *2008 IEEE International Frequency Control Symposium*, pp. 789–794, IEEE, 2008. 1.2.5

[37] I. Savukov, "Gradient-echo 3d imaging of rb polarization in fiber-coupled atomic magnetometer," *Journal of Magnetic Resonance*, vol. 256, pp. 9–13, 2015. 1.2.5

[38] M. Vengalattore, J. Higbie, S. Leslie, J. Guzman, L. Sadler, and D. Stamper-Kurn, "High-resolution magnetometry with a spinor Bose-Einstein condensate," *Physical review letters*, vol. 98, no. 20, p. 200801, 2007. 1.2.5, 1.2.6

[39] N. Schlosser, G. Reymond, and P. Grangier, "Collisional blockade in microscopic optical dipole traps," *Physical review letters*, vol. 89, no. 2, p. 023005, 2002. 1.2.6

[40] F. M. Ciurana, G. Colangelo, L. Slodička, R. Sewell, and M. Mitchell, "Entanglement-enhanced radio-frequency field detection and waveform sensing," *Physical review letters*, vol. 119, no. 4, p. 043603, 2017. 1.2.6, 2.2.6.3

[41] D. Gallego, S. Hofferberth, T. Schumm, P. Krüger, and J. Schmiedmayer, "Optical lattice on an atom chip," *Optics letters*, vol. 34, no. 22, pp. 3463–3465, 2009. 1.2.6

[42] O. S. Burrow, P. F. Osborn, E. Boughton, F. Mirando, D. P. Burt, P. F. Griffin, A. S. Arnold, and E. Riis, "Stand-alone vacuum cell for compact ultracold quantum technologies," *Applied Physics Letters*, vol. 119, no. 12, p. 124002, 2021. 1.2.6

[43] R. H. Koch, J. Clarke, W. Goubau, J. M. Martinis, C. Pegrum, and D. J. Van Harlingen, "Flicker (1/f) noise in tunnel junction dc SQUIDs," *Journal of low temperature physics*, vol. 51, no. 1, pp. 207–224, 1983.

[44] W. Muessel, H. Strobel, D. Linnemann, D. Hume, and M. Oberthaler, "Scalable spin squeezing for quantum-enhanced magnetometry with Bose-Einstein condensates," *Physical review letters*, vol. 113, no. 10, p. 103004, 2014. 1.3, 6

[45] P. A. Bottomley and E. R. Andrew, "RF magnetic field penetration, phase shift and power dissipation in biological tissue: implications for NMR imaging," *Physics in Medicine & Biology*, vol. 23, no. 4, p. 630, 1978. 2.1

[46] A. V. Vorst, A. Rosen, and Y. Kotsuka, *Fundamentals of Electromagnetics*, pp. 7–62. 2006. 2.1

[47] S. Watson, R. Williams, W. Gough, and H. Griffiths, "A magnetic induction tomography system for samples with conductivities below 10 s m- 1," *Measurement Science and Technology*, vol. 19, no. 4, p. 045501, 2008. 2.1

[48] C. J. Foot, *Atomic physics*, vol. 7. OUP Oxford, 2004. 2.2.1, 2.4.2.2

[49] *Optical Magnetometry*. Cambridge University Press, 2013. 2.2.2, 2.2.5.1

[50] C. Cohen-Tannoudji, "Linear superpositions of states in radiative processes," *Physica Scripta*, vol. 1997, no. T70, p. 79, 1997. 2.2.2

[51] S. J. Seltzer, *Developments in alkali-metal atomic magnetometry*. Princeton University, 2008. 2.2.2, 2.2.3, 2.2.5.1, 2.2.6.1

[52] G. A. Smith, S. Chaudhury, and P. S. Jessen, "Faraday spectroscopy in an optical lattice: a continuous probe of atom dynamics," *Journal of Optics B: Quantum and Semiclassical Optics*, vol. 5, no. 4, p. 323, 2003. 2.2.2

[53] V. Acosta, M. Ledbetter, S. Rochester, D. Budker, D. J. Kimball, D. Hovde, W. Gawlik, S. Pustelny, J. Zachorowski, and V. Yashchuk, "Nonlinear magneto-optical rotation with frequency-modulated light in the geophysical field range," *Physical Review A*, vol. 73, no. 5, p. 053404, 2006. 2.2.2

[54] G. Vasilakis, *Precision measurements of spin interactions with high density atomic vapors*. Princeton university, 2011. 2.2.3

[55] A. Serafin, Y. Castin, M. Fadel, P. Treutlein, and A. Sinatra, "Nuclear spin squeezing by continuous quantum non-demolition measurement: a theoretical study," *arXiv preprint arXiv:2012.14686*, 2020. 2.2.5.1

[56] G. Vitagliano, *Spin squeezing, macrorealism and the heisenberg uncertainty principle*. PhD thesis, Universidad del País Vasco-Euskal Herriko Unibertsitatea, 2015. 2.2.5.1

[57] D. Budker and M. Romalis, "Optical magnetometry," *Nature physics*, vol. 3, no. 4, pp. 227–234, 2007. 2.2.5.1

[58] W. Happer and A. Tam, "Effect of rapid spin exchange on the magnetic-resonance spectrum of alkali vapors," *Physical Review A*, vol. 16, no. 5, p. 1877, 1977. 2.2.5.1

[59] W. HAPPER, "Optical pumping," *Rev. Mod. Phys.*, vol. 44, pp. 169–249, Apr 1972. 2.2.5.1

[60] B. Julsgaard, J. Sherson, J. Sørensen, and E. S. Polzik, "Characterizing the spin state of an atomic ensemble using the magneto-optical resonance

method," *Journal of Optics B: Quantum and Semiclassical Optics*, vol. 6, no. 1, p. 5, 2003. 2.2.5.1

[61] P. Glasenapp, A. Greilich, I. Ryzhov, V. Zapasskii, D. Yakovlev, G. Kozlov, and M. Bayer, "Resources of polarimetric sensitivity in spin noise spectroscopy," *Physical Review B*, vol. 88, no. 16, p. 165314, 2013. 2.2.5.2

[62] B.-B. Li, J. Bilek, U. B. Hoff, L. S. Madsen, S. Forstner, V. Prakash, C. Schäfermeier, T. Gehring, W. P. Bowen, and U. L. Andersen, "Quantum enhanced optomechanical magnetometry," *Optica*, vol. 5, no. 7, pp. 850–856, 2018. 2.2.6

[63] S. Forstner, S. Prams, J. Knittel, E. Van Ooijen, J. Swaim, G. Harris, A. Szorkovszky, W. Bowen, and H. Rubinsztein-Dunlop, "Cavity optomechanical magnetometer," *Physical review letters*, vol. 108, no. 12, p. 120801, 2012. 2.2.6

[64] S. Pustelny, A. Wojciechowski, M. Gring, M. Kotyrba, J. Zachorowski, and W. Gawlik, "Magnetometry based on nonlinear magneto-optical rotation with amplitude-modulated light," *Journal of Applied Physics*, vol. 103, no. 6, p. 063108, 2008. 2.2.6.2

[65] C. Xu, J. Zhang, H. Yuan, G. Bian, P. Fan, M. Li, and T. Liu, "Burst eddy current testing with diamond magnetometry," *Applied Physics Letters*, vol. 120, no. 8, p. 084104, 2022. 2.2.6.3, 5.2.5

[66] M. W. Mitchell and S. P. Alvarez, "Colloquium: Quantum limits to the energy resolution of magnetic field sensors," *Reviews of Modern Physics*, vol. 92, no. 2, p. 021001, 2020. 2.2.6.3

[67] J. Allred, R. Lyman, T. Kornack, and M. V. Romalis, "High-sensitivity atomic magnetometer unaffected by spin-exchange relaxation," *Physical review letters*, vol. 89, no. 13, p. 130801, 2002. 2.2.6.3

[68] Y. Li, J. Wu, G. Feng, J. Nute, S. Piano, L. Hackermüller, J. Ma, L. Xiao, and S. Jia, "Enhanced Raman sideband cooling of caesium atoms in a vapour-loaded magneto-optical trap," *Laser Physics Letters*, vol. 12, no. 5, p. 055501, 2015. 2.3.4, 2.3.4, 4.1.6, 4.2.5.1

[69] V. Vuletić, C. Chin, A. J. Kerman, and S. Chu, "Degenerate Raman sideband cooling of trapped cesium atoms at very high atomic densities," *Physical Review Letters*, vol. 81, no. 26, p. 5768, 1998. 2.3.4, 4.1.7, 4.2.5.1

[70] G. Di Domenico, N. Castagna, G. Mileti, P. Thomann, A. Taichenachev, and V. Yudin, "Laser collimation of a continuous beam of cold atoms using zeeman-shift degenerate-Raman-sideband cooling," *Physical Review A*, vol. 69, no. 6, p. 063403, 2004. 2.3.4, 4.2.5.1, 4.2.5.5

[71] H. Metcalf and P. van der Straten, "Cooling and trapping of neutral atoms," *Physics Reports*, vol. 244, no. 4-5, pp. 203–286, 1994. 2.4, 4.2.2.2

[72] W. Ketterle and N. Van Druten, "Evaporative cooling of trapped atoms," in *Advances in atomic, molecular, and optical physics*, vol. 37, pp. 181–236, Elsevier, 1996. 2.4

[73] J. Söding, D. Guéry-Odelin, P. Desbiolles, G. Ferrari, and J. Dalibard, "Giant spin relaxation of an ultracold cesium gas," *Physical review letters*, vol. 80, no. 9, p. 1869, 1998. 2.4.1

[74] K. B. Davis, M.-O. Mewes, M. R. Andrews, N. J. van Druten, D. S. Durfee, D. Kurn, and W. Ketterle, "Bose-Einstein condensation in a gas of sodium atoms," *Physical review letters*, vol. 75, no. 22, p. 3969, 1995. 2.4.1

[75] C.-L. Hung, X. Zhang, N. Gemelke, and C. Chin, "Accelerating evaporative cooling of atoms into Bose-Einstein condensation in optical traps," *Physical Review A*, vol. 78, no. 1, p. 011604, 2008. 2.4.2.2

[76] A. B. Deb, T. McKellar, and N. Kjærgaard, "Optical runaway evaporation

for the parallel production of multiple Bose-Einstein condensates," *Physical Review A*, vol. 90, no. 5, p. 051401, 2014. 2.4.2.2, 6

[77] M. Theis, *Optical Feshbach resonances in a Bose-Einstein condensate*. na, 2005. 2.5

[78] F. Dalfovo, S. Giorgini, L. P. Pitaevskii, and S. Stringari, "Theory of Bose-Einstein condensation in trapped gases," *Reviews of modern physics*, vol. 71, no. 3, p. 463, 1999. 2.5, 2.5.1

[79] W. Ketterle, D. S. Durfee, and D. M. Stamper-kurn, "Making, probing and understanding Bose-Einstein condensates," in *proceedings of the international school of physics "Enrico Fermi", course cxl, edited by m. inguscio, s. stringari and c.e. wieman (ios)*, p. 67, Press, 1999. 2.5, 2.5.2

[80] V. Bagnato, D. E. Pritchard, and D. Kleppner, "Bose-Einstein condensation in an external potential," *Physical Review A*, vol. 35, no. 10, p. 4354, 1987. 2.5.1

[81] H. Otoishi, S. Nagata, T. Yukawa, K. Yamashita, and T. Kinoshita, "Rapid production of a Rb85 Bose-Einstein condensate in a double compressible optical dipole trap," *Physical Review A*, vol. 102, no. 2, p. 023316, 2020. 2.5.2

[82] Z. Ma, C. Han, X. Jiang, R. Fang, Y. Qiu, M. Zhao, J. Huang, B. Lu, and C. Lee, "Production of 87Rb Bose-Einstein condensate in an asymmetric crossed optical dipole trap," *Chinese Physics Letters*, vol. 38, no. 10, p. 103701, 2021. 2.5.2

[83] M. D. Rotondaro and G. P. Perram, "Collisional broadening and shift of the rubidium D1 and D2 lines (52s12 52p12, 52p32) by rare gases, H2, D2, N2, CH4 and CF4," *Journal of Quantitative Spectroscopy and Radiative Transfer*, vol. 57, no. 4, pp. 497–507, 1997. 3.1.2

[84] D. A. Steck, "Rubidium 87 D line data," 2001. 3.3, 3.1.4, 6, 5.2

[85] P. Bevington, *Radio frequency atomic magnetometer for applications in magnetic induction tomography*. PhD thesis, University of Strathclyde, 2021. 3.2, 5.2.3, 5.2.3

[86] J. D. Zipfel, S. Santosh, P. Bevington, and W. Chalupczak, "Object composition identification by measurement of local radio frequency magnetic fields with an atomic magnetometer," *Applied Sciences*, vol. 12, no. 16, 2022. 10

[87] S. F. Pedigo, G. E. Georgeson, R. D. Rempt, G. L. Clark, and J. L. Hafenrichter, "Control system and method for a magnetic indexer for high accuracy hole drilling," *US Patent 6,927,560*, vol. 45, no. 2, pp. 103–114, 2005. 11, 3.3

[88] N. Avdelidis and D. P. Almond, "Transient thermography as a through skin imaging technique for aircraft assembly: modelling and experimental results," *Infrared physics & technology*, vol. 45, no. 2, pp. 103–114, 2004. 3.3

[89] T. Dursun and C. Soutis, "Recent developments in advanced aircraft aluminium alloys," *Materials & Design (1980-2015)*, vol. 56, pp. 862–871, 2014. 13

[90] P. Bevington, R. Gartman, and W. Chalupczak, "Enhanced material defect imaging with a radio-frequency atomic magnetometer," *Journal of Applied Physics*, vol. 125, no. 9, p. 094503, 2019. 3.3, 6

[91] B. J. Darrer, J. C. Watson, P. Bartlett, and F. Renzoni, "Magnetic imaging: a new tool for UK national nuclear security," *Scientific reports*, vol. 5, no. 1, pp. 1–6, 2015. 3.3

[92] F. De Vogelaere, "Corrosion under insulation," *Process Safety Progress*, vol. 28, no. 1, pp. 30–35, 2009. 3.4

[93] C. Deans, L. Marmugi, and F. Renzoni, "Active underwater detection with an

array of atomic magnetometers," *Applied Optics*, vol. 57, no. 10, pp. 2346–2351, 2018. 3.5

[94] Y. B. Ovchinnikov, "Compact magneto-optical sources of slow atoms," *Optics communications*, vol. 249, no. 4-6, pp. 473–481, 2005. 4.1.3

[95] Z. Lu, K. Corwin, M. Renn, M. Anderson, E. A. Cornell, and C. Wieman, "Low-velocity intense source of atoms from a magneto-optical trap," *Physical review letters*, vol. 77, no. 16, p. 3331, 1996. 4.1.3

[96] D. A. Steck, "Cesium D line data," 2003. 4.3, 4.2.2.2, 4.21, 4.2.5.2

[97] T. Weber, *Bose-Einstein condensation of optically trapped cesium*. na, 2003. 4.1.5, 4.3

[98] N. Castagna, G. Domenico, G. Dudle, G. Mileti, M. Plimmer, A. Taichenachev, P. Thomann, and V. Yudin, "Collimation of a continuous cold atomic beam using Raman sideband laser cooling," pp. 431 – 435, 05 2004. 4.1.6

[99] S. Wolf, S. J. Oliver, and D. S. Weiss, "Suppression of recoil heating by an optical lattice," *Physical review letters*, vol. 85, no. 20, p. 4249, 2000. 4.1.7

[100] B. Fröhlich, T. Lahaye, B. Kaltenhäuser, H. Kübler, S. Müller, T. Koch, M. Fattori, and T. Pfau, "Two-frequency acousto-optic modulator driver to improve the beam pointing stability during intensity ramps," *Review of scientific instruments*, vol. 78, no. 4, p. 043101, 2007. 4.1.7

[101] X.-T. Xu, Z.-Y. Wang, R.-H. Jiao, C.-R. Yi, W. Sun, and S. Chen, "Ultra-low noise magnetic field for quantum gases," *Review of Scientific Instruments*, vol. 90, no. 5, p. 054708, 2019. 4.1.9

[102] J. Ringot, P. Szriftgiser, and J. C. Garreau, "Subrecoil Raman spectroscopy of cold cesium atoms," *Physical Review A*, vol. 65, no. 1, p. 013403, 2001. 4.1.9

[103] C. J. Dedman, R. Dall, L. Byron, and A. Truscott, "Active cancellation of stray magnetic fields in a Bose-Einstein condensation experiment," *Review of scientific instruments*, vol. 78, no. 2, p. 024703, 2007. 4.1.9

[104] Z. Ji, J. Yuan, Y. Zhao, X. Chang, Y. Yang, L. Xiao, and S. Jia, "Optimization and analysis of experimental parameters for polarization gradient cooling in optical molasses," *arXiv preprint arXiv:1304.7066*, 2013. 4.2.2.2

[105] Y. S. Domnin, G. Elkin, A. Novoselov, L. Kopylov, V. Baryshev, and V. Pal'Chikov, "VNIIFTRI cesium fountain," *Canadian journal of physics*, vol. 80, no. 11, pp. 1321–1327, 2002. 4.2.2.2

[106] C. Townsend, N. Edwards, K. Zetie, C. Cooper, J. Rink, and C. Foot, "High-density trapping of cesium atoms in a dark magneto-optical trap," *Physical Review A*, vol. 53, no. 3, p. 1702, 1996. 4.2.2.2

[107] W. Petrich, M. H. Anderson, J. R. Ensher, and E. A. Cornell, "Behavior of atoms in a compressed magneto-optical trap," *JOSA B*, vol. 11, no. 8, pp. 1332–1335, 1994. 4.2.3.1

[108] C. Salomon, J. Dalibard, W. Phillips, A. Clairon, and S. Guellati, "Laser cooling of cesium atoms below 3 μk," *EPL (Europhysics Letters)*, vol. 12, no. 8, p. 683, 1990. 4.2.4.1

[109] D. Guéry-Odelin, J. Söding, P. Desbiolles, and J. Dalibard, "Strong evaporative cooling of a trapped cesium gas," *Optics Express*, vol. 2, no. 8, pp. 323–329, 1998. 4.2.4.1

[110] Y. Li, J. Wu, G. Feng, J. Nute, S. Piano, L. Hackermüller, J. Ma, L. Xiao, and S. Jia, "Enhanced Raman sideband cooling of caesium atoms in a vapour-loaded magneto-optical trap," *Laser Physics Letters*, vol. 12, no. 5, p. 055501, 2015. 4.2.4.1, 4.3

[111] C.-Y. Huang, C.-C. Chen, L.-A. Sun, G.-B. Liao, K.-S. Wu, Y.-J. Lin, and M.-S. Chang, "A simple recipe for rapid all-optical formation of spinor Bose-

Einstein condensates," *Journal of Physics B: Atomic, Molecular and Optical Physics*, vol. 50, no. 15, p. 155302, 2017. 4.2.4.3

[112] P. Treutlein, K. Y. Chung, and S. Chu, "High-brightness atom source for atomic fountains," *Physical Review A*, vol. 63, no. 5, p. 051401, 2001. 4.2.5.1

[113] M. Repp, R. Pires, J. Ulmanis, R. Heck, E. Kuhnle, M. Weidemüller, and E. Tiemann, "Observation of interspecies 6 Li-133 Cs feshbach resonances," *Physical Review a*, vol. 87, no. 1, p. 010701, 2013. 4.2.5.1

[114] Y. Li, J. Wu, G. Feng, J. Nute, S. Piano, L. Hackermüller, J. Ma, L. Xiao, and S. Jia, "Enhanced Raman sideband cooling of caesium atoms in a vapour-loaded magneto-optical trap," *Laser Physics Letters*, vol. 12, no. 5, p. 055501, 2015. 4.2.5.1

[115] R. Grimm, M. Weidemüller, and Y. B. Ovchinnikov, "Optical dipole traps for neutral atoms," in *Advances in atomic, molecular, and optical physics*, vol. 42, pp. 95–170, Elsevier, 2000. 4.2.5.2

[116] A. J. Kerman, "Raman sideband cooling and cold atomic collisions in optical lattices," *Ph. D. Thesis*, 2002. 4.2.5.3, 4.2.5.5

[117] T. Savard, K. O'hara, and J. Thomas, "Laser-noise-induced heating in far-off resonance optical traps," *Physical Review A*, vol. 56, no. 2, p. R1095, 1997. 4.2.5.4

[118] V. Vuletić, C. Chin, A. J. Kerman, and S. Chu, "Degenerate Raman sideband cooling of trapped cesium atoms at very high atomic densities," *Physical Review Letters*, vol. 81, no. 26, p. 5768, 1998. 4.2.5.4

[119] M. Gröbner, P. Weinmann, E. Kirilov, and H.-C. Nägerl, "Degenerate Raman sideband cooling of K39," *Physical Review A*, vol. 95, no. 3, p. 033412, 2017. 4.2.5.5

[120] T. Akatsuka, M. Takamoto, and H. Katori, "Three-dimensional optical lattice clock with bosonic Sr88 atoms," *Physical Review A*, vol. 81, no. 2, p. 023402, 2010. 4.2.6.2

[121] A. Wood, L. Turner, and R. Anderson, "Measurement and extinction of vector light shifts using interferometry of spinor condensates," *Physical Review A*, vol. 94, no. 5, p. 052503, 2016. 4.2.6.2

[122] A. Guttridge, S. Hopkins, S. Kemp, M. D. Frye, J. M. Hutson, and S. L. Cornish, "Interspecies thermalization in an ultracold mixture of Cs and Yb in an optical trap," *Physical Review A*, vol. 96, no. 1, p. 012704, 2017. 4.3

[123] M. Repp, *Interspecies Feshbach resonances in an ultracold, optically trapped Bose-Fermi mixture of cesium and lithium*. PhD thesis, 2013. 4.3

[124] A. S. Flores, H. P. Mishra, W. Vassen, and S. Knoop, "Simple method for producing Bose-Einstein condensates of metastable helium using a single-beam optical dipole trap," *Applied Physics B*, vol. 121, no. 3, pp. 391–399, 2015. 5.1.3

[125] I. Savukov, T. Karaulanov, and M. Boshier, "Ultra-sensitive high-density rb-87 radio-frequency magnetometer," *Applied Physics Letters*, vol. 104, no. 2, p. 023504, 2014. 5.2.1

[126] C. Deans, L. Marmugi, S. Hussain, and F. Renzoni, "Electromagnetic induction imaging with a radio-frequency atomic magnetometer," *Applied Physics Letters*, vol. 108, no. 10, p. 103503, 2016. 5.2.1

[127] G. Liu, O. Be'Er, Y. Margalit, M. Givon, D. Groswasser, Y. Japha, and R. Folman, "Survival of the fittest in the coherent evolution of quantum ensembles," *Physical Review A*, vol. 98, no. 1, p. 013856, 2018. 5.2.3

[128] A. V. Taichenachev, V. Yudin, C. Oates, C. Hoyt, Z. Barber, and L. Hollberg, "Magnetic field-induced spectroscopy of forbidden optical transitions with

application to lattice-based optical atomic clocks," *Physical review letters*, vol. 96, no. 8, p. 083001, 2006. 5.2.3

[129] A. Fregosi, C. Gabbanini, S. Gozzini, L. Lenci, C. Marinelli, and A. Fioretti, "Magnetic induction imaging with a cold-atom radio frequency magnetometer," *Applied Physics Letters*, vol. 117, no. 14, p. 144102, 2020. 5.3